UPC **CTTC**

Numerical simulation of bubbles and drops in complex geometries by using dynamic meshes

Centre Tecnològic de Transferència de Calor
Departament de Màquines i Motors Tèrmics
Universitat Politècnica de Catalunya

Enrique Gutiérrez Álvarez
Doctoral Thesis

Numerical simulation of bubbles and drops in complex geometries by using dynamic meshes

Enrique Gutiérrez Álvarez

TESI DOCTORAL

presentada al

Departament de Màquines i Motors Tèrmics
E.S.E.I.A.A.T.,
Universitat Politècnica de Catalunya

per a l'obtenció del grau de

Doctor per la Universitat Politècnica de Catalunya

Terrassa, July 2018

Numerical simulation of bubbles and drops in complex geometries by using dynamic meshes

Enrique Gutiérrez Álvarez

Director de la tesi

Dr. Assensi Oliva Llena

Co-director de la tesi

Dr. Néstor Vinicio Balcázar Arciniega

Tribunal Qualificador

Dr. Iztok Tiselj
University of Ljubljana

Dr. Antonio M. Pascau Benito
University of Zaragoza

Dr. Carlos D. Pérez-Segarra
Polytechnic University of Catalonia

A mis padres, Encarni y Manolo

```
X:1
T:Glutius
M:4/4
L:1/8
Q: 1/4=140
V:P1 clef=treble
V:P2 clef=bass t=2 octave=-2
%%score {P1 | P2}
K:Bm
V:P1
|:{f}g4 d4 | B3^c da3|1 f8- | f8 :|2 f8- | f6 _e=f||
|:{f}g4 d4 | B3^c da3|1 eA f6- | f4 zd_e=f :|2 f8- | f6 ag ||
|:{^d}[e3 G3] B ^c g3-|g4 [=f4 a4] |{a}[_b3 g3] g d' a3-|a4 [e ^c][f d][a A][g =B] |
{^d}[e3 G3] B ^c g3-|g4 [=f4 a4] |1 {a}[_b3 g3] g d' a3-|a4 d2- (3dag :|2 [d' g] [^c'3 f3]-[^c'4 f4]-| [^c'8 f8]]
V:P2
|:_Bg_ed' _Bg_ed' &_e4 _B4| =eged' =cged' & =c4 G4 |1 dfdd' Bfdd' &B4 f4| Bfdd' Bfdd' & d4 F4 :|2 Bfdd' Bfdd' &d2 a2 b2 a2| Bf (3gag dfga & d2 x6||
|:_Bg_ed' _Bg_ed' &_e4 _B4| =eged' =cged' & =c4 G4 |1 dfdd' Bfdd' &B4 f4| Bfdd' Bfdd' & d4 F4 :|2 Bf [D6 a6 d6 d'6]-&d2 x6|[D8 a8 d8 d'8] ||
|: eged' eged'& =c4 G4| eged' eg=fd'& =C4 G4| _eged' =cged' &=c4 _B4 | _eged' ^ca=ed' &=c4 A4 |
eged' eged'& =c4 G4| eged' eg=fd'& =C4 G4|1 _eged' =cged' &=c4 _B4 | _eged' ^ca=ed' &=c4 A4 :|2 [b8 d8 G8] | z8 ||
```

Acknowledgements

Me gustaría empezar mis agradecimientos por Assensi Oliva, director de mi tesis y del Centro Tecnológico de transferencia de Calor (CTTC). Él me ha transmitido su pasión por la mecánica de fluidos computacional; y no solo eso, ha confiado en mi, y me ha apoyado en los momentos difíciles durante estos años. Así mismo, es el principal responsable de haber creado este espacio de trabajo constructivo y dinámico que es el CTTC.

También me gustaría agradecer la labor de mi co-director de tesis Néstor Balcázar, y de mi tutor Joaquim Rigola. Juntos nos hemos enfrentado a multitud de retos científicos. Ellos siempre me han tendido la mano cuando la he necesitado. Os agradezco de corazón vuestra contribución a esta tesis.

Quedo también profundamente agradecido a mis compañeros del CTTC que me han acompañado durante esta aventura. A Octavi por todo el tiempo que ha dedicado a solucionar mis problemas informáticos. A Eduard, con quien he ido de la mano en el doctorado, apoyándonos cuando lo hemos necesitado. A Ali, por querer ser mi amigo, tal y como le pedí amablemente el primer día que le conocí. A Jesús por recogerme cada día a las 13:30 y llevarme a comer. A Héctor, por todas esas conversaciones interesantes en nuestro despacho. A Fede, por su paciencia y dedicación a nuestro trabajo. A Carles, que ha sido tanto padre como amigo dentro del laboratorio. A Jordi Chiva, por su ayuda en programación. A Lluis Jofre, por su amabilidad y atención en mi primera etapa en el CTTC, guiándome en el aprendizaje del código. A todos ellos, y a los que no incluyo por razones de espacio, muchas gracias.

Así mismo, me gustaría agradecerle a la profesora Darina Murray del Trinity College de Dublin mi acogida por tres meses, así como su amabilidad conmigo, enseñándome el funcionamiento del grupo que lidera y poniéndome en contacto con los investigadores que trabajan allí. Igualmente, quiero agradecerle a Pedro Curto su recibimiento en el Instituto de Ingeniería Mecánica y Producción industrial (IIMPI), de la Universidad de la República (Uruguay). Pedro me aceptó amablemente en la institución que dirige, donde tuve la ocasión de realizar una estancia de investigación de un mes y medio.

Agradezco muy especialmente el apoyo de mis familiares Encarni, Manolo, Helena, Chris e Inés, y del resto de mi familia que no puedo mentar por falta de espacio.

Finalmente, como autor de esta tesis me gustaría agradecer a la Generalitat de

Catalunya por el apoyo financiero recibido durante la tesis doctoral. De igual forma, a la UPC, el programa *Erasmus+* de la Unión Europea, y a *La Caixa*, por haber contribuido económicamente a que puediese realizar las estancias de investigación en el extranjero. Por último, quiero agradecer también a la Red Española de Supercomputación y al *Irish Centre for High-End Computing* por los recursos computacionales provistos durante mi doctorado.

Abstract

The present thesis aims at improving the versatility of the DNS simulations of multiphase flows. CFD techniques are important tools for the study of multiphase flows, because most of the physical phenomena of these flows often happen on space and time scales where experimental methodologies are impossible in practice. Notwithstanding, numerical approaches are limited by the computational power of the present computers. In this sense, small improvements in the efficiency of the simulations can make the difference between an approachable problem and an unapproachable one. The proposal of this doctoral thesis is focused on developing numerical algorithms to optimize the simulations of multiphase solvers based on single-fluid formulations, applied on three-dimensional unstructured meshes, in the context of a finite-volume discretization. In particular, in the light of previous background of the *Heat and Mass Transfer Technological Center* (CTTC) research group, the methods developed in the context of this PhD thesis use a conservative level set technique to deal with the multiphase domain. The previous work on multiphase flows developed at CTTC is mainly focused in build robust DNS solvers that can be used to address fundamental problems of bubbles, drops and jets. Thus, it is worth noting that the work presented in the present PhD thesis is the first attempt within CTTC research group to bring those methods to real scenarios, with complex geometries and long physical domains.

The work has been organized in five chapters and four appendices. The first chapter constitutes an introduction to the multiphase flows and the different approaches used to study them. It also includes a description of the background of the present thesis, and a brief mathematical description of the chosen interface tracking technique (i.e. the conservative level set method). The core work of the of this PhD thesis is explained throughout chapters two, three, and four. In those chapters, the improvements performed on the multiphase DNS techniques are addressed in detail, providing results comparisons and discussions on the obtained outcomes. Most of the content of these chapters has been already submitted or published in international journals and conferences. The wording of those papers have been slightly adapted, aiming at unifying their format and at structuring them within the complete document. Consequently, each chapter is not self-contained, although some key concepts are often recalled. After developing the main ideas of the thesis a final concluding chapter is presented, summarizing the main findings of this research, and pointing out some future work. Finally, the appendices includes some material that can be useful to understand in depth some specific parts of the thesis but, conversely, they are not essential to follow the main thread.

As said before, the core work of this thesis is presented throughout chapters two, three and four. In chapter two, four domain optimization methods are formulated and tested. By using these techniques, small domains can be used in rising bubble simu-

lations, thus saving computational resources. These methods have been implemented in a conservative level set framework. Some of these methods require the use of open boundaries. Therefore, a careful treatment of both inflow and outflow boundaries has been carried out. This includes the development of a new outflow boundary condition as a variation of the classical convective outflow. At this point, a study about the sizing of the computational domain has been conducted, paying special attention to the placement of the inflow and outflow boundaries. Additionally, once the methods are formulated, several validation cases are run to discuss the applicability and robustness of each method.

The third chapter presents a physical study of a challenging problem: the Taylor bubble. By using the most promising technique from those presented in the previous chapter (i.e. the moving mesh method), the problem of an elongated bubble rising in stagnant liquid is addressed here. A transient study on the velocity field of the problem is provided. Moreover, the study also includes sensitivity analyses with respect to the initial shape of the bubble, the initial volume of the bubble, the flow regime and the inclination of the channel.

Chapter number four presents an extension of the developed method to simulate bubbles and drops evolving in complex geometries. The use of an immersed boundary method allows to deal with intricate geometries and to reproduce internal boundaries within an ALE framework. The resulting method is capable of dealing with full unstructured meshes. Different problems are studied here to assert the proposed formulation, both involving constricting and non-constricting geometries. In particular, the following problems are addressed: a 2D gravity-driven bubble interacting with a highly-inclined plane, a 2D gravity-driven Taylor bubble turning into a curved channel, the 3D passage of a drop through a periodically constricted channel, and the impingement of a 3D drop on a flat plate.

Contents

Abstract **v**

1 Introduction **1**
1.1 Motivation . . . 1
1.2 Background . . . 2
1.2.1 Multiphase flows in CFD . . . 2
1.2.2 High Performance Computing . . . 4
1.2.3 CTTC research group . . . 4
1.3 Objectives of the thesis . . . 6
1.4 Outline of the thesis . . . 7
1.5 Preliminary concepts on multiphase DNS . . . 8
1.5.1 Conservative level set governing equations . . . 8
1.5.2 Interface capturing . . . 9
1.5.3 Surface tension treatment . . . 10
References . . . 10

2 An assessment of domain optimization methods to simulate bubbles dynamics **17**
2.1 Introduction . . . 17
2.2 Domain optimization methods . . . 19
2.2.1 Fringe zone method . . . 20
2.2.2 Buffer zone method . . . 23
2.2.3 Moving mesh method . . . 24
2.2.4 Space conservation Law . . . 24
2.2.5 Non-inertial reference frame method . . . 25
2.3 Numerical methods . . . 26
2.3.1 Time step . . . 28
2.3.2 Calculation algorithms . . . 29
2.4 Boundary conditions treatment . . . 31
2.4.1 Periodic boundary condition . . . 31
2.4.2 Inflow boundary condition . . . 32
2.4.3 Outflow boundary condition . . . 32
2.5 Domain sizing . . . 36
2.5.1 Lateral boundaries placement . . . 36
2.5.2 Inlet placement . . . 37
2.5.3 Outlet placement . . . 42
2.6 Numerical experiments . . . 42

2.6.1 Two dimensional rising bubble 42
2.6.2 Three dimensional rising bubble 44
2.7 Conclusions 47
References 51

3 The Taylor Bubble problem 55
3.1 Introduction 56
3.2 Mathematical formulation 57
3.2.1 Interface capturing 58
3.2.2 Surface tension treatment 59
3.2.3 Moving mesh 59
3.2.4 Numerical schemes 60
3.3 Taylor bubble study 61
3.3.1 General considerations about the problem 61
3.3.2 Taylor bubble rising in viscous liquid - validation case 63
3.3.3 Effect of the initial shape of the Taylor bubble 66
3.3.4 Effect of the volume of the Taylor bubble 69
3.3.5 Effect of the Eötvös number 72
3.3.6 Effect of the Morton number 74
3.3.7 Effect of channel inclination 77
3.4 Conclusions 85
References 86

4 Bubbles and drops evolving through complex geometries 89
4.1 Introduction 90
4.2 Mathematical formulation 94
4.2.1 Interface capturing 95
4.2.2 Surface tension treatment 96
4.3 Numerical solution 96
4.3.1 Mesh movement and boundary conditions 97
4.3.2 Immersed boundary treatment 99
4.3.3 Time step 103
4.3.4 Calculation algorithm 104
4.4 Discussion on the method 104
4.5 Results and validation 106
4.5.1 Two-dimensional gravity-driven bubble approaching an inclined plane 107
4.5.2 Two-dimensional gravity-driven Taylor bubble through a curved channel 110
4.5.3 Three-dimensional gravity-driven falling drop against a plane surface 115

4.5.4 Three-dimensional gravity-driven buoyant drop in a constricted circular channel . . . 120
4.5.5 Three-dimensional gravity-driven unconstrained drop impinging on a horizontal plane . . . 127
4.6 Conclusions . . . 132
References . . . 135

5 Conclusions and future research **141**
5.1 Concluding remarks . . . 141
5.2 Future research . . . 142
5.2.1 Dynamic readjustment of the distances from the bubble/drop to the boundaries . . . 144
5.2.2 Domain sizing . . . 144
5.2.3 Deformability of the solids . . . 146
5.2.4 Contact angle model . . . 147
5.2.5 Coalescence and break-up . . . 147
References . . . 149

A Calculations of bubble/drop properties **151**

B Exact calculation of the swept volume for moving mesh methods **153**
B.1 Moving the mesh through a curve . . . 154
B.1.1 Two dimensional case . . . 155
B.1.2 Numerical considerations for particular cases . . . 156
B.2 Mass update process . . . 156
B.3 Extruded cylindrical mesh . . . 161
B.3.1 Swept Volume . . . 162
References . . . 163

C List of publications and presentations at congresses **165**

D Computational resources **167**

1

Introduction

The current section aims to present a first look at the work accomplished throughout this thesis. Multiphase flows and their interaction with solids are present in a broad range of industrial an natural phenomena. These problems have been studied by the scientific community over the last centuries, casting valuable light upon their complex physic. Therefore, some emphasis is placed on those methodology analysis. Additionally, some important applications will be highlighted in subsequents sections. Finally, the background of the present work is synthesized at the end of the chapter, as well as some useful preliminary concepts.

1.1 Motivation

As said before, the proper solution of multiphase flows is of paramount importance to laid a solid foundation on the understanding of many processes present in engineering and natural science. For example, the successful optimization of an oil extraction plant is conditioned to a complete comprehension of the slug flow pattern (elongated bubbles moving inside a pipe) [1]. The chemical engineering is another field fed by the multiphase knowhow. Micro-reactors and the lab-on-a-chip concept are good examples of bubbly flow applications within chemical science [2]. In addition, due to the fact that biomedical studies are becoming increasingly important for the scientific community, multiphase flows seems to be a significant issue to understand complex blood flow cases, i.e. embolisms. Other relevant engineering fields are also directly related to this discipline: microfluidics, volcanology, geothermal power plants, cryogenic fluids, sprays and injection processes. Additionally, many natural phenomena are conditioned to the behaviour of multiphase flows. For instance, cloud formation, rainfall, cosmic motions, and others. See [1] for a detailed explanation on the applications of this type of flow.

The simulation of multiphase flows falls within the broader field of the computational fluid dynamics (CFD). In particular, the methodology followed in the present thesis lies within the so-called Direct Numerical Simulation (DNS) field, which involves

a complete resolution of all turbulence scales. The present work aims to shed some light on the resources optimization and flexibility of those multiphase DNS methods. By progressively introducing numerical improvements, the proposed DNS approach will be optimized, seeking to achieve a more versatile method as explained in Sec. 1.3.

1.2 Background

The present PhD thesis is developed on the context of the computational fluid dynamics (CFD). This discipline is strongly linked with the high performance computing (HPC), used to maximize its applicability. The current section introduces both CFD and HPC fields, as well as it describes the scientific group within the present work has been developed.

1.2.1 Multiphase flows in CFD

The intrinsic complexity of multiphase flows limits the approachability of the scientific community to their related phenomena. On the one hand, theoretical and analytical methods usually involve major assumptions, which compromises the applicability of the obtained results. On the other hand, experimental approaches are not always reliable, due to the difficulties related with the process of setting the initial conditions, as well as visualization problems. As an alternative to those methods, numerical approaches can be adopted. Those methodologies are becoming increasingly important due to the growth of the computational power available for the scientific community.

The CFD science consists on the analysis of problems involving fluid flows, heat transfer and associated phenomena, by means of computer-based simulation [3]. The development of the CFD started at 1960s linked to the aerospace engineering. This analysis technique is founded upon two mathematical disciplines: modeling and numerical methods. An important branch of CFD is the direct numerical simulation (DNS) of multiphase flows, which studies the evolution of physical domains in where several fluids coexist.

During the last two decades, great advances have been made in direct numerical simulations of multiphase flow. Unverdi and Tryggvason [4, 5] computed the interactions of two-dimensional and three-dimensional bubbles and Jan [3] examined the motion of two axisymmetric and two-dimensional bubbles in more detail. Ervin and Tryggvason [6, 7] computed the rise of a bubble in a vertical shear flow and showed that the lift force changes sign when the bubble deforms. The results of Jan and Ervin [6,8], which cover a Reynolds number range of about $1-100$ have yielded insight into the dependency of attractive and repulsive forces between two bubbles, depending on the Reynolds number and bubble deformability. Tryggvason and collaborators [4–8] have examined the motion of nearly spherical bubbles in periodic domains for low den-

sity ratio and Reynolds number between 20 and 30, using the front-tracking method. Bunner and Tryggvason [9, 10] simulated a much larger number of three-dimensional bubbles following the motion of 216 three-dimensional bubbles in a periodic domain for a relatively long time.

In general, DNS multiphase methods can be classified in two main groups: those using an Eulerian framework and those using a Lagrangian one. The latter is composed of front-tracking methods [11], which precisely describe the multiphase flow, but they are complex to implement due to the need for re-meshing at each iteration. Inside the group of methods that use an Eulerian approach, there are three main types: the volume-of-fluid (VoF) methods [12], the level set (LS) methods [13] and hybrid methods, for example, the CLSVoF method [14]. The VoF methods have the advantage of inherently conserving the mass, but the calculus of the geometrical properties at the interface is troublesome. On the contrary, level set approaches precisely calculate these geometrical properties of the interface (normal and curvature), but they have drawbacks in mass conservation. The hybrid methods usually solve both problems at the expense of increasing the computational cost.

In the present PhD thesis a LS approach is used to simulate problems of bubbles and drops. Those methods are founded upon the tracking of a sharp interface which separates the two different fluids. When dealing with bubbly flows, these two fluids can be unambiguously named as the "suspending fluid" and the "secondary phase". This is the selected criterion in the present document. Level set methods work by advecting a marker function (namely, the level set function) which takes an specific value at the secondary phase and another one at the suspending fluid (see Fig. 1.1). The process of advecting this function while keeping the interface sharp is a challenging issue in level set methods. According to Tryggvason et al. [11], the other troublesome facts for getting reliable simulations are (i) the tracking of the interface separating the fluids and (ii) the implementation of a model which takes into account the surface tension force. Although level set techniques had been broadly used in mathematics, the work of Sussman et al. [15] is considered the first successful application of a level set method to multiphase DNS. Sussman proposed a standard level set (SLS) approach, in which the level set function is a simple distance function. Successful implementations of this technique were demonstrated through the subsequent years (see for instance, [13, 15–23]). In 2005, Olsson et al. [18] carried out a significant improvement on the development of the method. Olsson settled down the so-called conservative level set (CLS) method by introducing a reinitialization step in the calculation algorithm of the level set method. This improved method greatly reduces the mass conservation problems present in the SLS. The development of the CLS was culminated in 2014 by Balcázar et al. [24], who generalized the method for unstructured meshes. Since then, the method has been widely used [14, 25–29].

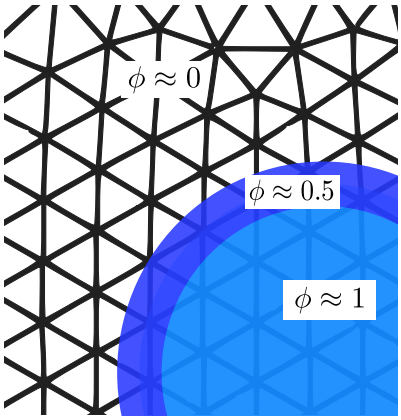

Figure 1.1: Example of a marker function in a level set method.

1.2.2 High Performance Computing

The development of CFD (and in particular multiphase DNS) is strongly linked with the high performance computing (HPC) science. It is well-known that CFD software is highly demanding in terms of computational power. Some specific simulations could last years if they are run sequentially (i.e. using one CPU). HPC makes possible the division of the computational domain in different regions, thus each of them is assigned to a different CPU (*parallelization*). Nowadays, this feature is essential in any reliable DNS software. Moreover, the computational power grows exponentially over time, as well as other computing tools, like the GPUs capabilities. All of this makes possible to face DNS problems in a reasonable time.

The HPC also facilitates the exploration of a level of detail that could not be accessible by using any other scientific approach (i.e. theoretical or experimental). This is due to the fact that the coupling of CFD and HPC makes possible the solution of very small turbulence scales, thus allowing a practically unlimited level of detail of results, as well as providing the ability to study systems under hazardous conditions at and beyond their normal performance limit (e.g accident scenarios and safety studies) [3].

1.2.3 CTTC research group

The CTTC and its environment develop their own CFD code called *TermoFluids* [30]. The code is a 3D unstructured parallel code that uses state-of-the-art numerical and physical models to perform accurate scientific analysis of engineering problems. Special care has been taken in its parallel performance, having a high efficiency in supercom-

puters. The development of the code has been a source of scientific publications in the most prominent scientific journals, which supports its reliability.

TermoFluids code employs collocated unstructured meshes, in where a finite volume discretization of the Navier-Stokes equations is performed. This discretization is conservative, due to the fact that the employed numerical schemes preserve the properties of the differential operators in which they are based. That is, some properties of the discretization ensure the kinetic-energy conservation and the stability of the code. Those properties are: the negative conjugate transpose of the gradient operator is approximately equal to the divergence operator, the convective operator is skew-symmetric, and the diffusive operator is symmetric positive-definite.

In order to run the *TermoFluids* software, the CTTC has a Beowulf HPC cluster (see Fig. 1.2) with a total of 2304 cores (1024 processing cores 128 nodes of two Quad-core CPUs each and 1280 processing cores distributed in 40 nodes of 32 Cores each). It has an infiniband DDR 4X network interconnection between nodes with latencies of 2.25 microseconds with a 20Gbits/s bandwidth and a system of files that allow unified capacities of several Petabytes, highly scalable.

Figure 1.2: JFF cluster at CTTC.

In addition, the scalability of the code in solving the Navier-Stokes equations has been recently tested up to 131072 CPU at the ALCF [31]. The scalability of the CLS multiphase solver has been demonstrated to reach 3072CPUs (PRACE project 2014112666 and 2016153612) [27, 32–34].

The group attained several milestones within CFD research. Some of the important topics addressed at CTTC are: natural and forced convection [35], turbulence modeling [36], combustion [37], radiation [42], refrigeration [43], HVAC [44], absorption [45],

fluid-solid interaction [46], numerical algorithms and solvers [48], moving and non-structured grids [47], adaptive mesh refinement [49], tribology [50], etc. Additionally, the multiphase flow branch has been broadly developed [14, 24–29, 32–34, 38–41], and some of this previous advances done at CTTC are essential to understand the course of the present thesis. Therefore, these founding ideas are summarized below, in Sec. 1.5.

1.3 Objectives of the thesis

Multiphase DNS has attracted a great deal of interest from the scientific community during the last decades. This is reflected in the the large amount of relevant improvements into the field (see Sec. 1.2.1). However, multiphase DNS is still far from facing many of the problems present in the industry. This arises from two main reasons. First, it is not easy to assure a proper coupling among the physics under consideration. And second, the computational power is still insufficient to tackle some challenging real cases, which involve big domains, long time-evolution and/or many different turbulent scales.

In order to address this last issue, there are some recurring approaches in the literature. One of this ideas consists in assuming axisymmetry, two-dimensionality or some kind of periodicity in the fluid domain. Although these approaches are useful to shed some light in some specific configurations, they should not be considered if a generic method to face industrial problems is sought. This is because they might omit some of the three-dimensional effects, inherently present in the real problems.

The founding idea of the present work is to consider three-dimensional and unstructured computational domains, which is aligned with the general philosophy of *Termofluids* code. From this point, we will consider the adaptation of the current DNS approaches to face real problems. In particular, we will be focus on the conservative level set (CLS) method, which is the most promising technique to simulate multiphase flows among those tested at CTTC. Therefore, a solid CLS method has been taken as starting point of the work developed in this thesis. See [24, 26] for details on the applicability of this CLS method.

In order to maintain a three-dimensional computational domain in bubbles and drops problems, some measures should be taken to make the problem approachable. In this sense, we observed the following issue: in rising bubble problems, there is a intrinsic need of leaving enough vertical space, so that the bubble evolves. This introduce a major problem: the expense of computational resources by the fact that regions far from the bubble are being solved. It is easy to see that those regions are not actually important to calculate the dynamics of the bubble. Therefore, some specific flow regimes would be impossible to dealt with, due to the size of the resulting meshes. Few previous approaches to this problem (although relevant [51–56]) are available in the scientific literature.

Based on this preliminary problem, we settled the following objectives for the present thesis:

- Investigate the different methods present in in the literature to reduce the computational domain in rising bubbles problems. Implement the feasible ones in the context of the CLS, and discuss their applicability.
- Select the most promising method and use it to study a challenging problem: the motion of a Taylor bubble. Detailed findings on the flow regime and rise conditions should be provided, in order to prove the validity of the coupling between the selected domain optimization method with the CLS method.
- Adapt the aforementioned method to simulate real intricate geometries, while keeping the computational expenditure under control.

These improvements should be implemented in the context of *Termofluids* code. For this purpose, the founding concepts of this software should be born in mind. In particular, those concerning mass conservation. This is essential to be coherent with the used CLS method. Other properties should also be a source of concern (i.e. scalability, interaction with other physics, etc.).

Finally, it is worth noting that, although the aforementioned improvements will be specifically designed for working with a CLS method, they could be easily transposed to other single fluid formulations (e.g. VoF, CLSVoF, Ghost fluid), by carrying out minor adjustments. Analogously, the developed methods should also work in staggered grid arrangements, by carrying out minor modifications.

1.4 Outline of the thesis

As mentioned before, the present thesis aims at improving the versatility of CLS method when dealing with bubbles/drops evolving in complex geometries. To accomplish this goal, a preliminary overview of the basic concepts of the conservative level set method is described over the present introductory chapter, in order to make the rest of the document more comprehensible.

The first of the posed objectives of this thesis (see Sec. 1.3) will be addressed thorough Ch. 2. Therefore, we will perform a numerical investigation on the methods allowing a reduction of the computational size in bubbles and drops problems. Several methods will be implemented in the context of *Termofluids*. Once formulated, they will be validated against experiments, and compared among then.

At this point, we intend to choose the domain optimization method presenting a better performance. Therefore, a discussion on the tested methods becomes important to clarify the advantages and drawbacks of each approach. The most promising technique will be applied to seed some light on an industrial problem: the slug flow.

Many numerical experiments will be performed throughout Ch. 3 on the Taylor bubble problem. This study includes sensitivity analyses with respect to the initial shape of the bubble, the initial volume of the bubble, the flow regime and the inclination of the channel, among others.

After that, an adaptation of the used method to simulate complex geometries will be sought. In Ch. 4 we perform some numerical modifications to improve the versatility of the chosen method. Finally, several test cases are addressed in order to guarantee the validity of the proposed method.

The document ends with a chapter devoted to summarize the conclusions and the future work (Ch. 5). Additionally, four appendices are included to complement some parts of the thesis. First, App. A explains how to compute the cinematic properties of a bubble/drop in a level set formulation. Second, App. B gathers some useful calculations in deformable meshes methods. Third, App. C gathers the publications resulting from this research. And fourth, App. D lists the parallel computing resources uses to perform the simulations.

1.5 Preliminary concepts on multiphase DNS

In order to make the following chapters more accessible to the reader, in the present section several founding concept are introduced. Most of this knowledge has been formerly developed in the context of the CTTC research activity (see for instance [24, 26]).

1.5.1 Conservative level set governing equations

Assuming incompressible flow, Newtonian fluids, no mass transfer at the interface between fluids, and constant surface tension coefficient σ, the Navier-Stokes equations governing the fluid motion are written as [24, 47]:

$$\frac{\partial}{\partial t}\left(\rho\mathbf{v}\right)+\nabla\cdot\left(\rho\mathbf{v}\mathbf{v}\right)=-\nabla p+\nabla\cdot\mu\left(\nabla\mathbf{v}+(\nabla\mathbf{v})^{T}\right)+\rho\mathbf{g}+\sigma\kappa\mathbf{n}\delta_{\Gamma} \tag{1.1}$$

$$\nabla\cdot\mathbf{v}=0 \tag{1.2}$$

where t is the time, ρ and μ are respectively the fluid density and viscosity, $\mathbf{v}$ is the velocity field, p is the pressure field, $\mathbf{g}$ is the gravity acceleration, $\mathbf{n}$ is the unit normal vector to the interface, κ is the interface curvature, and δ_{Γ} is the Dirac delta function located at the interface Γ. Finally, ρ and μ can be obtained by the following expressions:

$$\rho=\rho_1 H_1+\rho_2(1-H_1) \tag{1.3}$$

$$\mu=\mu_1 H_1+\mu_2(1-H_1) \tag{1.4}$$

where subscripts 1 and 2 refer respectively to continuous phase (Ω_1) and bubble/drop fluid (Ω_2). H_1 is the Heaviside function, which takes the value of 1 in Ω_1 and 0 in Ω_2. At discretized level, physical properties are smoothed according to the CLS method [18,24], in order to avoid numerical instabilities of the interface.

1.5.2 Interface capturing

The two main difficulties of simulating fluid interfaces are to keep up a sharp interface and to accurately calculate the surface tension [11]. In order to deal with this issues, we use the CLS method to capture the interface [24]. In this method, the following regularized indicator function ϕ is used in order to implicitly represent the interface:

$$\phi(\mathbf{x},t) = \frac{1}{2}\left(\tanh\left(\frac{d(\mathbf{x},t)}{2\varepsilon}\right)+1\right) \tag{1.5}$$

Here, $d(\mathbf{x},t) = \min_{x_\Gamma(t)\in\Gamma}(|\mathbf{x},\mathbf{x}_\Gamma(t)|)$ is the signed distance function and ε is a parameter for controlling the thickness of the interface. This level set function takes the value 0 in the secondary phase, and 1 in the continuous one. It varies continuously along the interface, which can be located by getting the $\phi = 0.5$ isosurface. Based upon this level set function, the fluid properties are regularized as follows:

$$\rho = \rho_1\phi + \rho_2\left(1-\phi\right) \tag{1.6}$$

$$\mu = \mu_1\phi + \mu_2\left(1-\phi\right) \tag{1.7}$$

The level set function is advected by the velocity field obtained from the solution of the Navier-Stokes equations (Eq. 1.1 and 1.2); this yields:

$$\frac{\partial\phi}{\partial t} + \nabla\cdot\phi\mathbf{v} = 0 \tag{1.8}$$

Due to numerical diffusion, the thickness of the interface tends to widen. In order to deal with this problem, a reinitialization equation is used to compress the interface [57]:

$$\frac{\partial\phi}{\partial\tau} + \nabla\cdot\phi\left(1-\phi\right)\mathbf{n}_{\tau=0} = \nabla\cdot\varepsilon\nabla\phi \tag{1.9}$$

where τ is the pseudo-time. This equation consists of a compressive term $\phi\left(1-\phi\right)\mathbf{n}_{\tau=0}$ which compresses the level set function along the unit normal vector $\mathbf{n}$, and of a diffusion term $\nabla\cdot\varepsilon\nabla\phi$, that maintains the characteristic thickness of the profile proportional to $\varepsilon = 0.5h^{0.9}$, where h is the grid size [24].

1.5.3 Surface tension treatment

By using the Continuum Surface Force (CSF) method developed by Brackbill et al. [58] two challenging issues can be handled: the computation of the curvature κ and the application of the resulting pressure jump to the fluids. Following [58], the singular term $\sigma\kappa\mathbf{n}\delta_\Gamma$ is rewritten as a volume force:

$$\sigma\kappa\mathbf{n}\delta_\Gamma = \sigma\kappa\left(\phi\right)\nabla\phi \tag{1.10}$$

where $\mathbf{n}$ and $\kappa\left(\phi\right)$ are given by:

$$\mathbf{n} = \frac{\nabla\phi}{\left\|\nabla\phi\right\|} \tag{1.11}$$

$$\kappa\left(\phi\right) = -\nabla\cdot\mathbf{n} \tag{1.12}$$

Here, $\nabla\phi$ is evaluated by means of the least-squares method [24].

References

[1] C.E. Brennen, Fundamentals of Multiphase Flow. Cambridge University Press, 2005.

[2] R. Perry, D. Green, J. Maloney, Perry's chemical engineers' handbook, McGraw-Hill, New York, 1997.

[3] H.K. Versteeg and W. Malalasekera, An introduction to computational fluid dynamics, Longman Scientific & Techical, 1995.

[4] S.O. Unverdi and G. Tryggvason. Computations of Multi-Fluid Flows. Physica D: Nonlinear Phenomena, 60 (1992), pp. 70-83.

[5] S. O. Unverdi and G. Tryggvason, A front-tracking method for viscous, incompressible, multi-fluid flows, J. Comput. Phys. 100 (1992), pp. 25-37.

[6] Y. J. Jan, Computational Studies of Bubble Dynamics, Ph.D. dissertation, University of Michigan, 1994.

[7] E. A. Ervin and G. Tryggvason, The rise of bubbles in a vertical shear flow, ASME J. Fluid Eng. 119 (1997), pp. 443-449.

[8] E. A. Ervin, Full Numerical Simulations of Bubbles and Drops in Shear Flow, Ph.D. dissertation, University of Michigan, 1993.

[9] B. Bunner and G. Tryggvason, Dynamics of Homogeneous Bubbly Flows. Part 2, Fluctuations of the Bubbles and the Liquid, J. Fluid Mech 466 (2002), pp. 53-84.

[10] B. Bunner and G. Tryggvason, Effect of Bubble Deformation on the Stability and Properties of Bubbly Flows, J. Fluid Mech. 495 (2003), pp. 77-118.

[11] G. Tryggvason, B. Bunner, A. Esmaeeli, D. Juric, N. Al-Rawahi, W. Tauber, J. Han, S. Nas, Y.J. Jan, A Front-Tracking Method for the Computations of Multiphase Flow, J. Comput. Phys. 169 (2001) 708-759.

[12] R. Scardovelli, S. Zaleski, Direct numerical simulation of free surface and interfacial flow, Annu. Rev. Fluid Mech. (1999), 31, 567-603.

[13] M. Sussman and E. Fatemi, An efficient interface-preserving level set redistancing algorithm and its application to interfacial incompressible fluid flow, SIAMJ. Sci. Comput. 20 (1999), pp. 1165-1191.

[14] N. Balcázar, O. Lehmkuhl, L. Jofre, J. Rigola and A. Oliva, A coupled volume-of-fluid/level-set method for simulation of two-phase flows on unstructured meshes Computers and Fluids (2016), 124, 12-19.

[15] M. Sussman, P. Smereka and S. Osher, A Level Set Approach for Computing Solutions to Incompressible Two-Phase Flow, J. Comput. Phys. 144 (1994), pp. 146-159.

[16] M. Sussman, E. Fatemi and P. Smereka, An Improved Level Set Method for Incompressible Two-Phase Flows, Journal of Computers and Fluids 27 (1998), pp. 663-680.

[17] A. Tornberg and B. Engquist, A Finite element based level set method for multiphase flow applications, Computing and Visualization in Science 3 (2000), pp. 93-101.

[18] E. Olsson and G. Kreiss, A conservative level set method for two phase flow, J. Comput. Phys. 210 (2005), pp. 225-246.

[19] E. Marchandise, P. Geuzaine and N. Chevaugeon, A Quadrature free discontinuous Galerkin method for the level set equation, J. Comput. Phys. 212 (2006), pp. 338-357.

[20] E. Olsson, G. Kreiss and S. Zahedi, A conservative level set method for two phase flow II, J. Comput. Phys. 225 (2007), pp. 785-807.

[21] E. Marchandise, P. Geuzaine, N. Chevaugeon and J. Remacle, A stabilized finite elementmethod using a discontinuous level set approach for the computation of bubble dynamics, J. Comput. Phys. 225 (2007), pp. 949-974.

[22] O. Desjardins, V. Moureau and H. Pitsch, An accurate conservative level set/ghost fluid method for simulating turbulent atomization, J. Comput. Phys. 227 (2008), pp. 8395-8416.

[23] R. Croce, M. Griebel and A. Schweitzer, Numerical simulation of bubble and droplet deformation by a level set approach with surface tension in three dimensions, Int. J. Numer. Meth. Fluids 62 (2010), pp. 963-993.

[24] N. Balcázar, L. Jofre, O. Lehmkuhl, J. Castro, J. Rigola, A finite-volume/level-set method for simulating two-phase flows on unstructured grids, Int. J. Multiph. Flow. 64 (2014), pp. 55-72.

[25] N. Balcázar, O. Lehmkuhl, J. Rigola, A. Oliva, A multiple marker level-set method for simulation of deformable fluid particles, Int. J. Multiph. Flow. 74 (2015), pp. 125-142.

[26] N. Balcázar, O. Lehmkuhl, L. Jofre, A. Oliva, Level-set simulations of buoyancy-driven motion of single and multiple bubbles, Int. J. Heat Fluid Flow. 56 (2015), pp. 91-107.

[27] N. Balccázar, J. Rigola, J. Castro and A. Oliva, A level-set model for thermocapillary motion of deformable fluid particles, International Journal of Heat and Fluid Flow 62 (2016), pp. 324-343.

[28] E. Schillaci, L. Jofre, N. Balcázar, O. Lehmkuhl and A. Oliva, A level-set aided single-phase model for the numerical simulation of free-surface flow on unstructured meshes, Computers & Fluids 140 (2016), pp. 97-110.

[29] E. Schillaci, L. Jofre, N. Balcázar, O. Antepara and A. Oliva, A Low-Dissipation Convection Scheme for the Stable Discretization of Turbulent Interfacial Flow, Computers & Fluids 153 (2017), pp. 102-117.

[30] Termo Fluids S.L., web page: http://www.termofluids.com/.

[31] R. Borrell, J. Chiva, O. Lehmkuhl, G. Oyarzun, I. Rodriguez and A. Oliva, Optimising the termofluids CFD code for petascale simulations, Int J Comut Fluid Dyn. 30-6 (2016), pp. 425-430.

[32] N. Balcázar, O. Lehmkuhl, J. Castro, A. Oliva, DNS of the Rising Motion of a Swarm of Bubbles in a Confined Vertical Channel. In: Grigoriadis D., Geurts B., Kuerten H., FrÃ¶hlich J., Armenio V. (eds) Direct and Large-Eddy simulation X. ERCOFTAC Series, vol 24 (2018). Springer, Cham.

[33] N. Balcázar, J. Castro, J. Rigola, A. Oliva, DNS of the wall effect on the motion of bubble swarms, Procedia Computer Science 108 (2017) 2008-2017.

[34] N. Balcázar, O. Lehmkuhl, J. Castro, J. Rigola, A. Oliva, Gravity-driven motion of a swarm of bubbles in a vertical pipe, 27th International Conference on Parallel Computational Fluid Dynamics (2015).

[35] F. Dabbagh, F.X. Trias, A. Gorobets and A. Oliva, On the evolution of flow topology in turbulent Rayleigh-Bénard convection, Physics of fluids 28:11 (2016), pp. 115105-1-115105-25.

[36] L. Paniagua, O. Lehmkuhl, C. Oliet and C. Perez, Large eddy simulations (LES) on the flow and heat transfer in a wall-bounded pin matrix, Numerical heat transfer. Part B, fundamentals 65:2 (2014), pp. 103-128.

[37] J. Ventosa-Molina, O. Lehmkuhl, C. Perez and A. Oliva, Large eddy simulation of a turbulent diffusion flame: some aspects of subgrid modelling consistency, Flow turbulence and combustion 99:1 (2017), pp. 209-238.

[38] L. Jofre, O. Lehmkuhl, J. Castro and A. Oliva, A 3-D volume-of-fluid advection method based on cell-vertex velocities for unstructured meshes, Computers and fluids 94 (2014), pp.244-252.

[39] N. Balcázar, J. Castro, J. Chiva, A. Oliva, DNS of Falling Droplets in a Vertical Channel, International Journal of Computational Methods and Experimental Measurements 6 (2018) 398-410.

[40] E. Schillaci, F. Favre, O. Antepara, N. Balcázar, A. Oliva, Numerical study of an impulse wave generated by A sliding mass, International Journal of Computational Methods and Experimental Measurements 6 (2018) 98-109.

[41] N. Balcázar, Numerical Simulation of Multiphase-Flows: Level-Set Tecniques, Ph.D. Thesis, 2014.

[42] F. Favre, G. Colomer, O. Lehmkuhl and A. Oliva, Numerical simulations of conjugate convection combined with surface thermal radiation using an Immersed-Boundary Method, Journal of Physics: Conference Series 745 (2016).

[43] H. Giraldez, C. Pérez, C. Oliet and A. Oliva, Heat and moisture insulation by means of air curtains: application to refrigerated chambers, International journal of refrigeration 68 (2016), pp.1-14.

[44] S. Danov, C. Pérez, C. Oliet and A. Oliva, Experimental facility for the study of liquid overfeed refrigeration systems and fin-and-tube evaporators 14 (2008), pp. 221-239

[45] J. Castro, A. Oliva, C. Pérez and J. Cadafalch, Evaluation of a small capacity, hot water driven, air-cooled H2O-LiBr absorption machine, HVAC & R research 13 (2007), pp. 59-75.

[46] I. González, A. Naseri, J. Rigola, C.D. Pérez-Segarra and A. Oliva, A fluid-structure interaction solver for the fluid flow through reed type valves, IOP Conference Series: Materials Science and Engineering 232 (2017).

[47] O. Estruch, O. Lehmkuhl, R. Borrell, C. D. Pérez Segarra and A. Oliva, A parallel radial basis function interpolation method for unstructured dynamic meshes, Comput. Fluids. 80 (2013) 44-54.

[48] F.X. Trias, A. Gorobetsa and A. Oliva, A simple approach to discretize the viscous term with spatially varying (eddy-)viscosity, Journal of computational physics 253 (2013), pp. 405-417.

[49] O. Antepara, O. Lehmkuhl, R. Borrell, J. Chiva and A. Oliva, Parallel adaptive mesh refinement for large-eddy simulations of turbulent flows, Computers & Fluids 110 (2015), pp. 48-61.

[50] A. Pont, J. López, J. Rigola and C.D. Pérez-Segarra, Numerical dynamic analysis of reciprocating compressor mechanism. Parametric studies for optimization purposes, Tribology International 105 (2017), pp. 1-14.

[51] D. Gaudlitz and N. Adams, Numerical investigation of rising bubble wake and shape variations, Phys. Fluids. 21 (2009), pp. 1-9.

[52] P. Schlatter, N. Adams and L. Kleiser, A windowing method for periodic inflow/outflow boundary treatment of non-periodic flows, J. Comput. Phys. 206 (2005), pp. 505-535.

[53] J. Nordström, N. Nordin and D. Henningson, The fringe region technique and the Fourier method used in the Direct Numerical Simulation of spatially evolving viscous flows, J. Sci. Comput. 20 (1999), pp. 1365-1393.

[54] H. Marschall, S. Boden, C. Lehrenfeld, D. Falconi, J. Carlos, U. Hampel, A. Reusken, M. Wörner and D. Bothe, Validation of Interface Capturing and Tracking Techniques with different Surface Tension Treatments against a Taylor Bubble Benchmark Problem, Comput. Fluids. 102 (2013), pp. 1-21.

[55] H. Rusche, Computational Fluid Dynamics of Dispersed Two-Phase Flows at High Phase Fractions, PhD thesis, 2002.

[56] M.C. Ruzicka, On bubbles rising in line, Int. J. Multiph. Flow. 26 (2000) pp. 1141-1181.

[57] A. Harten, The artificial compression method for computation of shocks and contact discontinuities. III - Self-adjusting hybrid schemes, Math. Comp. 32 (1978), pp. 363-389.

[58] J.U. Brackbill, D.B. Kothe and C. Zemach, A continuum method for modeling surface tension, J. Comput. Phys. 100 (1992), pp. 335-354.

2

An assessment of domain optimization methods to simulate bubbles dynamics

Abstract. Four domain optimization techniques have been formulated and tested: fringe zone, buffer zone, moving mesh and non-inertial reference frame methods. By using these techniques, small domains can be used in rising bubble simulations, thus saving computational resources. These methods have been implemented in a conservative level set framework. Because some of them require the use of open boundaries, a careful treatment of both inflow and outflow boundaries has been carried out, including the development of a new outflow boundary condition as a variation of the classical convective outflow. Additionally, we carefully studied the domain sizing process, in order to employ the minimum domain capable of capturing the physics of the problem. Validation cases were successfully run in both two and three dimensional configurations.

2.1 Introduction

The bubbly flow is of fundamental importance in a vast variety of engineering applications and natural phenomena. Bubble-laden flows are present in industrial processes

such as solvent extraction, unit operations, bubble columns and extraction columns [1]. To understand these flows, the elemental problem of a single rising bubble should be thoroughly comprehended, laying a solid foundation for the analysis of more complex cases. Buoyant bubble problems need the use of large domains to achieve proper capture of the phenomena. That is due to the need of leaving enough vertical space for the bubble to reach its steady state. This introduces a problem: the loss of computational efficiency due to the resolution of areas with no influence in the calculation of the dynamic properties of the bubble. In effect, at a specific point of the simulation, the region of interest includes the bubble and its surroundings, and also the zones over which the upwind and downwind disturbances are propagated. This region of interest does not include areas far from the bubble, in which the fluid remains totally quiescent.

To avoid this waste of computational resources, several approaches have been tested. In some cases, improving the efficiency is not only advisable but also mandatory, for instance when very fine meshes are needed in order to accurately reproduce small scale turbulent motions. The most usual solution is to reduce the computational domain and impose periodic boundary conditions at its limits. However, this may cause the bubble to interact with its own wake if the length of the domain is not large enough, altering its motion. One solution for this problem could be to use a fringe zone, a region above the rising bubble where the velocity field is reinitialized. Several studies have been published using this method [2–4].

Other approaches can also be adopted by using open boundaries instead of periodic ones. The problem can be formulated employing an Arbitrary Lagrangian-Eulerian (ALE) formulation. In this case, since the mesh is moving along the bubble rise, a short computational domain is enough to capture the evolution of the bubble. Moving Mesh (MM) methods have been broadly used in CFD [5–7]. In particular, it is starting to be applied to bubbles and drops problems [8]. The non-inertial reference frame method is another similar method that can be used with identical aim and which also involves the use of open boundaries. In this method a new reference frame is attached to the bubble centroid, and the dynamics of the bubble are analyzed from this frame. This method has already been used within the context of bubbly flows [9, 10].

As shown above, rising bubbles problems frequently involve the use of open boundaries. A proper design of these boundaries (specially the outflow) could have an overriding impact in the behavior of the simulation. The outflow boundary should allow the outlet of disturbances, with a minimum influence in the rest of the domain. Different approaches have been adopted to deal with outflow boundary conditions in other rising bubbles studies [9, 11, 12]. This work undertakes the task of developing a suitable outflow boundary condition aiming to minimize the global mass error derived from the presence of this boundary. In this regard, a mass correction step is added to the well-known fractional step method [13].

The size of the computational domain is a crucial parameter to study the viability

of a DNS simulation. Bigger domains give rise to bigger meshes, and therefore more resources-consuming simulations. For example, by increasing only a 10% the side of a cubic mesh, the computational expenditure would be more than 130% of the original one. This increment can make the difference between an approachable problem and an unapproachable one. In bubbles and drops problems, the work of Harmathy [14] marked the first step towards a complete domain sizing optimization. In that paper, Harmathy proposed an expression to compute the lateral distance (i.e. from bubble centroid to the lateral walls) while keeping under control the absolute error of the terminal velocity. In the present work, we study the influence of the distances from the bubble centroid to the inflow and outflow, with a view to maintain unaltered the fluid field around the bubble, while keeping a compact domain.

The above-mentioned studies has been put into practice in the problem of a standard rising bubble. This constitutes an essential problem to understand many of the underlying physical phenomena in multiphase flow problems. First, a two-dimensional approach has been conducted, with the aim of making the testing stage more versatile. To this end, the well-known configuration of Hysing et al. [15] has been taken as reference. Additionally, a three dimensional configuration has also been tested, following the work of Balcázar et al. [16].

The work is organized as follows. The problem of reducing the computational domain is explained in Sec. 2.2. The used numerical methods are presented in Sec. 2.3, followed by an in-depth explanation of the needed boundary conditions (Sec. 2.4). In addition, a thoughtful study on the computational domain sizing is presented in Sec. 2.5, in order to provide a procedure to minimize the size of the mesh in rising bubble problems. Thereafter, for the sake of validating the different methods, a set of numerical experiments is carried out in Sec. 2.6. Finally, Sec. 2.7 presents the concluding remarks, together with an assessment of the used methods, in order to choose the one with better performance, which will be selected for the following work of the PhD thesis.

2.2 Domain optimization methods

The present section describes the strategies followed to minimize the domain dimensions. Without these strategies, a large domain would be needed in order to leave enough vertical space for the bubble to rise. This causes a loss of the efficiency due to the fact that regions far from the bubble are being solved. Therefore, the use of the following methods improves the efficiency, and enables finer meshing and/or saving computational resources.

2.2.1 Fringe zone method

The first method considered to reduce the computational domain is based upon avoiding the interaction between the bubble and its own wake in a periodic domain. It is the so-called *fringe zone method*, and was first introduced by Nordström et al. [4]. This method defines a region above the bubble in which the velocity field is reset, leaving a quiescent domain for the approaching bubble. Both up and down boundaries are connected by imposing periodic boundary conditions. Mathematically, the dampening zone is defined as an extra source term in the momentum equation (Eq. 1.1):

$$\Psi_{\text{fringe}} = \frac{1}{\rho}\lambda(\mathbf{x})\mathbf{v} \tag{2.1}$$

where $\mathbf{x}$ is the position vector and $\lambda(\mathbf{x})$ is a fringe function given by:

$$\lambda(y) = \lambda_{\max}\left[S^*\left(\frac{y-y_{\text{start}}}{\Delta}\right) - S^*\left(\frac{y-y_{\text{end}}}{\Delta}+1\right)\right] \tag{2.2}$$

Here, $\lambda_{\max}$ is the maximum amplification factor, y_{start} and y_{end} are respectively the vertical coordinate of the start and the end of the fringe zone, and Δ is the width over which the function ramp up or down. Finally, S^* is the regularized *sigmoid function*:

$$S^*(u) = \begin{cases} 0 & \text{if } u \leq 0 \\ S(u) & \text{if } 0 < u < 1 \\ 1 & \text{if } u \geq 1 \end{cases} \tag{2.3}$$

As is shown in Fig. 2.1, several forms for the sigmoid function $S(u)$ were tested, without finding any relevant difference in the behaviour of the fringe zone source term. Thus, the original formulation of [3] is used, which for the current problem yields the following form:

$$S(u) = \frac{1}{1+\exp\left[\frac{1}{u-1}+\frac{1}{u}\right]} \tag{2.4}$$

Fig. 2.2 depicts the position and shape of the fringe zone in a 2D rectangular domain. As shown in the figure, the definition of the fringe zone is conditioned by the values of the following parameters: $\{s, b, \Delta, \lambda_{\max}\}$. The vertical positions of the start of the fringe zone y_{start} and its end y_{end} are determined by the following relations: $y_{\text{start}} = y_{\text{bubble}} + s$, $y_{\text{end}} = y_{\text{bubble}} + s + b$, where y_{bubble} is the vertical coordinate of the bubble position.

In addition, an extra source term is needed in order to compensate the weight of the fluids within the domain [16]:

$$\Psi_{\rho_0} = -\rho_0\mathbf{g} \tag{2.5}$$

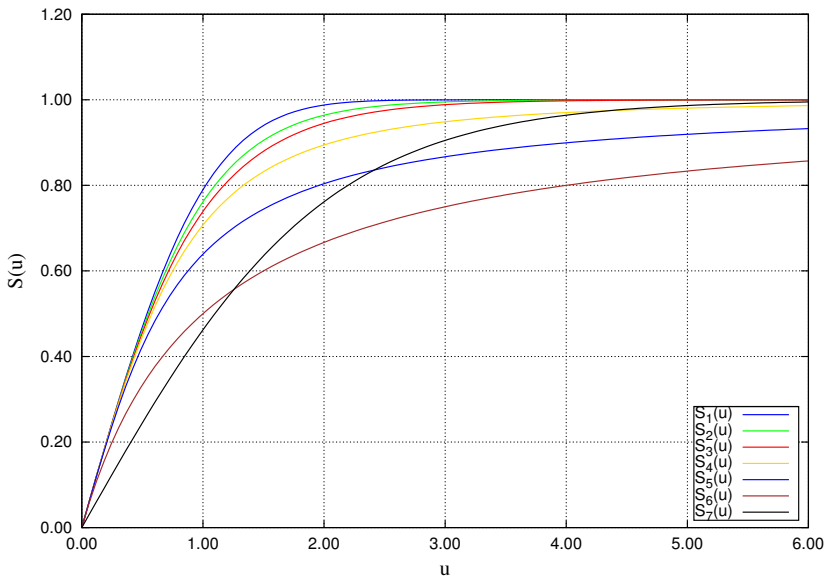

Figure 2.1: Comparison among different normalized sigmoid functions tested: $S_1(x) = \mathrm{erf}\left(\sqrt{\pi}x/2\right)$, $S_2(x) = \tanh(x)$, $S_3(x) = 2\arcsin(\tanh(\pi x/2))/\pi$, $S_4(x) = x/\sqrt{1+x^2}$, $S_5(x) = 2\arctan(\pi x/2)/\pi$, $S_6(x) = x/(1+|x|)$, $S_7(x) = 2/(1+e^{-x}) - 1$.

where ρ_0 is the space averaged density given by:

$$\rho_0 = \frac{1}{V_\Omega}\int_\Omega \rho \mathrm{d}V = \frac{1}{V_\Omega}\int_\Omega \left[\rho_1\, H|_{t=0} + \rho_2\,(1 - H|_{t=0})\right] \mathrm{d}V \tag{2.6}$$

where V_Ω is the domain's volume.

Taken into account the extra source term introduced above, the governing equations to be solved in this method are given by:

$$\frac{\partial}{\partial t}\left(\rho\mathbf{v}\right) + \nabla\cdot\left(\rho\mathbf{v}\mathbf{v}\right) = -\nabla p + \nabla\cdot\mu\left(\nabla\mathbf{v} + (\nabla\mathbf{v})^T\right) + \rho\mathbf{g} + \sigma\kappa\mathbf{n}\delta_\Gamma + \Psi_{\mathrm{fringe}} + \Psi_{\rho_0} \tag{2.7}$$

$$\nabla\cdot\mathbf{v} = 0 \tag{2.8}$$

Immersed boundary formulation

The implementation of a Fringe zone method can be readily carried out in a framework where an Immersed Boundary (`IB`) method is available [17]. By proceeding this way,

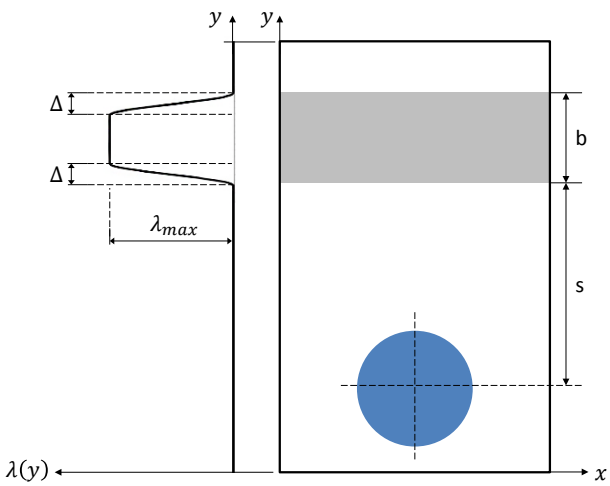

Figure 2.2: Geometrical parameters defining the fringe zone, showed in a two-dimensional domain.

the obtained method is indeed more versatile, as it is capable of dealing with more flow conditions than the traditional approach explained above. However, the implementation may be problematic.

IB methods allow the representation of inner boundaries that do not actually conform the shape of the grid. They do so by imposing Dirichlet conditions in the internal nodes of a moving object, which is represented by means of triangular surface meshes in stereo-lithography format (STL). See [17] for a detailed explanation on these methods. Thus, by defining a dampening inner boundary above the moving bubble, we can impose zero velocity at a specific region of the fluid domain, just as it was done in the previous formulation. This formulation is suitable for situations where the bubble has a strong lateral velocity. In these cases, periodic boundaries should be imposed at the lateral limits. The inner boundary rotates in conjunction with the velocity, so it is able to dampen also the lateral disturbances, acting as a shield against the bubble wake.

Two extra auxiliary objects are needed for the moment in which the main dampening object is crossing one of the boundaries. Those objects move in unison with the leading one, but displaced a fixed distance equal to the longitudinal or transversal length of the domain, respectively. See Fig. 2.3 for a sketch on this method. Additionally, when the leading dampening object completely crosses a boundary, one of the other solids is set as the leading one. The outer solid is then instantaneously moved

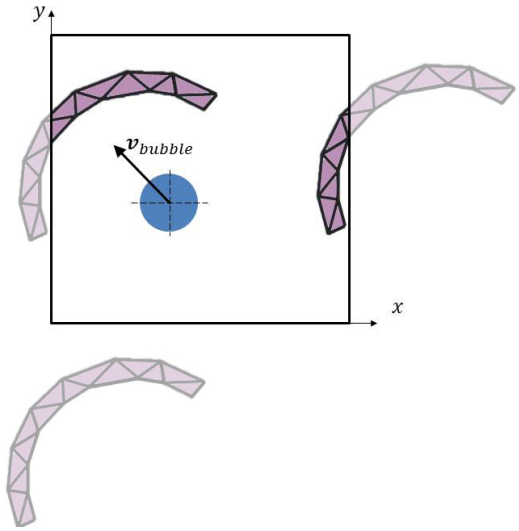

Figure 2.3: Proposed variation of the fringe zone method, based on an immersed boundary approach.

to the position where completes the aforementioned configuration. With this cyclical procedure, a virtual infinite domain is obtained, and an artificial periodic behaviour for the main dampening object is imitated, just as the bubble in the periodic domain.

Although this variation of the fringe zone is more versatile, the method comparison carried out throughout the present chapter has been performed using the standard approach, since it is easier to implement and less likely to introduce computational errors.

2.2.2 Buffer zone method

As a variation of the previous one, we have developed the buffer zone method. This artificial high-viscosity regions have been broadly used in CFD, especially to dampen the disturbances before an outflow boundary condition. Here, we enforced of a moving region in which the viscosity of the fluid is notably increased. With this strategy, the buffer zone dampens the velocity field, leaving a mainly unaltered domain.
The viscosity field is updated each time step as follows:

$$\mu = \lambda(\mathbf{x})\left[\mu_0 H + \mu_1 (1-H)\right] \tag{2.9}$$

where $\lambda(\mathbf{x})$ is given by Eq. 2.2. As with the fringe zone method, the additional source

term Φ_{ρ_0} is needed to compensate the weight of the fluids within the domain. Therefore, governing equations can be written as:

$$\frac{\partial}{\partial t}\left(\rho\mathbf{v}\right)+\nabla\cdot\left(\rho\mathbf{v}\mathbf{v}\right)=-\nabla p+\nabla\cdot\mu\left(\nabla\mathbf{v}+(\nabla\mathbf{v})^T\right)+\rho\mathbf{g}+\sigma\kappa\mathbf{n}\delta_\Gamma+\Psi_{\rho_0} \tag{2.10}$$

$$\nabla\cdot\mathbf{v}=0 \tag{2.11}$$

2.2.3 Moving mesh method

Using this method, an Arbitrary Lagrangian-Eulerian approach is adopted to describe the problem. The momentum equation given in Eq. 1.1 is mildly modified as follows:

$$\frac{\partial}{\partial t}\left(\rho\mathbf{v}\right)+\nabla\cdot\left(\rho\mathbf{v}(\mathbf{v}-\mathbf{v}_{\text{domain}})\right)=-\nabla p+\nabla\cdot\left(\mu\nabla\mathbf{v}+\mu(\nabla\mathbf{v})^T\right)+\rho\mathbf{g}+\sigma\kappa\mathbf{n}\delta_\Gamma \tag{2.12}$$

where $\mathbf{v}_{\text{domain}}$ is the velocity of the computational domain, which for this specific case is identical to the vertical component of the bubble velocity (see Ap. A). Numerical details about this method for incompressible single phase flow can be found in [5]. The algorithm derived in that paper has been simplified to take into account that the mesh is just linearly translated, without deformation. Fig. 2.4 shows a diagram on how this method works. The mesh is moving at the vertical velocity of the bubble, so apparently the bubble stays vertically stationary inside the mesh domain.

A zero-velocity inlet boundary condition is imposed at the top of the domain and an outlet boundary condition at its bottom. These boundary conditions are explained in detail in Sec. 2.4.

2.2.4 Space conservation Law

When an Arbitrary Lagrangian-Eulerian approach is adopted, the computational volume should be preserved. This is done by using the so-called Space Conservation Law (SCL) [5]:

$$\frac{d}{dt}\int_{\Omega_{\text{CV}}}\mathrm{d}\Omega_{\text{CV}}+\int_S\mathbf{v}_g\cdot\mathbf{n}\mathrm{d}S=0 \tag{2.13}$$

where Ω_{CV} is a moving control volume (CV), S is its closed surface, and $\mathbf{v}_g$ is the surface velocity whose outward unit vector is represented by $\mathbf{n}$. The mass conservation is then procured by enforcing this SCL. Actually, only mass flux through a cell c needs to be modified as follows:

$$\dot{m}_c^{\text{modified}}=\int_{S_c}\rho\left(\mathbf{v}-\mathbf{v}_g\right)\cdot\mathbf{n}\mathrm{d}S\approx\rho_c\left(\mathbf{v}\cdot\mathbf{n}\right)_c S_c-\rho_c\left(\mathbf{v}_g\cdot\mathbf{n}\right)_c S_c \tag{2.14}$$

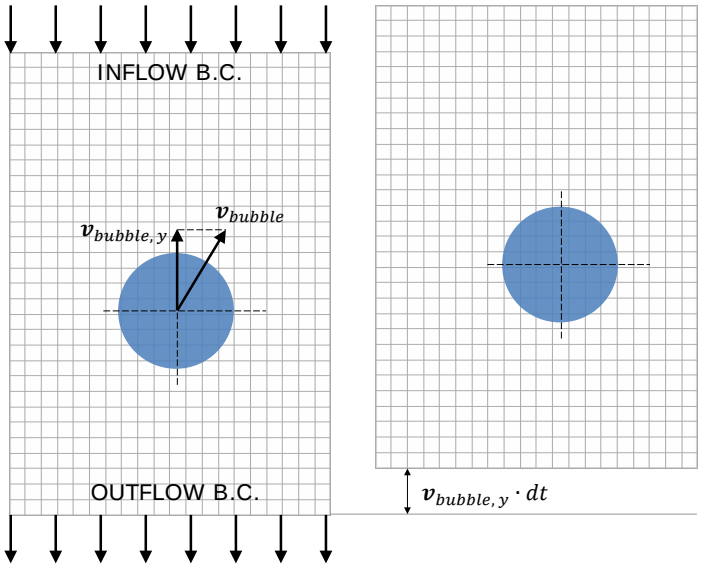

Figure 2.4: Schematic representation of the moving mesh method, showing two consecutive time instants. The mesh displacement is calculated as the product of the current time step and the bubble vertical velocity.

where subscript c denotes that the corresponding variable is evaluated at cell c. The term $(\mathbf{v}_g \cdot \mathbf{n})_c S_c$ represents the volume swept by the CV face c per unit of time (see Fig. 2.5). As the mesh is trivially moved without deformation at a velocity $\mathbf{v}_{\text{domain}}$ equal to the bubble's vertical velocity, the calculation of the this swept volume is straightforward.

2.2.5 Non-inertial reference frame method

In this method a non-inertial frame of reference is attached to the projection of the bubble's centroid over the vertical central axis. As in the moving mesh method, the bubble apparently remains vertically still, although it can move sideways. Fig. 2.6 depicts a sketch of this method. The frame of reference of the studied domain is now non-inertial, and its acceleration is considered by means of adding the corresponding virtual forces Ψ_{virtual} to the momentum equation (Eq. 1.1). As the movement of the domain is just linear, the inertial forces due to the rotation of the reference system are not presented [18]; this yields:

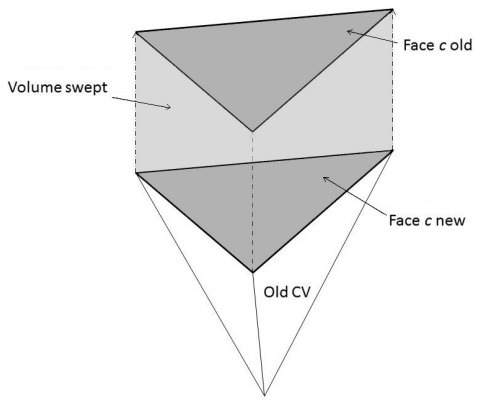

Figure 2.5: Volume swept by the CV face c in the movement of the mesh.

$$\Psi_{\text{virtual}} = -\rho a_{\text{bubble},y} \hat{\mathbf{u}}_y \tag{2.15}$$

where $a_{\text{bubble},y}$ is the vertical component of the bubble acceleration (see App. A) and $\hat{\mathbf{u}}_y$ is the vertical unit vector.

In the same way as the moving mesh method, an inlet boundary condition is used at the top of the domain and an outlet boundary condition at its bottom. See Sec. 2.4 for details on the formulation of the inflow/outflow boundary conditions. At the inflow boundary condition the velocity is set to the vertical value of the bubble velocity $\mathbf{v}_{\text{bubble}}$, with the sign reversed.

2.3 Numerical methods

The aforementioned numerical procedures have been implemented on a collocated unstructured grid arrangement by means of the finite-volume method, according to [19]. A Central Difference (CD) scheme is used to discretize the diffusion terms of the governing equations (Eqs. 1.1 and 1.9). A Superbee flux limiter adapted to unstructured meshes [19] is used to discretize the convective term of the advection equation Eq. 1.8, and a CD scheme is used for the convective term of the momentum equation, Eq. 1.1. For time discretization, a 3-step-third-order accurate TDV Runge-Kutta scheme [20] is used for advection and reinitialization equations (Eqs. 1.8 and 1.9). Finally, CD schemes are used for the compressive and diffusive terms of the reinitialization equation, Eq. 1.9 [21]. For the non-inertial reference frame method (Sec. 2.2.5), the acceleration of the bubble has been calculated from its velocity by means of a second order

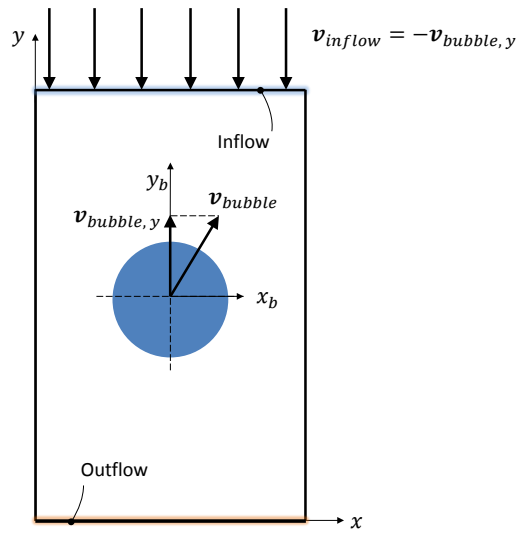

Figure 2.6: Sketch of the non-inertial reference frame method, showing configuration and boundary conditions used.

finite difference scheme (see. A).

The pressure-velocity coupling is solved by means of a Fractional Step method [13, 19, 22, 23]. Momentum equation (Eq. 1.1) is computed in two steps:

$$\frac{\rho \mathbf{v}^{\mathrm{p}} - \rho^n \mathbf{v}^n}{\Delta t} = \nabla \cdot \left[\rho \mathbf{v}^n \left(\mathbf{v}^n - \mathbf{v}^n_{\mathrm{domain}}\right)\right] + \nabla \cdot \mu \left(\nabla \mathbf{v}^n + \nabla^T \mathbf{v}^n\right) + \rho \mathbf{g} + \sigma \kappa \nabla \phi + \Psi \tag{2.16}$$

where $\mathbf{v}^{\mathrm{p}}$ is the predictor velocity of the Fractional Step method. For simplicity, this equation is discretized using an explicit Euler scheme, however and explicit Adams-Bashforth scheme has been used for computations. Eq. 2.16 is applicable in all the presented methods, taking into account that $\mathbf{v}_{\mathrm{domain}} = 0$ except in the moving mesh method, and Ψ depends on the selected method. The next step of the fractional step method is the calculation of the following expression:

$$\mathbf{v}^{n+1} = \mathbf{v}^{\mathrm{p}} - \frac{\Delta t}{\rho} \nabla p^{n+1} \tag{2.17}$$

Now, by adding the continuity equation (Eq. 1.2), the following Poisson equation is

obtained to solve the pressure:

$$\nabla \cdot \left(\frac{1}{\rho} \nabla p^{n+1} \right) = \frac{1}{\Delta t} \nabla \cdot \mathbf{v}^{\mathrm{p}} \tag{2.18}$$

The discretization of this equation leads to a linear system, which is solved by means of a preconditioned conjugate gradient method. Cell-face velocity is calculated according to [19, 23], in order to avoid pressure-velocity decoupling and to fulfill the incompressible constraint. This cell-face velocity is used to advect the CLS function in Eq. 1.8 and momentum in Eq. 1.1.

The characteristic interface thickness is $\varepsilon = \mathscr{C}_\varepsilon (\Delta_n)^\alpha$, where $\mathscr{C}_\varepsilon = 0.5$. The parameter α is set to 1 in the fringe zone, buffer zone and the moving mesh methods, and to 0.9 in the non-inertial reference frame method. A lower parameter α helps to avoid numerical instabilities, but at the price of artificially widen the interface thickness.

An extra particular treatment of the non-inertial reference frame method is also needed for the discretization of the convective term in the momentum equation (Eq. 1.1). Whilst a central difference (CD) scheme can be used in fringe zone and moving mesh methods, an upwind scheme is required in the non-inertial reference frame method, which introduce numerical diffusion. For a detailed discussion about the influence of convective schemes in the buoyancy-driven motion of single bubbles, see [16].

2.3.1 Time step

A CFL type condition is used to dynamically determine an admissible time step for stable computations. By a straightforward comparison among the terms of the momentum equation (Eq. 1.1), the following relations are obtained. The convective time step condition is:

$$(\Delta t)_{\mathrm{conv}} \leq \min \left(\frac{\Delta^n}{\|\mathbf{v}^n\|} \right) \tag{2.19}$$

where superscript n denotes that the corresponding variable is evaluated at the node n under consideration, and Δ^n is the characteristic size of the control volume n calculated as the cubic root of the cell volume. The viscous time step restriction is calculated as follows:

$$(\Delta t)_{\mathrm{visc}} \leq \min \left(\frac{(\Delta^n)^2 \rho^n}{\mu^n} \right) \tag{2.20}$$

Furthermore, the gravity source term gives the following restriction:

$$(\Delta t)_{\mathrm{g}} \leq \sqrt{\min \left(\frac{\Delta^n}{g} \right)} \tag{2.21}$$

where $g = \|\mathbf{g}\|$. Finally, the surface tension source term gives [36]:

$$(\Delta t)_{\text{cap}} \leq \min\left(\left(\frac{\rho_1 + \rho_2}{4\pi\sigma}\right)^{1/2} \left(\Delta^n\right)^{3/2}\right) \tag{2.22}$$

For some specific methods, other time step restrictions should be taken into account. For instance, in the fringe zone method:

$$(\Delta t)_{\text{fringe}} \leq \min\left(\frac{\rho^n}{\lambda_{\max}}\right) \tag{2.23}$$

For the methods using the extra source term Φ_{ρ_0}, the following conditions should also be imposed:

$$(\Delta t)_{\rho_0} \leq \sqrt{\min\left(\frac{\rho^n \Delta^n}{\rho_0 g}\right)} \tag{2.24}$$

For the moving mesh method the following condition should be imposed:

$$(\Delta t)_{\text{mesh}} \leq \min\left(\frac{\Delta^n}{\|\mathbf{v}_{\text{domain}}\|}\right) \tag{2.25}$$

and for the non-inertial reference frame:

$$(\Delta t)_{\text{accel}} \leq \sqrt{\min\left(\frac{\Delta^n}{|a_{\text{bubble},y}|}\right)} \tag{2.26}$$

Finally, the global stability condition for the fringe zone method is given by:

$$\Delta t \leq \min\left((\Delta t)_{\text{conv}}, (\Delta t)_{\text{visc}}, (\Delta t)_{\text{g}}, (\Delta t)_{\text{cap}}, (\Delta t)_{\text{fringe}}, (\Delta t)_{\rho_0}\right) \tag{2.27}$$

for the buffer zone method

$$\Delta t \leq \min\left((\Delta t)_{\text{conv}}, (\Delta t)_{\text{visc}}, (\Delta t)_{\text{g}}, (\Delta t)_{\text{cap}}, (\Delta t)_{\rho_0}\right) \tag{2.28}$$

for the moving mesh method:

$$\Delta t \leq \min\left((\Delta t)_{\text{conv}}, (\Delta t)_{\text{visc}}, (\Delta t)_{\text{g}}, (\Delta t)_{\text{cap}}, (\Delta t)_{\text{mesh}}\right) \tag{2.29}$$

and for the non-inertial reference frame method:

$$\Delta t \leq \min\left((\Delta t)_{\text{conv}}, (\Delta t)_{\text{visc}}, (\Delta t)_{\text{g}}, (\Delta t)_{\text{cap}}, (\Delta t)_{\text{accel}}\right) \tag{2.30}$$

2.3.2 Calculation algorithms

Depending on the selected method, a different calculation process should be carried out in order to advance from the current time step t^m to the following one t^{m+1}. Algs. 1, 2 and 3 summarize these different algorithms for the methods studied in this work.

Algorithm 1 Fringe zone and buffer zone methods

repeat:

Choose a suitable time step, as explained in Sec. 2.3.1.
Advect the level set function ϕ by solving Eq. 1.8.
Compress the interfaces between both fluids by solving Eq. 1.9.
Update the density, viscosity and curvature fields.
Calculate the predictor velocity.
Solve the Poisson equation to get the pressure field.
Compute the velocity at the faces [19]
Calculate the final velocity.

Fractional step method

until $t > t_{\text{end}}$

Algorithm 2 Moving mesh method

repeat:

Calculate the mesh velocity, as explained in Sec. 2.2.3.
Choose a suitable time step, as explained in Sec. 2.3.1.
Advect the level set function ϕ by solving Eq. 1.8.
Compress the interfaces between both fluids by solving Eq. 1.9.
Update the density, viscosity and curvature fields.
Calculate the predictor velocity.
Perform the mass conservation step explained in Sec. 2.4.3.
Solve the Poisson equation to get the pressure field.
Compute the velocity at the faces [19]
Calculate the final velocity.

Fractional step method

Move the mesh.

until $t > t_{\text{end}}$

Algorithm 3 Non-inertial reference frame method

repeat:

Calculate the bubble velocity and its acceleration, as explained in App. A.
Choose a suitable time step, as explained in Sec. 2.3.1.
Advect the level set function ϕ by solving Eq. 1.8.
Compress the interfaces between both fluids by solving Eq. 1.9.
Update the density, viscosity and curvature fields.
Calculate the predictor velocity.
Perform the mass conservation step explained in Sec. 2.4.3.
Solve the Poisson equation to get the pressure field.
Compute the velocity at the faces [19]
Calculate the final velocity.

Fractional step method

until $t > t_{\text{end}}$

2.4 Boundary conditions treatment

The different methods presented above can be used both in two- and three-dimensional problems. In the two-dimensional case, the bubble rises in a rectangular shaped domain, while in the three-dimensional case the domain is a cylinder, in order to have a constant distance from the bubble centroid to the lateral walls. In both cases, three kinds of boundaries can be identified: a lateral boundary, consisting of both side walls parallel to the gravity vector for the 2D case and all the curved side of the cylinder for the 3D case; an upper boundary, which for both cases is the side to which the bubble is directed; and a lower boundary, which is the domain limit from which the bubble moves away. These upper and lower limits are not physical, they do not exist in reality. They are used in order to limit the computational domain, as explained in Sec. 2.1. In the lateral boundary, either free slip or non slip boundary condition is imposed (see Sec. 2.6). The conditions applied in the other boundaries change depending on the method used, as is described in previous sections. The numerical treatment of these conditions is explained below.

2.4.1 Periodic boundary condition

In the fringe zone and buffer zone methods, a periodic boundary condition is imposed at the upper and lower domain limits, linking both boundaries. This is accomplished by imposing the following condition on the corresponding boundary faces:

$$\gamma_{\text{upper}} = \gamma_{\text{lower}} \qquad ; \qquad \gamma = \{\mathbf{v}, p, m\} \tag{2.31}$$

where m is the mass flux across these faces, and subscripts *upper* and *lower* refer to the property at that respective boundary face.

2.4.2 Inflow boundary condition

An inflow boundary condition is needed in the moving mesh and the non-inertial reference frame methods. This boundary condition aims to achieve a well-defined flow profile at the boundary. The formulation we used is based upon specifying the velocity vector at the corresponding boundary and using a zero gradient condition for the pressure. These conditions are readily implemented, but the boundary needs to be carefully placed far enough from the bubble. Hence, its interaction with the propagated upstream disturbances is avoided, or at least it is restricted to a negligible effect on the whole flow structure, specially near the bubble. See Sec. 2.5.2 for further notes about the placement of this boundary.

2.4.3 Outflow boundary condition

As well as the inflow boundary condition, an outflow boundary condition is also required in some of the methods tested in this work (namely, moving mesh and non-inertial reference frame methods). However, the numerical implementation of the outflow boundary condition is much more burdensome. The real infinite domain is truncated by the outflow boundary, and it would be desirable that this limit is placed sufficiently far to prevent it from interacting with the region of interest. In spite of that, due to practical computational considerations, the boundary is usually placed not so far from the bubble, so a suitable outflow boundary condition is necessary. An incorrect placement of this boundary or an improper choice of the boundary condition might seriously affect the motion of the bubble. In general, there are three desirable features that an effective outflow boundary condition must have [25]: it should allow the flow to exit the domain with a smooth discharge of disturbances, it should have a minimum effect on the flow near the outlet, and it should have a negligible effect on the bubble motion.

The approach taken in the formulation of the outflow boundary condition was to minimize the global mass error, due to the importance of this factor in terms of numerical stability, and to be coherent with the conservative level set formulation used [19]. This is not the only criterion to tackle the task of designing the outlet; other criteria could also be adopted in order to get a suitable boundary condition (for instance, to minimize the local mass error, to minimize the mesh requirements near the boundary, etc.).

The formulation of our outflow boundary condition is based upon a combination of the well-known convective boundary condition (CCB) explained for instance in [26] and the outflow used by Davis and Moore [27]. As the fractional step method is going to be used to solve the Navier-Stokes equations [13], a condition for calculating the predictor velocity $\mathbf{v}^{\mathrm{p}}$ in the boundary should be given. In this regard, a convective boundary

condition is used:

$$\frac{\partial \mathbf{v}_*^{\mathrm{p}}}{\partial t} + \mathcal{V}_{\mathrm{C}} \frac{\partial \mathbf{v}_*^{\mathrm{p}}}{\partial n} = 0 \tag{2.32}$$

where n indicates the boundary face normal direction and $\mathcal{V}_{\mathrm{C}}$ is the convective velocity. A characteristic velocity of the problem should be used as $\mathcal{V}_{\mathrm{C}}$. We assumed $\mathcal{V}_{\mathrm{C}} = \|\mathbf{v}_{\mathrm{bubble}}\|$, but other options were also tested (for instance, $\mathcal{V}_{\mathrm{C}} = U_T$, where U_T is the expected terminal velocity of the bubble), with negligible differences in the obtained results. Eq. 2.32 is discretized by using an Euler scheme in time. The variable $\mathbf{v}_*^{\mathrm{p}}$ is not the predictor velocity for the fractional step method. A correction mass step is carried out at this point, in order to ensure the global mass conservation of the calculated pseudo-velocity field. The correction mass process differs from others used in the literature and is explained in detail at thi end of the current section.
The employed discrete form of Eq. 2.32 yields:

$$\mathbf{v}_*^{\mathrm{p}} = \mathbf{v}_b - \frac{\Delta t}{\|\Delta \mathbf{x}_{b\to nb}\|} \mathcal{V}_{\mathrm{C}} (\mathbf{v}_b - \mathbf{v}_{nb}) \tag{2.33}$$

where subscript b denotes that the corresponding variable is evaluated at the boundary node, subscript nb denotes the neighbor node, Δt is the current time step and $\|\Delta \mathbf{x}_{b\to nb}\|$ is the distance between the boundary node and its neighbor node.

At this point, the pressure at the boundary nodes is set to the corrected hydrodynamic pressure. For the moving mesh method, it yields:

$$p = \rho \mathbf{g}\mathbf{x} \tag{2.34}$$

and for the non-inertial reference frame method:

$$p = \rho \mathbf{g}\mathbf{x} + \rho a_{\mathrm{bubble},y} y \tag{2.35}$$

The outflow boundary surface of all tested cases is perpendicular to the gravity vector $\mathbf{g}$ and also to the acceleration of the non-inertial reference frame (for the non-inertial method). Therefore, any constant pressure (for instance, $p = 0$) can be imposed at this boundary. Once the pressure is obtained at those nodes, the velocity is computed following the fractional step method [13].

As explained before, the design of this boundary aims to minimize the global mass error. This error is directly related to the global volume error E_{V}, which compares the initial bubble volume with the current one. It is defined as follows:

$$E_V = \frac{V_{\Omega_2} - V_{\Omega_2}^0}{V_{\Omega_2}^0} \tag{2.36}$$

where V_{Ω_2} is the volume of the bubble at the current time step and $V_{\Omega_2}^0$ is its initial one. This error is computed numerically as:

$$E_V = \frac{\sum_n \phi_n V_n - \sum_n \phi_n^0 V_n}{\sum_n \phi_n^0 V_n} \tag{2.37}$$

where ϕ_n is the level set function evaluated at the node n, ϕ_n^0 is again the level set function at the node n, but at the initial state, and V_n is the volume of the corresponding cell.

Tab. 2.1 and Fig. 2.7 show a comparison between different outflow boundary conditions, including the one proposed in the present section. Tab. 2.1 shows the average and maximum global volume error E_V for a fixed number of iterations (1000) in the resolution of a two dimensional rising bubble problem (see Sec. 2.6.1 for further details about this problem). It is shown that the conservative convective boundary condition (CCBC) proposed in this work has the best behavior in terms of global volume error. The only boundary condition that has an error of the same order is the Neumann boundary condition (NBC). However, the outlet of disturbances is not correctly reproduced by using NBC. Additionally, Fig. 2.7 shows the evolution of this global error along iterations.

Type of Outflow	Formulation	Average E_V	Maximum E_V
Conserv. Convective	(Described in the text)	$7.10 \cdot 10^{-14}$	$1.45 \cdot 10^{-13}$
Simple Convective	$\frac{\partial \mathbf{v}}{\partial t} + \mathcal{V}_C \frac{\partial \mathbf{v}}{\partial n} = 0$	$3.82 \cdot 10^{-6}$	$5.61 \cdot 10^{-6}$
Neumann	$\frac{\partial \mathbf{v}}{\partial n} = 0$	$7.29 \cdot 10^{-14}$	$1.45 \cdot 10^{-13}$
Davis [27]	$\frac{\partial \mathbf{v}}{\partial n} = 0\,, p = p^*$	$5.26 \cdot 10^{-6}$	$9.95 \cdot 10^{-6}$
Christer [28]	$\frac{\partial^3 \mathrm{v}_n}{\partial n^3} = 0\,, \frac{\partial^2 \mathrm{v}_\theta}{\partial n^2} = 0\,, p = p_0$	$6.63 \cdot 10^{-7}$	$2.22 \cdot 10^{-6}$
Shirayama [29]	$\frac{\partial^2 \mathbf{v}}{\partial n^2} = 0$	$2.26 \cdot 10^{-4}$	$8.09 \cdot 10^{-4}$
Magnaudet [30]	$\frac{\partial^2 \mathrm{v}_n}{\partial n^2} = 0\,, \frac{\partial \mathrm{v}_\theta}{\partial n} = 0\,, \frac{\partial p}{\partial n \partial \theta} = 0$	$1.14 \cdot 10^{-3}$	$2.84 \cdot 10^{-3}$

Table 2.1: Comparison between the different outflow boundary conditions tested in a two-dimensional rising bubble problem, where E_V is the global volume error, $\mathcal{V}_C$ is the convective velocity, n and θ indicate directions normal and tangential to the outer boundary, v_n and v_θ refer the normal and tangential velocity components, p^* is the corrected hydrodynamic pressure, and p_0 is a fixed pressure.

Mass correction

As it is explained above, the outflow boundary condition requires a mass correction step which is performed after calculating the pseudo-velocity field. In the literature, this is usually done by adding the corrective mass m^{cor} to the mass flow m of the

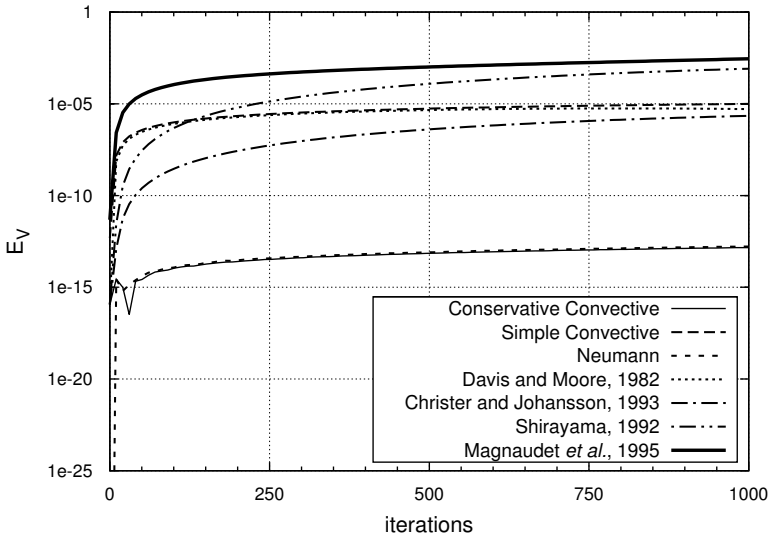

Figure 2.7: Evolution of the global volume error E_V for different outflow boundary conditions tested in a two-dimensional rising bubble problem.

corresponding outflow boundary node [25]:

$$m_b^{\text{cor}} = \sum_{bf} m_b \frac{A_b}{\sum_{obf} A} \tag{2.38}$$

where A is the face area. Subscript b denotes that the corresponding variable is evaluated at the boundary node under consideration. Summation $\sum_{bf} m_b$ is performed over all boundary faces in the entire domain and summation $\sum_{obf} A$ is performed just over the outflow boundary faces. This method for mass correction might have the drawback of the formation of large local mass errors in the corner cells of the domain due to the physical characteristics of the problem, causing numerical instabilities. In order to avoid this issue, a modified mass correction step is proposed. Fig. 2.8 shows a graphic interpretation of the simple mass correction method and the one presented in this work.

In this way, the global mass balance error Δm is distributed on a weighted basis over the outflow boundary nodes. A weighting coefficient w is assigned to each node of the outflow boundaries, so that the nodes near the corners have small coefficients, and the central nodes have larger ones. The distribution of these weights is based on the

following formula:

$$w_b = \frac{\mathbf{v}_{\text{bubble}} \cdot \mathbf{n}}{\|\mathbf{v}_{\text{bubble}}\| \cdot \|\mathbf{n}\|} \exp\left\{ -\frac{1}{2}\chi \left[\left(\alpha - \frac{S_\alpha}{2}\right)^2 + \left(\beta - \frac{S_\beta}{2}\right)^2 \right] \right\} \tag{2.39}$$

where χ is a shape control parameter of the weight function ($\chi = 1$ by default), α and β are curvilinear coordinates over the boundary surface, and S_α and S_β are projections of the surface in α and β directions, respectively. Other similar weight functions were also tested, with negligible differences in the obtained results. The previous expression can be rewritten for general cases, with an homogeneous bubble motion and an ordinary domain. For instance, for the two-dimensional rising bubble problem (see Sec. 2.6.1), the following formula can be used:

$$w_b = \exp\left\{ -\frac{1}{2}\chi \left(x - \frac{S_x}{2} \right)^2 \right\} \tag{2.40}$$

2.5 Domain sizing

The current section presents an study on the size of the computational domain, which is a crucial parameter to study the viability of the multiphase simulations. Small differences in the dimensions of the computational domain could give rise to big differences in the mesh size, compromising the viability of the study case.

2.5.1 Lateral boundaries placement

The lateral distance from bubble centroid to the lateral walls should be enough to not constrict the motion of the drop. This constriction has a dampen effect on the terminal velocity of the bubble. Harmathy [14] proposed the following expression to compute the lateral distance while keeping under control the terminal velocity error:

$$\frac{U_T}{U_T^\infty} \simeq 1 - \left(\frac{d}{D}\right)^2 \tag{2.41}$$

where U_T^∞ represents the terminal velocity in an infinite domain, U_T is the actual terminal velocity, d is the bubble's diameter and D is the diameter of the computational domain. U_T^∞ can be taken from the graphs shown in Fig. 2.9. We adopted this expression throughout the present work to compute the lateral distance, taken 3% as an acceptable threshold of the absolute error of the terminal velocity.

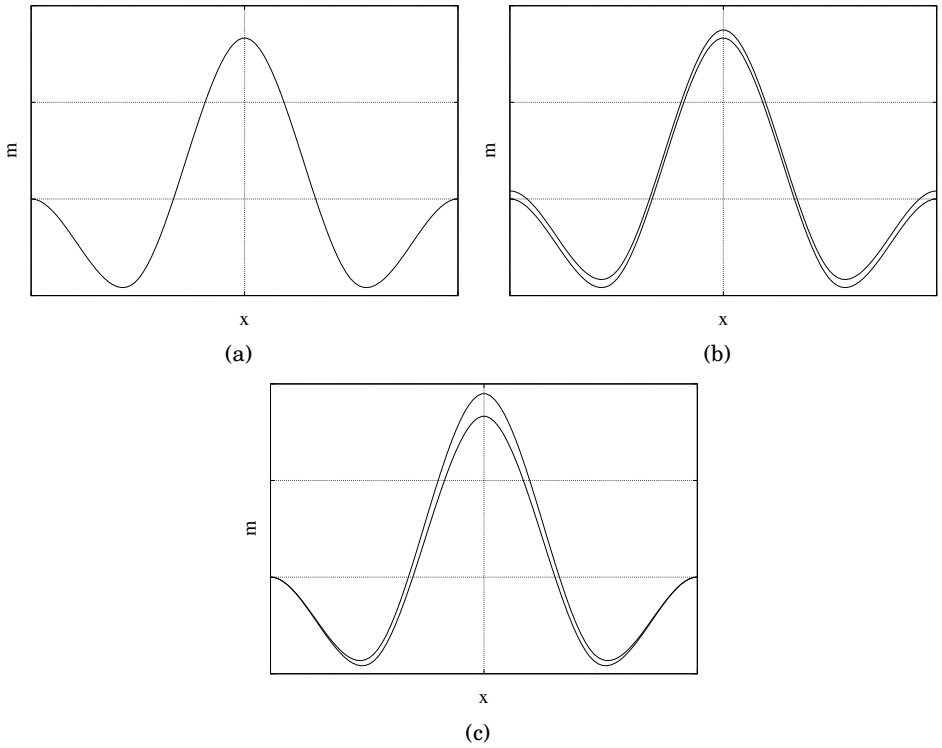

Figure 2.8: Sketch of the mass correction step, showing (a) the mass profile at an outflow boundary without correction, (b) this profile after a simple mass correction step and (c) this same profile after performing the improved correction step.

2.5.2 Inlet placement

The placement of the inflow boundary has a strong influence in the terminal velocity of the bubble. By placing it too close to the bubble, the upper surrounding flow could be underdeveloped, causing a reduction of the terminal velocity of the bubble. A statistical analysis has been carried out at this point, aiming to obtain a procedure to compute a suitable inlet distance, in a manner similar to Harmathy's equation [14] (Eq. 2.41) for the lateral distance.

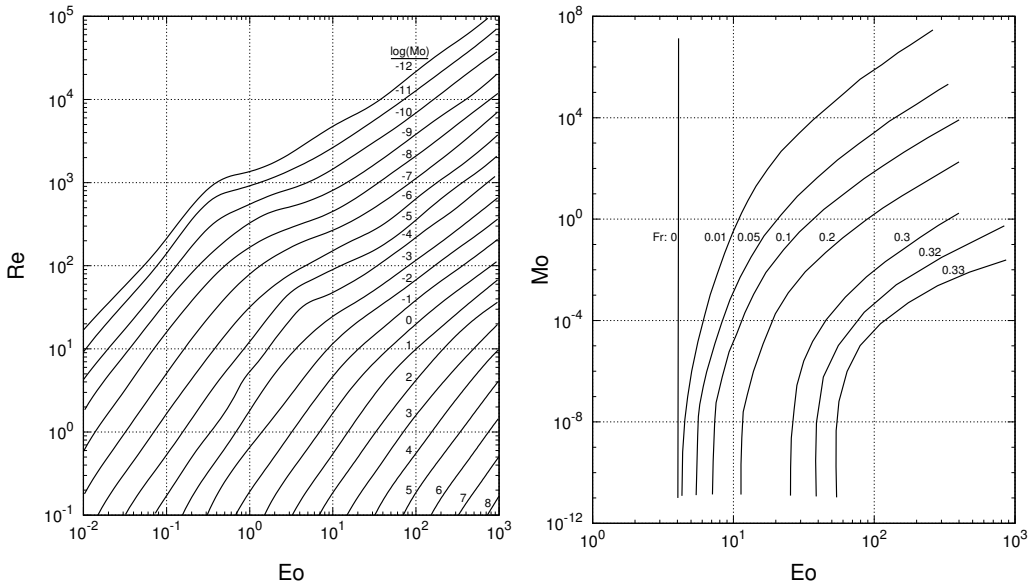

(a) (b)

Figure 2.9: Useful diagrams to obtain tentative values of the rising velocity in both (a) constrained or (b) unconstrained rising bubbles. Diagrams are reproduced from those represented in [33] and [34], respectively.

Regression analysis

Given a discrete set of results that relates the distance h_i from the bubble to the inlet and the error in the terminal rise velocity, a non-linear regression analysis can be carried out. By doing this study, an analytical expression can be obtained. This expression can be used to calculate the expected lost of accuracy in a given domain size.

The original dataset for this statistical study is presented in Tab. 2.2. For each of these sets of parameters, different simulations were run varying the distance from the bubble to the inflow. Long distances from bubble centroid to lateral and outlet boundaries were used.

A base of exponential functions is used to fit the results from the aforementioned test cases. We found that, by retaining the first five terms of the series, enough accuracy is achieved. Thus, by following the process given by [32], the following equation is

Case label	Eo	Mo
A	1.0	10^{-2}
B	1.0	10^{-4}
C	1.0	10^{-6}
D	9.0	10^{-2}
E	9.0	10^{-4}
F	9.0	10^{-6}
G	90.0	10^{-2}
H	90.0	10^{-4}
I	90.0	10^{-6}

Table 2.2: Flow conditions taken into account to obtain Eq. 2.42 by a regression analysis, as explained in the text.

obtained:

$$\begin{aligned} E_U = 1 - C_0(Eo,Mo) + C_1(Eo,Mo)\cdot\exp\left\{\frac{h_i}{d}\right\} + C_2(Eo,Mo)\cdot\exp\left\{2\frac{h_i}{d}\right\} \\ + C_3(Eo,Mo)\cdot\exp\left\{3\frac{h_i}{d}\right\} + C_4(Eo,Mo)\cdot\exp\left\{4\frac{h_i}{d}\right\} \end{aligned} \tag{2.42}$$

Here, $E_U = \left|U_T - U_T^\infty\right|/U_T^\infty$ is the absolute error of the terminal velocity. The coefficients $C_n(Eo,Mo)$ are adjusted by two-dimensional log-linear regression:

$$C_n(Eo,Mo) = c_{n1} + c_{n2}\cdot\log(Eo) + c_{n3}\cdot\log(Mo) \tag{2.43}$$

where c_{nk} are the regression constants. Tab. 2.3 provides the expressions to compute the coefficients $C_n(Eo,Mo)$.

$C_n(Eo,Mo)$
$C_0(Eo,Mo) = 1.200 - 0.023\log(Eo) + 0.033\log(Mo)$
$C_1(Eo,Mo) = -2.875 + 0.035\log(Eo) - 0.497\log(Mo)$
$C_2(Eo,Mo) = 13.906 + 2.455\log(Eo) + 2.600\log(Mo)$
$C_3(Eo,Mo) = -25.577 - 13.930\log(Eo) - 5.605\log(Mo)$
$C_4(Eo,Mo) = 9.016 + 17.048\log(Eo) + 3.981\log(Mo)$

Table 2.3: Values of regression coefficients $C_n(Eo,Mo)$ of the inlet study, obtained by fitting a set of numerical results. A base of exponential functions was used to perform this fitting.

Fig. 2.10 shows the results of measuring the variation of the absolute error of the terminal velocity with the distance from the inlet to the bubble, for the different flow

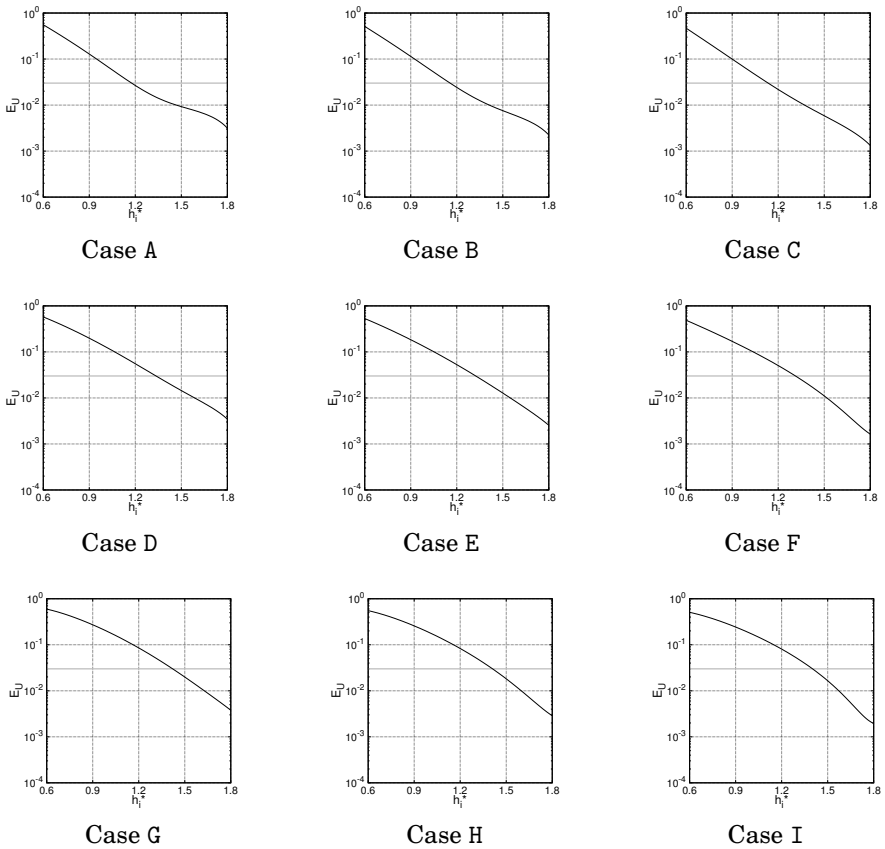

Figure 2.10: Variation of the absolute error in the rising velocity when varying the distance from the bubble to the inlet. The graphs have been obtained by using the Eq. 2.42 with the flow conditions described in Tab. 2.2. A threshold of $3 \cdot 10^{-2}$ has been marked on those graphs.

conditions presented in Tab. 2.2. Those results were fitted as explained above, and used to obtain Eq. 2.42.

In order to check the applicability of Eq. 2.42, several well-known flow regimes are selected for a validation case. In particular, the different flow conditions described in [35] are chosen. In that reference, the authors selected 8 representative flow regimes from the Clift diagram (Fig. 2.9). Tab. 2.4 summarizes those conditions.

Results from the validation cases are presented in Fig. 2.11. That figure shows the variation of the absolute error of the terminal velocity when varying the distance from

Case label	Eo	Mo
Spherical	1.0	$1.26 \cdot 10^{-3}$
Ellipsoidal	10.0	$9.71 \cdot 10^{-4}$
Skirted	0.971	97.1
Intermediate spherical cap + wobbling	9.71	$9.71 \cdot 10^{-12}$
Wobbling	1.94	10^{-12}
Dimpled ellipsoidal cap	97.1	10^{3}
Intermediate skirted + ellipsoidal	38.8	$9.71 \cdot 10^{-4}$
Intermediate ellipsoidal + wobbling	10.0	$9.71 \cdot 10^{-8}$

Table 2.4: Flow conditions for the validation cases shown in Fig. 2.11. Those conditions are set by some representative cases of the Clift diagram (Fig. 2.9) given by [35].

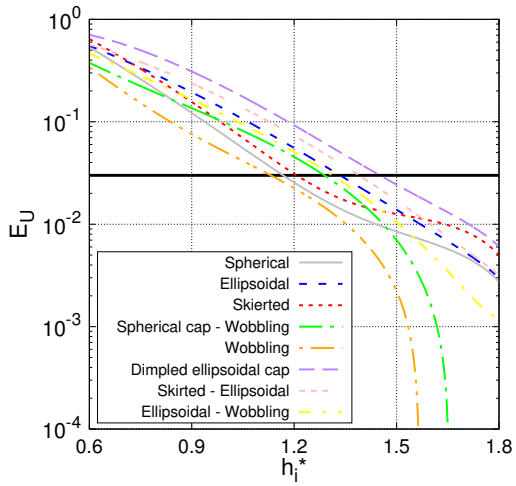

Figure 2.11: Absolute error variation of the rising velocity when varying the distance from the inflow to the bubble, obtained by using Eq. 2.42. The flow conditions have been set by taking some representative cases of the Clift diagram (Fig. 2.9) given by [35]. An indicative threshold of $3 \cdot 10^{-2}$ has been marked on the graph.

the bubble to the inlet, based on Eq. 2.42. Results are coherent with the physical observations. For cases with a high Reynolds number (i.e. "wobbling" situations), the bubble faces the approaching fluid faster, thus the disturbances are propagated only a small upstream distance. On the contrary, slow cases require longer upstream distances.

2.5.3 Outlet placement

By varying the distance between the outlet and the bubble it is shown that the behaviour of the results differs from that seen in the inlet study. In the outlet case, when the distance to the outflow h_o is reduced, the error in the terminal velocity does not significantly increase until a critical distance h_o^*. Beyond this threshold value, the simulation becomes unstable and diverges. The calculation of this h_o^* is not straightforward, since it strongly depends on the numerical parameters of the problem, the simulation time, the flow regime, etc. For tested cases, we successfully used the following expression:

$$h_o = \begin{cases} 1.3 C_{\mathrm{h_o}} d & \text{if } Re_T < 10 \\ 1.3 C_{\mathrm{h_o}} d \log(Re_T) & \text{if } Re_T > 10 \end{cases} \tag{2.44}$$

where $C_{\mathrm{h_o}}$ is a safety constant ($C_{\mathrm{h_o}} \approx 1.4$) and Re_T is the expected terminal Reynolds number. This last parameter can easily be obtained by using the graphs provided by Clift [33] (for standard rising bubbles) and White and Beardmore [34] (for Taylor bubbles), which relate the terminal velocity, the Eötvös number and the Morton number. Fig. 2.9 shows these graphs.

2.6 Numerical experiments

The current section presents a set of numerical experiments upon which the explained domain optimization methods have been tested. We have simulated a standard rising bubble, both in a two- and three-dimensional domain. These cases have been used to validate the DOMs explained above.

2.6.1 Two dimensional rising bubble

The ascent of a two-dimensional bubble is a well-known benchmark test case in multiphase flow field. It consists of a buoyant bubble immersed in a heavier fluid. The problem was originally proposed by [15], but several authors have already reported their results (see for instance [19], [31]).

Fig. 2.12 depicts the computational set-up and domain arrangement of the problem. As it shows, the used mesh is orthogonal and structured. The mesh density is set by dividing the bubble diameter into 50 control volumes, since based upon the results reported by [31] this grid refinement is enough to achieve good-accurate results. The horizontal dimension of the domain is $2d$, whereas the value of the vertical dimension depends on the selected Domain Optimization Method (DOM). For methods based on periodic boundaries (i.e. fringe and buffer zone methods), the distance to the inlet and the outlet are both set to $1.5d$, giving rise to a total vertical dimension of $4d$. For DOMs based on open boundaries (i.e. moving mesh and non-inertial reference frame

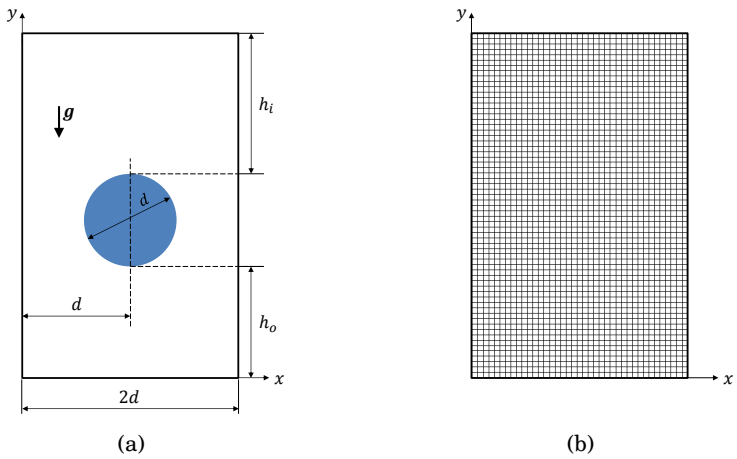

Figure 2.12: Sketch of (a) initial state and (b) mesh configuration of the two dimensional rising bubble problem, in which d denotes the bubble's diameter, and h_i and h_o are the distances from the bubble to the inlet and outlet boundaries, respectively. The mesh is orthogonal and structured, and its density is obtained by dividing the bubble diameter d into 50 control volumes.

methods), the distances to inlet and outlet are optimized by following the explanation given in Sec. 2.5. By doing this, we successfully employed the following distances: $h_i = 1.4d$ and $h_o = 1.7d$. Thus, the total vertical distance is $3.1d$, significantly smaller than the originally proposed in [31].
The flow regime is defined by setting the following dimensionless numbers:

$$\eta_\rho = \frac{\rho_1}{\rho_2} \quad , \quad \eta_\mu = \frac{\mu_1}{\mu_2} \quad , \quad Eo = \frac{gd^2\left(\rho_1 - \rho_2\right)}{\sigma} \quad , \quad Mo = \frac{g\mu_1^4\left(\rho_1 - \rho_2\right)}{\rho_1^2\sigma^3} \tag{2.45}$$

where η_ρ and η_μ are respectively the density and viscosity ratios, Eo is the Eötvös number and Mo is the Morton number. In the present problem, $\eta_\rho = 10$, $\eta_\mu = 10$, $Eo = 9.0$ and $Mo = 6 \cdot 10^{-4}$.

Benchmark quantities are depicted in Fig. 2.13. App. A details how these quantities are obtained. As shown there, these results are in excellent agreement with the ones published by [15]. The simulation times were similar in all the tested methods, except in the buffer zone one, in which it is significantly larger. This, together with the fact that this method requires a complex setting of parameters (see Sec. 2.2.2) and its results are not totally accurate, makes the buffer zone method not very promising for solve more complex cases. Furthermore, the following parameters were found suitable for fringe zone and buffer zone methods: $\{s, b, \Delta, \lambda_{\max}\}_{\text{fringe}} = \{2.5d, 0.17d, 0.017d, 100\}$,

and $\{s, b, \Delta, \lambda_{\max}\}_{\text{buffer}} = \{0.9d, 2.2d, 0.2d, 320\}$.

Benchmark quantities are depicted in Fig. 2.13. Details about how to obtain these magnitudes are presented in App. A. Results are in excellent agreement with those published by [15]. It is important to note that, in contrast to the standard periodic case in which the terminal velocity slightly increases over time, all tested methods avoid this issue, faithfully reproducing the actual physics of the problem. Finally, Tab. 2.5 summarizes the obtained results.

Method	Re	ζ_{2D}	E_V
Fringe zone	9.6196	0.91819	$1.5951 \cdot 10^{-12}$
Buffer zone	9.6268	0.92237	$8.4924 \cdot 10^{-13}$
Moving mesh	9.6065	0.91960	$2.3515 \cdot 10^{-13}$
Non-inertial reference frame	9.6391	0.91868	$5.1756 \cdot 10^{-13}$

Table 2.5: Summary of achieved results at dimensionless time $t^* = 4$ for the two-dimensional rising bubble problem. Reynolds number Re, circularity ζ_{2D} and global volume error E_V are shown for the different tested methods.

2.6.2 Three dimensional rising bubble

In the present section, the different methods are assessed in a full three-dimensional configuration. The flow regime is now set by choosing $\eta_\rho = 100$, $\eta_\mu = 100$, $Eo = 39.4$ and $Mo = 0.065$ (see Eq. 2.45). Buffer zone method has been excluded from this test case, since based on the results obtained in the previous $2D$ case that method does not seems capable of solving the current $3D$ configuration in a reasonable simulation time.

The initial state and the mesh configuration are sketched in Fig. 2.14. A cylindrical shaped domain is used. We used the semi-empirical expression obtained by Harmathy [14] to calculate the diameter of the tube D (Eq. 2.41). Based on this equation, the diameter of the domain D is set to $8d$, as it leads to accurate enough results.

Boundary conditions at inlet and outlet depend on the selected method (see Sec. 2.4), and free slip boundary condition is applied at lateral walls. The bubble is initially placed on the cylinder axis. The mesh structure is generated by extruding a non-uniform two-dimensional mesh along the cylinder axis. The minimum control volume size $h_{\min}$ is set by dividing the bubble diameter into 30. An exponential growth in radial direction is used, and an orthogonal structured grid is fixed in the immediate area of the axis, with a cell size of $h_{\min}$. The mesh configuration showed in Fig. 2.14b is suitable for this flow regime since the lateral motion of the bubble is practically worthless. For methods where the bubble remains stationary within the domain (namely, moving mesh and non-inertial reference frame methods), a more efficient grid could have been

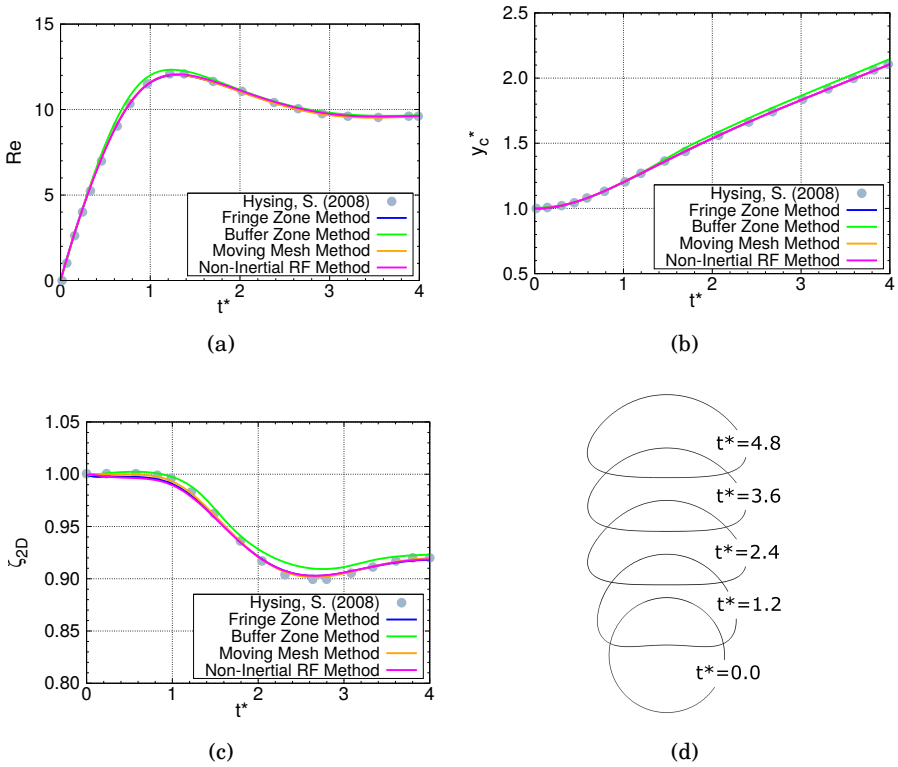

Figure 2.13: Two-dimensional rising bubble results comparison against numerical experiment of [15], for the four tested methods: fringe zone, buffer zone, moving mesh and non-inertial reference frame. The graphs show (a) Reynolds number $Re = \rho_1 U d/\mu_1$, (b) centroid vertical position $y_c^* = y_c/d$, (c) circularity ζ_{2D}, and (d) bubble shape evolution over dimensionless time $t^* = tg^{1/2}d^{-1/2}$.

used, with an axial concentration of cells in the vicinity of the bubble. However, in order to make a fair comparison between methods, the same mesh was used.

For the fringe zone method, we found the following set of suitable parameters: $\{s, b, \Delta, \lambda_{\max}\} = \{2.3d, 0.2d, 0.017d, 100\}$. For details about the used numerical schemes, the reader is referred to [16]. A particular treatment of the non-inertial reference frame method is needed for set-up the domain dimensions. By running some preliminary studies, the distances to the inlet and outlet were fixed to $2.5d$ and $4.0d$ respectively, for the three tested methods. However, the non-inertial reference frame technique needs a bigger distance to the outlet ($h_o = 6.0d$) in order to improve the stability of this

method. Therefore, non-inertial reference frame method need a more careful setting process. Otherwise, it could give rise to numerical instabilities in the most challenging regions of the problem (namely, the bubble's interface and the outflow boundary surroundings).

In order to find a suitable mesh resolution to solve the problem, we selected one of the tested DOMs (i.e. the moving mesh method) and we run several simulations with different mesh resolutions. Tab. 2.6 summarizes this grid independence study, in comparison with the results from other authors [16, 37]. Additionally, Fig. 2.15 shows the time evolution of several variables, for the different tested meshes and with the chosen DOM (i.e. the moving mesh method).

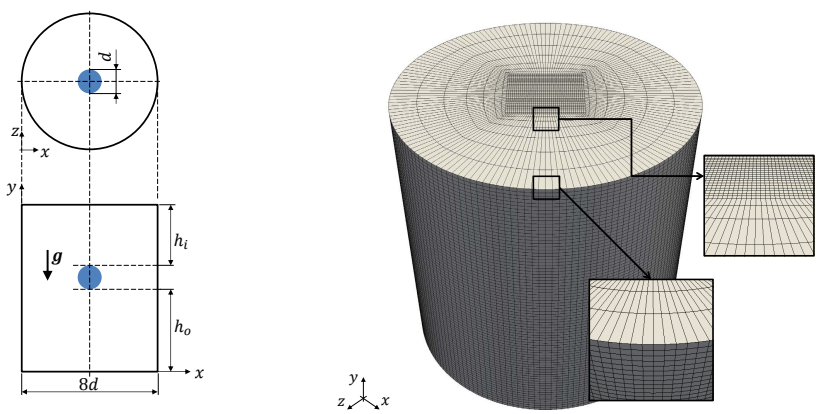

(a) (b)

Figure 2.14: Representation of (a) computational set-up and (b) mesh configuration of the three-dimensional rising bubble problem, in which d denotes the diameter of the bubble, and h_i and h_o are the distances from the bubble to the inlet and outlet boundaries, respectively.

Furthermore, Fig. 2.17 shows the results corresponding to the tested cases with the different DOMs. From the previous mesh independence study, a resolution of $h = d/50$ is known to be capable of accurate reproduce the physics of the problem. Good agreement was found with results reported by Balcázar et al. [16]. Additionally, Fig. 2.16 depicts the profiles' evolution by using the tested methods, without appreciable differences between them. Finally, Tab. 2.7 summarizes the obtained results.

Results	$U_T(dg)^{-1/2}$	ζ_{3D}
CLS - Moving mesh method ($h = d/20$)	0.595	0.7923
CLS - Moving mesh method ($h = d/25$)	0.604	0.7848
CLS - Moving mesh method ($h = d/30$)	0.607	0.7803
Balcázar [16] (fixed mesh)	0.610	0.784
Hnat and Buckmaster [37] (experimental)	0.622	—

Table 2.6: Summary of achieved results at dimensionless time $t^* = 10$ for the three-dimensional rising bubble problem. Dimensionless terminal velocity $U_T(dg)^{-1/2}$ and sphericity ζ_{3D} are shown for moving mesh method, in comparison with reference data reported by [16] ($\eta_\rho = 100, \eta_\mu = 6.67 \cdot 10^3$), and by [37] ($\eta_\rho = 714, \eta_\mu = 6.67 \cdot 10^3$).

Method	Re	ζ_{3D}	E_V
Fringe zone	19.203	0.7811	$2.440 \cdot 10^{-12}$
Moving mesh	19.098	0.7803	$3.569 \cdot 10^{-11}$
Non-inertial reference frame	19.031	0.7797	$7.021 \cdot 10^{-8}$
Balcázar et al. [16]	19.00	0.784	—

Table 2.7: Summary of achieved results at dimensionless time $t^* = 10$ for the three-dimensional rising bubble problem. Reynolds number Re, sphericity ζ_{3D} and global volume error E_V are shown for the different tested methods.

2.7 Conclusions

In the present section, several DOMs have been formulated and implemented. By using those methods, small computational domains can be used, thus saving resources. First, two methods based on periodic boundaries have been introduced: the fringe zone and the buffer zone methods. The first methods are based on a moving region that reinitializes the velocity field. This fringe is moved at each iteration so that it remains at a constant from the bubble centroid. By reinitializing the velocity field in this region, the bubble is prevented from encountering its own wake. Otherwise, due to the use of periodic boundaries, the bubble could interact with its own perturbations. Similarly, the buffer zone method aims to dampen the disturbances by introducing a diffusive moving region.

Another two DOMs have been presented in this chapter, both based on open boundaries. On the one hand, a moving mesh method has been posed. In this method, the mesh follows the ascent of the bubble, assuring a small computational domain. Inflow and outflow conditions are needed on the domain limits. On the other hand, a non-inertial reference frame method has been enforced. In this method the dynamics of the bubble are analyzed from an observer on the bubble. An extra source term is needed

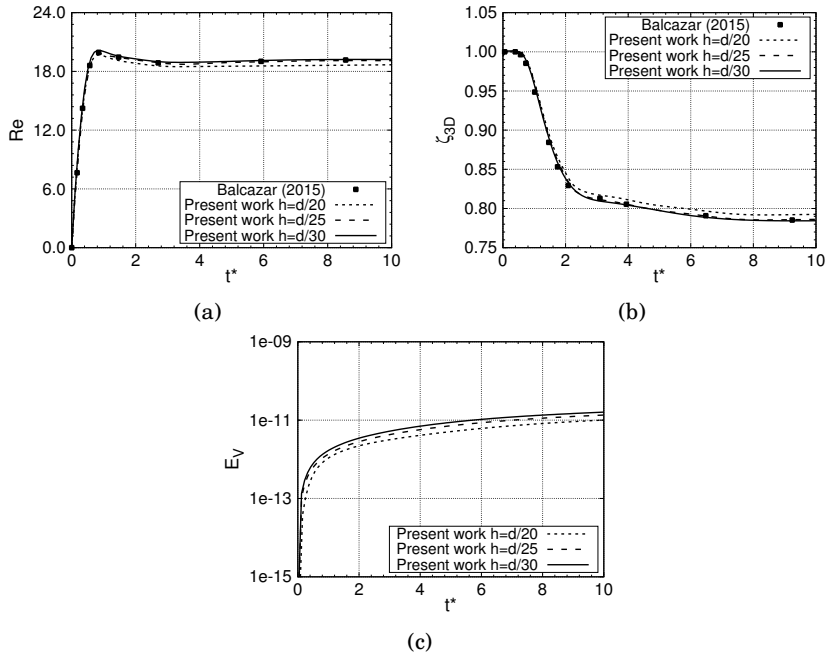

Figure 2.15: Mesh independence study for the three-dimensional standard rising bubble problem, by using the moving mesh method as DOM. The graphs show (a) Reynolds number $Re = \rho_1 U d/\mu_1$, (b) bubble shape evolution, (c) sphericity ζ_{3D} and (d) global volume error E_V over dimensionless time $t^* = tg^{1/2}d^{-1/2}$, for the different mesh resolutions tested.

in order to take the inertial forces into account.

Once the aforementioned methods have been formulated, Sec. 2.3 presents the numerical treatment of the governing equations. Some of the DOMs need a particular treatment of the boundary conditions. In particular, a careful formulation is needed when dealing with inflow and outflow boundary conditions, as explained in Sec. 2.4. Finally, complete study on the sizing of the computational domain has been carried out in Sec. 2.5, aiming to minimize the mesh size while maintaining sufficiently precise results.

The proposed numerical procedures have been validated by running two numerical tests. First, a two-dimensional rising bubble configuration has been studied (Sec. 2.6.1). Obtained results have been compared against those present in the literature. Second, the three-dimensional problem of a bubble rising in an unbounded medium has been conducted (Sec. 2.6.2). Good agreement was found in both test cases.

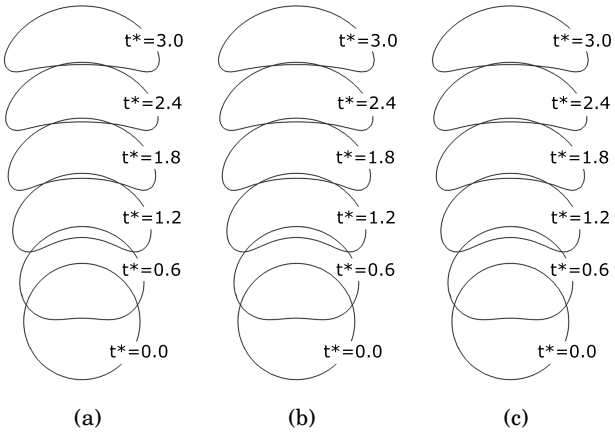

Figure 2.16: Bubble shape evolution by using (a) fringe zone (b) moving mesh and (c) non-inertial reference frame methods.

Once the three proposed methods have been validated, it is reasonable to compare the behavior of each method, in order to find out the one with the best performance.

The fringe zone method features an easy implementation, both in the mathematical model and in the treatment of the boundary conditions. The simulations carried out by using this method do not show a noticeable increase in the simulation time, compared with the standard periodic case. Moreover, we found it stable for the selected problems. However, this method does not seem very promising in terms of applicability, due to the following issues. As it was already mentioned, this method does not allow the presence of an hypothetical second bubble within the domain, since the fringe zone would disrupt its motion. In addition, the mesh could be more efficient using the other methods that maintain the bubble in a static position. Finally, the fact that chiefly restricts the applicability of this method is that it requires a difficult process of parameter setting. The defining parameters of the fringe zone (namely, s, b, Δ and $\lambda_{\max}$) should be re-adjusted when willing to simulate a new study case, because they vary at different regimes and geometries. Therefore, a careful setting of those parameters is needed, in order to correctly dampen the velocity field and not to perturb the ascent of the bubble.

The buffer zone method has the same disadvantages as the fringe zone method. Moreover, it presents an extra drawback: as shown in Sec. 2.3.1, the maximum allowable time step depends on the inverse of the maximum viscosity, so the simulations using the buffer zone method could be significantly slower than those using other methods.

The non-inertial reference frame method solves the main disadvantages of the

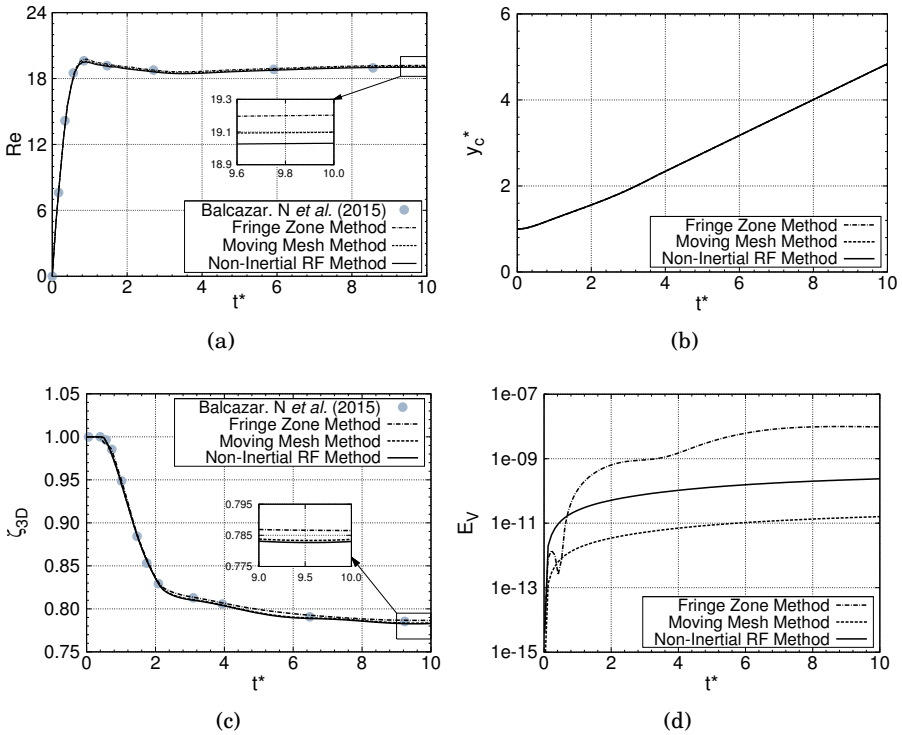

Figure 2.17: Three-dimensional rising bubble results for the three tested methods: fringe zone, moving mesh and non-inertial reference frame. The graphs show (a) Reynolds number $Re = \rho_1 U d/\mu_1$, (b) centroid vertical position $y_c^* = y_c/d$, (c) sphericity ζ_{3D} and (d) global volume error E_V over dimensionless time $t^* = tg^{1/2}d^{-1/2}$.

fringe zone and buffer methods. It allows both the use of improved meshes and the study of bubble interaction problems. Nevertheless, we found numerical stability problems in the tested cases. The method is very sensitive to the setting up of the conservative level set parameters (e.g. numerical schemes) and the domain lengths (e.g. distances from the inlet and outlet). In particular, the following points need a special treatment. First, a non-conservative convective schemes are needed in order to discretize the governing equations (see Sec. 2.3). Second, wider interfaces between fluids are needed in order to assure numerical stability (see Sec. 2.3). Third, the continuity equation (Eq. 1.2) becomes unsatisfied in some high demanding flow regimes. And fourth, larger security factors are needed for the sizing of the computational domain (see Sec. 2.5). An improper treatment of these issues can cause the simulation to di-

verge, which makes this technique not very robust.

We found the moving mesh method the most promising technique from those presented in this work. Despite it involves a computationally expensive process of moving the mesh, it shows a robust behavior in the tested problems. The disadvantages found in the methods based on periodic boundaries are not present in the moving mesh technique. Furthermore, it seems less sensitive to the setting up of the problem compared to the non-inertial reference frame method, which makes the simulations more stable in a broader range of parameters. Based on the aforementioned facts, we chose this method to tackle the challenging problem of the three dimensional Taylor bubble, which is presented in the following chapter.

References

[1] R. Perry, D. Green, J. Maloney, Perry's chemical engineers' handbook, McGraw-Hill, New York, 1997.

[2] D. Gaudlitz, N. Adams, Numerical investigation of rising bubble wake and shape variations, Phys. Fluids. 21 (2009) 1-9.

[3] P. Schlatter, N. Adams, L. Kleiser, A windowing method for periodic inflow/outflow boundary treatment of non-periodic flows, J. Comput. Phys. 206 (2005) 505-535.

[4] J. Nordström, N. Nordin, D. Henningson, The fringe region technique and the Fourier method used in the Direct Numerical Simulation of spatially evolving viscous flows, J. Sci. Comput. 20 (1999) 1365-1393.

[5] O. Estruch, O. Lehmkuhl, R. Borrell, C. D. Pérez Segarra, A. Oliva, A parallel radial basis function interpolation method for unstructured dynamic meshes, Comput. Fluids. 80 (2013) 44-54.

[6] J.T. Batina, Unsteady Euler airfoil solutions using unstructured dynamic meshes, AIAA J. 28 (1990) 1381-1388.

[7] Y. Bazilevs, K. Takizawa, T.E. Tezduyar, Computational Fluid-Structure Interaction, Wiley, Hoboken, 2013.

[8] H. Marschall, S. Boden, C. Lehrenfeld, D. Falconi, J. Carlos, U. Hampel, A. Reusken, M. Wörner, D. Bothe, Validation of Interface Capturing and Tracking Techniques with different Surface Tension Treatments against a Taylor Bubble Benchmark Problem, Comput. Fluids. 102 (2013) 1-21.

[9] H. Rusche, Computational Fluid Dynamics of Dispersed Two-Phase Flows at High Phase Fractions, PhD thesis, 2002.

[10] M.C. Ruzicka, On bubbles rising in line, Int. J. Multiph. Flow. 26 (2000) 1141-1181.

[11] M. Ohta, M. Sussman, The buoyancy-driven motion of a single skirted bubble or drop rising through a viscous liquid, Phys. Fluids. 24 (2012).

[12] M. Ohta, S. Yamaguchi, Y. Yoshida, M. Sussman, The sensitivity of drop motion due to the density and viscosity ratio, Phys. Fluids. 22 (2010) 1-11.

[13] J.L. Guermond, P. Minev, J. Shen, An overview of projection methods for incompressible flows, Comput. Methods Appl. Mech. Eng. 195 (2006) 6011-6045.

[14] T.Z. Harmathy, Velocity of large drops and bubbles in media of infinite or restricted extent, AIChE J. 6 (1960) 281-288.

[15] S. Hysing, S.Turek, D. Kuzmin, N. Parolini, E. Burman, S. Ganesan, L. Tobiska, Quantitative benchmark computations of two-dimensional bubble dynamics, Int. J. Numer. Meth. Fluids. 60 (2008) 601-629.

[16] N. Balcázar, O. Lehmkuhl, L. Jofre, A. Oliva, Level-set simulations of buoyancy-driven motion of single and multiple bubbles, Int. J. Heat Fluid Flow. 56 (2015) 91-107.

[17] R. Mittal, G. Iaccarino, Immersed Boundary Methods. Annual Review of Fluid Mechanics, 37:1 (2005) 239-261.

[18] G.K. Batchelor, An Introduction to Fluid Dynamics, Cambridge University Press, Cambridge, 1967.

[19] N. Balcázar, L. Jofre, O. Lehmkuhl, J. Castro, J. Rigola, A finite-volume/level-set method for simulating two-phase flows on unstructured grids, Int. J. Multiph. Flow. 64 (2014) 55-72.

[20] S. Gottlieb and C. Shu, Total variation diminishing Runge-Kutta schemes, Math. Comp. (1998), 67, 73-85.

[21] N. Balcázar, O. Lehmkuhl, L. Jofre, J. Rigola and A. Oliva, A coupled volume-of-fluid/level-set method for simulation of two-phase flows on unstructured meshes Computers and Fluids (2016), 124, 12-19.

[22] A.J. Chorin. Numerical solution of the Navier-Stokes equations, Math. Comp. 22 (1968), 745-762.

[23] N. Balcázar, J. Rigola, J. Castro, A. Oliva, A level-set model for thermocapillary motion of deformable fluid particles, Int. J. Heat Fluid Flow. October 2016.

[24] L. Jofre, O. Lehmkuhl, J. Ventosa, F.X. Trias and A. Oliva, Conservation Properties of Unstructured Finite-Volume Mesh Schemes for the Navier-Stokes Equations, Numerical Heat Transfer, Part B: Fundamentals 65:1 (2013) 53-79.

[25] A. Sohankar, C. Norberg, L. Davidson, Low-Reynolds-number flow around a square cylinder at incidence: Study of blockage, onset of vortex shedding and outlet boundary condition, Int. J. Numer. Meth. Fluids. 26 (1996) 39-56.

[26] J.H. Ferziger, M. Peric, Computational Methods for Fluid Dynamics, Springer, Berlin, 2002.

[27] R.W. Davis, E.F. Moore, A numerical study of vortex shedding from rectangles, J. Fluid Mech. 116 (1982) 475-506.

[28] B. Christer, V. Johansson, Boundary Conditions for Open Boundaries for the Incompressible Navier-Stoke Equation, J. Comput. Phys. 105 (1993) 233-251.

[29] S. Shirayama, Flow past a sphere - Topological transitions of the vorticity field, AIAA J. 30 (1992) 349-358.

[30] J. Magnaudet, M. Rivero, J. Fabre, Accelerated flows past a rigid sphere or a spherical bubble. Part 1. Steady straining flow, J. Fluid Mech. 284 (1995) 97-135.

[31] S. Hysing, Mixed element FEM level set method for numerical simulation of immiscible fluids, J. Comput. Phys. 231 (2012) 2449-2465.

[32] N.R. Draper and H. Smith, Applied Regression Analysis, Ed. Wiley, New York, 1998.

[33] R. Clift, Bubbles, Drops and Particles, volume 94. Academic Press, Inc., New York, 1979.

[34] E.T. White, R.H. Beardmore, The velocity of rise of single cylindrical air bubbles through liquids contained in vertical tubes, Chem. Eng. Sci. 17 (1962) 351-361.

[35] N.G. Deen, M. Annaland, J. Kuipers, Direct numerical simulation of complex multi-fluid flows using a combined front tracking and immersed boundary method, Chem. Eng. Sci. 64 (2009) 2186-2201.

[36] J.U. Brackbill, D.B. Kothe, C. Zemach, A continuum method for modeling surface tension, J. Comput. Phys. 100 (1992) 335-354.

[37] J.G. Hnat and J.D. Buckmaster, Spherical cap bubbles and skirt formation, Phys. Fluids. 19 (1976), 182-194.

3

The Taylor Bubble problem

Main contents of this chapter have been published in:

E. Gutiérrez, N. Balcázar, E. Bartrons and J. Rigola. Numerical study of Taylor bubbles rising in a stagnant liquid using a level-set/moving-mesh method. *Chemical Engineering Science*, 164:158–177, 2017.

Abstract. An Arbitrary Lagrangian-Eulerian formulation has been posed to solve the challenging problem of the three-dimensional Taylor bubble, within a Conservative Level Set (CLS) framework. By employing a domain optimization method (i.e. the moving mesh method), smaller domains can be used to simulate rising bubbles, thus saving computational resources. The coupled CLS - Moving Mesh method has been verified by means of extensive numerical tests. The challenging problem of the full three-dimensional Taylor bubble has then been thoroughly addressed, providing a detailed description of its features. The study also includes sensitivity analyses with respect to the initial shape of the bubble, the initial volume of the bubble, the flow regime and the inclination of the channel.

3.1 Introduction

The slug flow is of fundamental importance in a vast variety of engineering applications and natural phenomena. This flow pattern consists of bullet-shaped bubbles separated by liquid slugs. The bubbles almost completely fill the channel cross section, where at most a thin liquid film separates them from the wall. In reference to its applications, the growing interest in miniaturization of chemical unit operations makes slug flow an important area of study [1]. In addition, due to the fact that biomedical studies are becoming increasingly important for the scientific community, slug flows seems to be the key to understand complex blood flow cases, e.g. embolisms. Other relevant scientific fields are also directly related to this flow pattern: volcanology [2], geothermal power plants, gas and oil extraction, cryogenic fluids, etc.

To understand these flows the elemental problem of a single Taylor bubble should be thoroughly comprehended, laying a solid foundation for the analysis of more complex cases. Buoyant bubble problems need the use of large domains to achieve proper capture of the phenomena. That is due to the need of leaving enough vertical space for the bubble to reach its steady state. This problem can be handled by using an Arbitrary Lagrangian-Eulerian (ALE) formulation. In this case, since the mesh is moving along the bubble rise, a short computational domain is enough. Dynamic mesh methods have been broadly used in CFD [3–5].

In order to deal with the multiphase domain, several methods are available in the literature. In the present chapter, a Conservative Level Set method (CLS) is used [6]. As stated in previous chapters, this technique has been implemented in the framework of finite-volume discretization and unstructured meshes. The method greatly reduces the problem of mass conservation of the Standard Level Set (SLS) methods, and it was thoroughly verified in [7, 8]. The coupling between the conservative level set method and the moving mesh technique has been already verified and validated in the previous chapter (see Sec. 2.6.1 and 2.6.2).

In the present chapter, the challenging problem of the full three-dimensional Taylor bubble is addressed. Since the publications of the original works of Davies and Taylor [9] and White and Beardmore [10], several approaches have been assessed to simulate Taylor bubbles. Rigorous experimental research have been reported [11–14], theoretical models have been proved [15, 16] and numerical methods have been addressed, by using Volume of Fluid method [17], Front Tracking method [18], Lattice Bolzmann method [19, 20], and others [21, 22]. To the authors' knowledge, the present work is the first approach to the Taylor bubble problem by means of a conservative level set method. Regarding the aforementioned numerical studies, the proposed method solve three typical problems encountered when the Taylor bubble problem is addressed. First, as three-dimensional unstructured meshes are employed, 3D circular cross-section tubes can be directly studied, with no need of using a simplified approach (i.e. assuming axisymmetric). Second, by using the CLS method, the mass conservation

problem which is known to affect to standard level set formulations is circumvented. Finally, by using a domain optimization method, the covered domain is small compared with other methods, thus saving computational resources. Therefore, a simulation for some specific conditions has been carried out, allowing comparison against experimental data [13] and other numerical studies [22]. Furthermore, in order to check the validity of the method in a wide variety conditions, other studies have been considered, e.g. sensitivity to the shape of the initial bubble, sensitivity to variations in the initial volume of the bubble, sensitivity to flow regime (comparing the results against those of Quan [18] and Hayashi et al. [23]), and sensitivity to the channel inclination. Regarding this last topic, there are several valuable studies present in the literature that aim to solve the Taylor bubble problem in inclined channels. For instance, Amaya-Bower and Lee [20] numerically solved the problem in a square cross-section channel, and Shosho and Ryan [14] studied several mixtures at different inclinations.

The work is organized as follows: Sec. 3.2 presents a short summary about the `CLS+MM` method, aiming to gather the different parts of the algorithm presented in a scattered manner throghout the previous chapters. This section collects the governing equations of the method, the surface tension treatment, the moving mesh technique and the numerical formulation used to discretize the governing equations. Thereafter, the problem of the three-dimensional Taylor bubble is thoroughly addressed in Sec. 3.3, providing particular studies and a complete description of its features. This study includes sensitivity analyses with respect to the initial shape of the bubble, the initial volume of the bubble, the flow regime and the inclination of the channel. Finally, Sec. 3.4 presents the concluding remarks.

3.2 Mathematical formulation

The present section aims to gather the mathematical approach to solve multiphase problems by using a conservative level set + moving mesh (`CLS+MM`) method. Assuming incompressible flow, Newtonian fluids, no mass transfer at the interface between fluids, constant surface tension coefficient σ and the use of a moving mesh, the Navier-Stokes equations governing the fluid motion are written as [3, 6]:

$$\frac{\partial}{\partial t}\left(\rho\mathbf{v}\right) + \nabla\cdot\left(\rho\mathbf{v}(\mathbf{v}-\mathbf{v}_{\text{domain}})\right) = -\nabla p + \nabla\cdot\mu\left(\nabla\mathbf{v} + (\nabla\mathbf{v})^T\right) + \rho\mathbf{g} + \sigma\kappa\mathbf{n}\delta_\Gamma \tag{3.1}$$

$$\nabla\cdot\mathbf{v} = 0 \tag{3.2}$$

where t is the time, ρ and μ are respectively the fluid density and viscosity, $\mathbf{v}$ is the velocity field, p is the pressure field, $\mathbf{g}$ is the gravity acceleration, $\mathbf{n}$ is the unit normal vector to the interface, κ is the interface curvature, and δ_Γ is the Dirac delta function located at the interface Γ. $\mathbf{v}_{\text{domain}}$ is the mesh velocity, which for this case is equal to the vertical component of the bubble velocity (see App. A). Finally, ρ and μ can be

obtained by the following expressions:

$$\rho = \rho_1 H_1 + \rho_2 (1 - H_1) \tag{3.3}$$

$$\mu = \mu_1 H_1 + \mu_2 (1 - H_1) \tag{3.4}$$

where subscripts 1 and 2 refer to continuous fluid and bubble fluid respectively, and H_1 is the Heaviside function, which takes the value of 1 in Ω_1 and 0 in Ω_2. These Ω_1 and Ω_2 are the corresponding subdomains associated with the two fluids. At discretized level, physical properties are smoothed according to the CLS method [6, 25], in order to avoid numerical instabilities of the interface.

3.2.1 Interface capturing

The two main difficulties of simulating fluid interfaces are to keep up a sharp interface and to accurately calculate the surface tension [24]. In order to deal with this issues, we use the CLS method for interface capturing [6]. In this method, the regularized indicator function ϕ is used in order to implicitly represent the interface:

$$\phi(\mathbf{x}, t) = \frac{1}{2}\left(\tanh\left(\frac{d(\mathbf{x}, t)}{2\varepsilon}\right) + 1\right) \tag{3.5}$$

Here, $d(\mathbf{x}, t) = \min_{x_\Gamma(t) \in \Gamma}(|\mathbf{x}, \mathbf{x}_\Gamma(t)|)$ is the signed distance function and ε is a parameter for controlling the thickness of the interface. This level set function takes the value 0 in one fluid, and 1 in the other. It varies continuously along the interface, which can be located by getting the $\phi = 0.5$ isosurface. Based upon this level set function, the fluid properties are regularized as follows:

$$\rho = \rho_1 \phi + \rho_2 (1 - \phi) \tag{3.6}$$

$$\mu = \mu_1 \phi + \mu_2 (1 - \phi) \tag{3.7}$$

The level set function is advected by the velocity field obtained from the solution of the Navier-Stokes equations (Eq. 3.1 and 3.2); this yields:

$$\frac{\partial \phi}{\partial t} + \nabla \cdot \phi \mathbf{v} = 0 \tag{3.8}$$

Due to numerical diffusion, the thickness of the interface tends to widen. In order to deal with this problem, a reinitialization equation is used to compress the interface [26]:

$$\frac{\partial \phi}{\partial \tau} + \nabla \cdot \phi (1 - \phi) \mathbf{n}_{\tau=0} = \nabla \cdot \varepsilon \nabla \phi \tag{3.9}$$

where τ is the pseudo-time. This equation consists of a compressive term $\phi(1-\phi)\mathbf{n}_{\tau=0}$ which compresses the level set function along the unit normal vector $\mathbf{n}$, and of a diffusion term $\nabla \cdot \varepsilon \nabla \phi$, that maintains the characteristic thickness of the profile proportional to $\varepsilon = 0.5 h^{0.9}$, where h is the grid size [6].

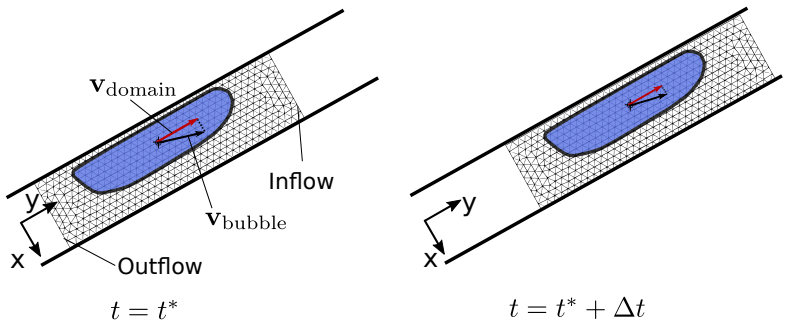

Figure 3.1: Sketch of the moving mesh method in Taylor bubble problems.

3.2.2 Surface tension treatment

By using the Continuum Surface Force (CSF) method developed by Brackbill et al. [27] two challenging issues can be handled: the computation of the curvature κ and the application of the resulting pressure jump to the fluids. Following [27], the singular term $\sigma\kappa\mathbf{n}\delta_\Gamma$ is rewritten as a volume force:

$$\sigma\kappa\mathbf{n}\delta_\Gamma = \sigma\kappa\left(\phi\right)\nabla\phi \tag{3.10}$$

where $\mathbf{n}$ and $\kappa\left(\phi\right)$ are given by:

$$\mathbf{n} = \frac{\nabla\phi}{\left\|\nabla\phi\right\|} \tag{3.11}$$

$$\kappa\left(\phi\right) = -\nabla\cdot\mathbf{n} \tag{3.12}$$

Here, $\nabla\phi$ is evaluated by means of the least-squares method [6].

3.2.3 Moving mesh

By using the current dynamic mesh approach, the computational domain is moved at the vertical velocity of the bubble (see App. A). Thus, the bubble apparently stays vertically stationary inside the mesh domain. Fig. 3.1 shows how the moving mesh method works in Taylor bubble problems.

When an Arbitrary Lagrangian-Eulerian approach is adopted [4], the computational volume should be preserved. This is done by using the so-called Space Conservation Law (SCL) [3]. The mass conservation is procured by enforcing this SCL, which results in the modification of the mass flux through faces, adding the corresponding volume swept in the movement of the face under consideration. As the mesh is trivially

moved without deformation at a velocity $\mathbf{v}_{\text{domain}}$ equal to the bubble's vertical velocity, the calculation of the this correction is straightforward.

3.2.4 Numerical schemes

The aforementioned equations have been discretized on a collocated unstructured grid arrangement by means of the finite-volume method, according to [6]. A Central Difference (CD) scheme is used to discretize the diffusion terms of the governing equations (Eqs. 3.1 and 3.9). A Superbee flux limiter adapted to unstructured meshes [6] is used to discretize the convective term of the advection equation Eq. 3.8, and a CD scheme is used for the convective term of the momentum equation, Eq. 3.1. For time discretization, a 3-step-third-order accurate TDV Runge-Kutta scheme [28] is used for advection and reinitialization equations (Eqs. 3.8 and 3.9). Finally, CD schemes are used for the compressive and diffusive terms of the reinitialization equation, Eq. 1.9 [6].

The pressure-velocity coupling is solved by means of a Fractional Step method [6, 29–31]. Momentum equation (Eq. 3.1) is computed in two steps:

$$\frac{\rho\mathbf{v}^* - \rho^n\mathbf{v}^n}{\Delta t} = \nabla\cdot\left[\rho\mathbf{v}^n\left(\mathbf{v}^n - \mathbf{v}^n_{\text{domain}}\right)\right] + \nabla\cdot\mu\left(\nabla\mathbf{v}^n + \nabla^T\mathbf{v}^n\right) + \rho\mathbf{g} + \sigma\kappa\nabla\phi \tag{3.13}$$

For simplicity, this equation is discretized using an explicit Euler scheme, however and explicit Adams-Bashforth scheme has been used for computations. The next step of the method is the calculation of the following expression:

$$\mathbf{v}^{n+1} = \mathbf{v}^* - \frac{\Delta t}{\rho}\nabla p^{n+1} \tag{3.14}$$

Now, by adding the continuity equation (Eq. 3.2), the following Poisson equation is obtained to solve the pressure:

$$\nabla\cdot\left(\frac{1}{\rho}\nabla p^{n+1}\right) = \frac{1}{\Delta t}\nabla\cdot\mathbf{v}^* \tag{3.15}$$

The discretization of this equation leads to a linear system, which is solved by means of a preconditioned conjugate gradient method. Cell-face velocity is calculated according to [6,31], in order to avoid pressure-velocity decoupling and to fulfill the incompressible constraint. This cell-face velocity is used to advect the CLS function in Eq. 3.8 and momentum in Eq. 3.1.

Boundary condition

As the mesh is vertically moved, open boundaries are needed at the upper and lower domain limits. Therefore, an inflow condition is enforced at the upper limit, whilst

an otflow boundary condition is applied at the lower limit. The reader is referred to Sec. 2.4 for details on the formulation of these boundaries. Correspondingly, all conditions are imposed at the lateral boundaries.

Time step

A CFL type condition is used to dynamically determine an admissible time step for stable computations. By a straightforward comparison among the terms of Eq. 3.1, the following global stability condition for the proposed CLS-MM method is obtained:

$$\Delta t = \mathscr{C}_{\mathrm{CFL}} \cdot \min\left(\frac{h}{\|\mathbf{v}_n\|}, \frac{h^2 \rho_n}{\mu_n}, \sqrt{\frac{h}{g}}, \left(\frac{\rho_1+\rho_2}{4\pi\sigma}\right)^{1/2} h^{3/2}, \frac{h}{\|\mathbf{v}_{mesh}\|} \right) \tag{3.16}$$

where subscript n denotes that the corresponding variable is evaluated at the node n under consideration, h is the characteristic size of the control volume n calculated as the cubic root of the cell volume, and $\mathscr{C}_{\mathrm{CFL}}$ is a safety constant ($\mathscr{C}_{\mathrm{CFL}} \approx 0.1$).

Calculation algorithm

The calculation process needed to advance from the current time step t^m to the following one t^{m+1} is detailed in Alg. 1. The present method has been implemented in the context of a parallel c++/MPI code called *TermoFluids*. The reader is referred to Balcázar et al. [6] for further details on the finite volume discretization of the governing equations. Simulation times of the cases presented in this chapter are between 12 and 72 hours (depending mostly on the size of the mesh and the obtained CFL condition). Those cases were run using 32 up to 256 CPUs.

3.3 Taylor bubble study

In the present section, the challenging problem of the full three-dimensional Taylor bubble is addressed. First, some general definitions are introduced in Sec. 3.3.1. Second, a well-known flow regime is chosen, in order to have enough reference data. A complete result comparison has been carried out at this point (see Sec. 3.3.2). From this scenario, several studies have been conducted to check the influence of different conditions in the problem (see Sec. 3.3.3 to 3.3.7). To the authors' knowledge, most of these investigations are novel in scientific terms.

3.3.1 General considerations about the problem

The Taylor bubble problems studied below have some common defining parameters that set up the problem configuration and, in particular, its initial condition. Those

Algorithm 1 `CLS-MM` method

repeat:
1: Calculate the mesh velocity, as explained in Sec. 3.2.3.
2: Choose a suitable time step, as explained in Sec. 3.2.4.
3: Advect the level set function ϕ by solving Eq. 3.8.
4: Compress the interfaces between both fluids by solving Eq. 3.9.
5: Update the density, viscosity and curvature fields.
6: Calculate the predictor velocity.
7: Perform the mass conservation step explained in Sec. 2.4.3.
8: Solve the Poisson equation to get the pressure field.
9: Compute the velocity at the faces [6]
10: Calculate the final velocity.
11: Move the mesh.
until $t > t_{\text{end}}$

Fractional step method

parameters are presented in the present section. Fisrt, the size of the bubble is characterized by a dimensionless bubble size parameter $k = 2a/D$, where a is the radius of an equivalent spherical bubble of the same volume, and $D = 2R$ is the diameter of the tube. Then, $a = \left(3V_{\Omega_2}/4\pi\right)^{1/3}$, where V_{Ω_2} is the volume of the bubble. The initial radius of the bubble r is chosen to be close to the one that will have the bubble in the steady state. In order to do so, the following expression is used, as derivation of the one obtained by Brown [32] when $D \sim r$:

$$r = \frac{D}{2} - \sqrt[3]{\frac{3\mu_1^2}{4g\rho_1^2} \cdot Re_T} = \frac{D}{2} - \sqrt[3]{\frac{3\mu_1 D^{3/2}}{4g^{1/2}\rho_1} \cdot Fr_T} \tag{3.17}$$

where the expected terminal Reynolds number $Re_T = \rho_1 U_T D/\mu_1$ or the expected terminal Froude number $Fr_T = U_T/\sqrt{Dg}$ is obtained from the well-known predictions of White and Beardmore [10].

Furthermore, as the used method leaves the bubble quiescent at its starting vertical position, initial distances from the bubble nose to the inlet h_i and from the bubble rear end to the outlet h_o should be fixed, as they will remain approximately constant during the simulation. On the one hand, the distance h_i is set to D, since for not too slow regimes ($Re_T > 1$) velocity field perturbations do not propagate beyond D from the bubble nose. On the other hand, the distance h_o has been determined by used Eq. 2.44 presented in the previous chapter. It is important to note that that equation was successfully used in the context of the method presented in this work. The extrapolation of its applicability to other conditions should be analyzed particularly.

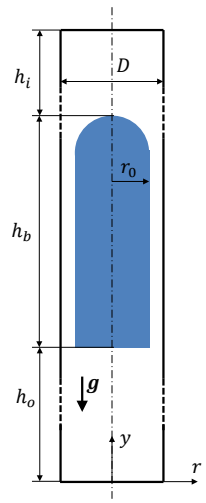

Figure 3.2: Outline of the initial set-up of the Taylor bubble problem. Here, r = 0.007m is the the bubble's radius and h_b = 0.0523m is its length.

3.3.2 Taylor bubble rising in viscous liquid - validation case

In this section, the Taylor bubble problem is studied by using the coupled `CLS-MM` method. The chosen reference case is the one published by Bugg and Saad [13] (experiment) and by Ndinisa et al. [22] (numerical simulation).

Fig. 3.2 depicts the initial configuration for the reference case. The simulation is based on the conditions described by Ndinisa et al. [22]. The density of the continuous phase ρ_1 is set to 911kg/m^3, and its viscosity μ_1 is 0.084Pa$\cdot$s. On the other hand, the properties of the bubble's fluid correspond to air at 20°C. Therefore, ρ_2 = 1.205kg/m^3 and $\mu_2 = 1.827 \cdot 10^{-5}Pa\cdot$s. The surface tension coefficient σ is set to 0.0328N/m. The diameter of the pipe D is set to 0.019m. Those properties and geometrical parameters yield the following dimensionless groups: $\eta_\rho = \rho_1/\rho_2 = 756.017$, $\eta_\mu = \mu_1/\mu_2 = 4597.701$, $Eo = \rho_1 g D^2/\sigma = 100$ and $Mo = g\mu_1^4/\left(\rho_1\sigma^3\right) = 0.015$. For its part, the expected terminal Reynolds number $Re_T = \rho_1 U_T D/\mu_1$ is about 27, where U_T is the terminal velocity calculated as explained in App. A. No-slip boundary condition is used at the lateral side of the domain. The boundary conditions at the inlet and the outlet have been explained in detail in Sec. 2.4.

The initial shape of the bubble is a cylinder with an hemisphere at the front end (see Fig. 3.2). The radius r of this cylinder is 0.007m (see Eq. 3.17). The total axial distance h_b of the initial bubble is 0.0523m, which leads to a total initial volume of $7.697 \cdot 10^{-6}$m^3, and a parameter k of 1.29.

The simulation domain is cylindrical and it was meshed using hexahedral control volumes uniformly distributed over the whole space. The meshes were generated by a constant step extrusion of a two-dimensional unstructured grid along the axis of the cylinder, being the step size $y_{\text{length}}/N_{\text{planes}}$, where y_{length} is the axial length and N_{planes} is the number of planes in which the vertical axis is divided. Tab. 3.1 shows a description of the used grids. Three meshes with different resolution were considered, namely `M1`, `M2` and `M3`. The mesh resolution was set by dividing the tube diameter D into 52, 76 and 95 control volumes, respectively.

Furthermore, as pointed out above, initial distance form the bubble nose to the inlet h_i was set to D, and distance from the bubble rear end to the outlet h_o was computed by means of Eq. 2.44. For the conditions of the experiment of Ndinisa et al. [22], we obtained $h_o \approx 2D$. Taking into the account that the axial dimension of the initial bubble h_b is $2.75D$, a total axial distance y_{length} of $5.75D$ was found enough to reproduce the ascent of the Taylor bubble until it reached the steady state. This greatly reduces the domain requirements compared to previous works, where axial distances between $8D$ and $16D$ are typically used [18]. Moreover, more complex meshes could be used, with a relatively large characteristic cell size, and having enough nodes concentration in the important regions of the problem (i.e. the wall vicinities and the wake zone). However, for the sake of simplicity, current simulations were run with quasi-homogeneous meshes.

Mesh name	Mesh size	Cells per plane	N_{planes}	y_{length}	h
`M1`	$5.3 \cdot 10^5$	2098	254	$5D$	$D/52$
`M2`	$1.9 \cdot 10^6$	5043	380	$5D$	$D/76$
`M3`	$3.7 \cdot 10^6$	7891	475	$5D$	$D/95$

Table 3.1: Description of the meshes used in the Taylor bubble problem, where N_{planes} is the number of planes in which the vertical axis is divided and y_{length} is the length of this vertical axis.

Fig. 3.3a shows the evolution of the Reynolds number Re along dimensionless time t^*. Results are summarized in Tab. 3.2, where a comparison against other works are presented. Good agreement was found when `M2` and `M3` meshes are used. With `M1` mesh, the final velocity is less accurate. Furthermore, Fig. 3.3b depicts the bubble profile evolution along the dimensionless time t^*.

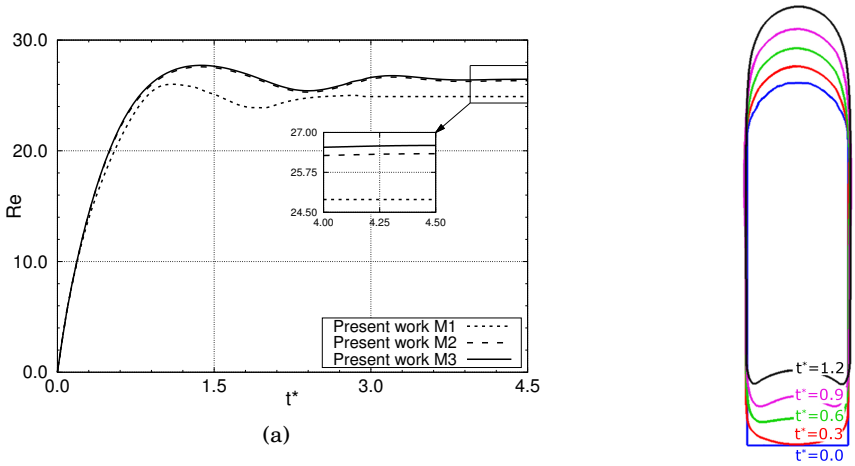

(a) (b)

Figure 3.3: Reynolds number evolution and profiles evolution of the tested Taylor bubble. The bubble profile after $t^* = 1.2$ remains approximately constant.

Case	U_T	E_{U_T}
Present work (M1)	0.1210m/s	7.63%
Present work (M2)	0.1277m/s	2.52%
Present work (M3)	0.1286m/s	1.83%
Ndinisa et al. [22]	0.140m/s	6.87%
White and Beardmore [10]	0.1272m/s	2.90%
Bugg and Saad [13]	0.131m/s	—

Table 3.2: Summary of achieved results at dimensionless time $t^* = 4.5$ for the three-dimensional Taylor bubble problem, where E_{U_T} is the relative error compared to the experimental results of Bugg and Saad [13].

Results discussion

Fig. 3.4 shows several velocity profiles plotted over different sections by comparing them with the reference data. Results are shown for the three studied meshes. On the other hand, Fig. 3.5 sketches the velocity field and the streamlines. By analysing these images, a fairly accurate picture of the velocity field can be depicted.

First, the normalized axial velocity along the tube axis above the bubble nose is plotted in Fig. 3.4a. Results of this graph are referred to an auxiliary reference frame located in the bubble nose. Ahead of the bubble, the suspending fluid is perturbed by the ascent of the bubble. However, as shown in Fig. 3.4a, the bubble does not have a strong influence on the fluid above it, since the axial velocity tends toward zero at a distance of $D/3$. Close to the bubble nose, the fluid is strongly radial, since the bubble is moving upwards and the fluid ahead of it is pushed sideways. This can be clearly seen in Figs. 3.4b and 3.4c, where the normalized axial and radial velocities across the tube radius at $0.111D$ above the bubble nose are plotted, respectively. Figs. 3.4d and 3.4e depict the normalized axial and radial velocities in the developing film at $0.504D$ below the bubble nose, showing that, as we descend into the developing film, a strong radial velocity component is still observed, specially close to the fluids' interface. The developing film speeds up and thins as it falls, until the shear stress at the wall is capable of withstanding the weight of the film. The fully developed film is then formed, giving rise to an essentially axial and constant flow. When the rear end is achieved, the axial velocity is dramatically reduced (see Fig. 3.4f, showing the normalized axial velocity in the wake of the bubble at $0.2D$ below the bubble). At this point the flow becomes strongly radial, since the fluid from the wall is transferred toward the cylinder axis. The radial velocity component swiftly decays to zero near the tube axis, where the suspending fluid is moving upward with a similar velocity as the bubble's one.

The present results are confirmed by experimental and numerical studies reported by Bugg and Saad [13] and Ndinisa et al. [22]. For meshes `M2` and `M3`, good agreement can be found in all of the results. On the other hand, mesh `M1` does not seem fine enough to correctly replicate these results. For the results obtained with `M2` and `M3` meshes, the slight disagreements can be explained based on the ambiguity of locating a specific section relative to the bubble nose. In effect, results in Fig. 3.4 show notable changes when visualizing sections near each other, highlighting the importance of using fine meshes. This observation is consistent with Ndinisa et al. work [22].

The sketches of the velocity field and the streamlines (Fig. 3.5) agree qualitatively with results reported by Bugg and Saad [13] and by Ndinisa et al. [22]. These images underscore the essentially axisymmetric nature of this problem. Furthermore, a large vortex is observed inside the Taylor bubble. Due to the selected flow regime, no vortex appears in the closed-wake of the bubble.

3.3.3 Effect of the initial shape of the Taylor bubble

Besides the initial shape proposed above, others were also tested in order to check the influence of the initial condition on the obtained results, with the same dimensionless numbers than in the previous section. The different initial bubble forms tested are: a cylinder with an hemisphere at the front end, a cylinder with two hemispheres, a standard cylinder, a cylinder with an hemisphere at the front end and a notched rear

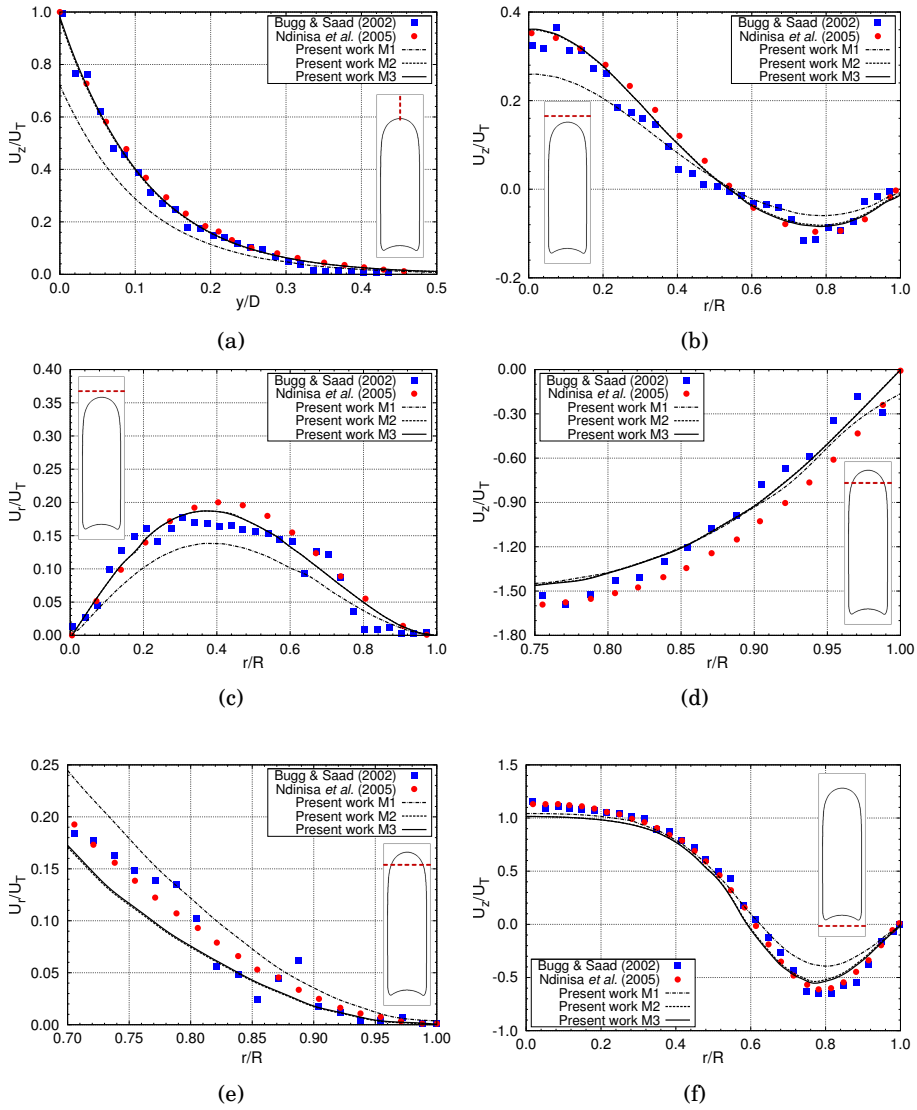

Figure 3.4: Results of the three-dimensional Taylor bubble problem, showing (a) the normalized axial velocity in the tube axis above the bubble nose, (b) the normalized axial velocity in a section above the bubble, (c) the normalized radial velocity in a section above the bubble, (d) the normalized axial velocity in the developing film, (e) the normalized radial velocity in the developing film and (f) the normalized axial velocity in the wake of the bubble.

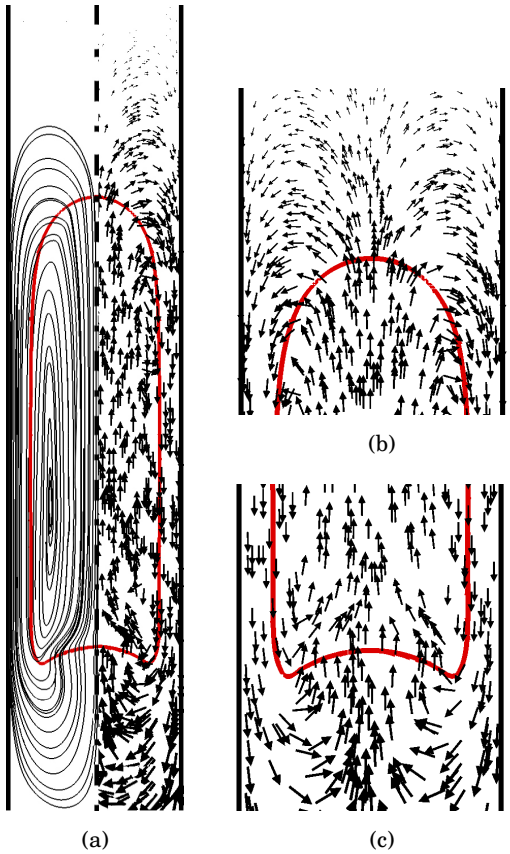

Figure 3.5: Streamlines and velocity field details of the three-dimensional Taylor bubble problem.

end, and a shape close to the stationary. This last form was obtained by taking the bubble profile from a previous simulation. Fig. 3.6 depicts these different initial bubble shapes. All of them have the same total volume of $7.697 \cdot 10^{-6}\mathrm{m}^3$ ($k = 1.29$), and the same radius r. The radius of the notch in the respective case is $0.8r$. Fig. 3.7 shows the time evolution of these distinct cases. The initial bubble shape only has influence in the transient period and in the total time needed to achieve the final state. In this regard, the shape close to the stationary is narrowly the first to achieve the stationary state, at approximately $t^* = 3.0$. The governing factor in the time evolution of the different shapes seems to be the shape of the bubble's frontal area (at least for the selected

parameter k). While all the shapes with an hemisphere in the front part of the bubble evolve similarly, the standard cylinder presents a very different time evolution, as well as the shape close to the stationary state.

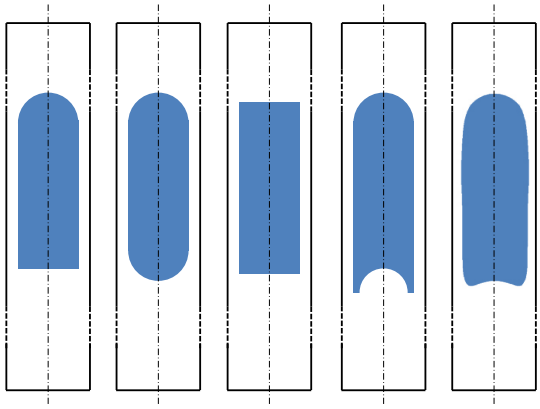

Figure 3.6: Sketch of the different initial states tested to solve the Taylor bubble problem.

3.3.4 Effect of the volume of the Taylor bubble

As stated above, the initial volume of the bubble is $7.697 \cdot 10^{-6}\mathrm{m}^3$, corresponding to a parameter k equal to 1.29. A comparative study varying this parameter has been carried out, in order to investigate the influence of the volume of the bubble in the results.

A set of 11 cases has been run, corresponding to the following k numbers: 0.4, 0.5, 0.6, 0.7, 0.8, 0.9, 1.0, 1.1, 1.2, 1.3 and 1.4. The initial shapes of the bubbles have been taken spherical when $k < 2r/D$, and cylindrical with an hemisphere at the front end when $k > 2r/D$. All other physical and geometrical parameters are the same as in previous sections. The type of mesh employed is also equivalent to the ones described above. In order to determine a suitable number of control volumes, a mesh independence study has been carried out for the extreme cases $k = 0.4$ and $k = 1.4$, since the geometry of the problem has changed. Tab. 3.3 summarized the results of this study, proving that by using a mesh with 70 control volumes per diameter, the obtained results are sufficiently precise. The dimensions of the domain are obtained as discussed above.

Outcomes of the current study are presented in subsequent figures. On the one

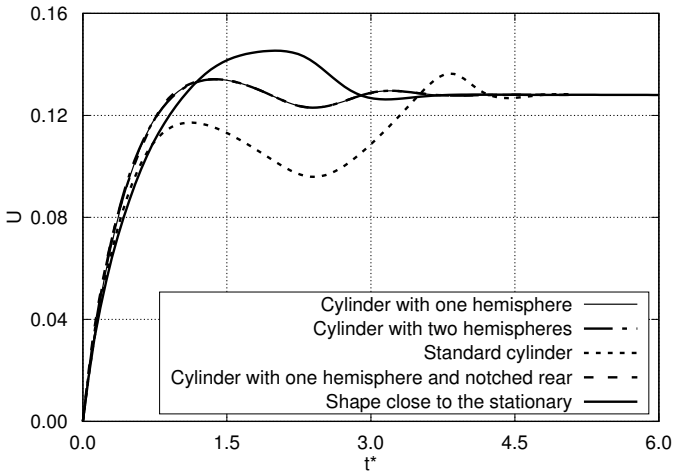

Figure 3.7: Evolution of the velocity of the Taylor bubble over dimensionless time t^*, for the different initial bubble shapes tested.

hand, terminal shapes of the bubbles are shown in Fig. 3.8. These forms present the following features: for $k < 0.5$ the influence of the wall is not a crucial factor in the ascent of the bubble. Thus, it remains elliptical, as it corresponds to this regime for standard rising bubbles. For $k = 0.6$ and $k = 0.7$, the bubble tends to acquire an elongated mushroom shape, showing the transition from a standard rising bubble to a Taylor bubble, where the interaction of the bubble with the tube walls has a capital influence in the dynamics of the bubble. For k greater than 0.8 and lower than 1.1, the bubble tends to take a bullet shape. Beyond this critical point, any increase in the total volume of the bubble results in increasing the axial length without changing the shape of the nose and the rear end of the bubble. Finally, for $k > 1.2$ the bubble becomes slug-shaped. This behaviour is consistent with the one observed by other authors (i.e. Li et al. [33] and Amaya et al. [20]).

Additional results are shown in Fig. 3.9 as function of the bubble size, characterized by the parameter k. First, the Reynolds number is plotted in Fig. 3.9a. For small k values ($k < 1$), the velocity of the bubble grows almost linearly as k does, as a result of the increase in the buoyancy force. As the bubble size becomes comparable to the tube size, the confining walls make the drag force increase. These results in a stagnation of the Reynolds number at $k \approx 1.0$, when the bubble velocity becomes independent of its volume. Furthermore, Fig. 3.9c shows the relationship between k and the film thickness δ. As the volume of the bubble increases, the film thickness is reduced until achieve a stagnation point at $k \approx 1.1$. From this point on, the value of δ stays con-

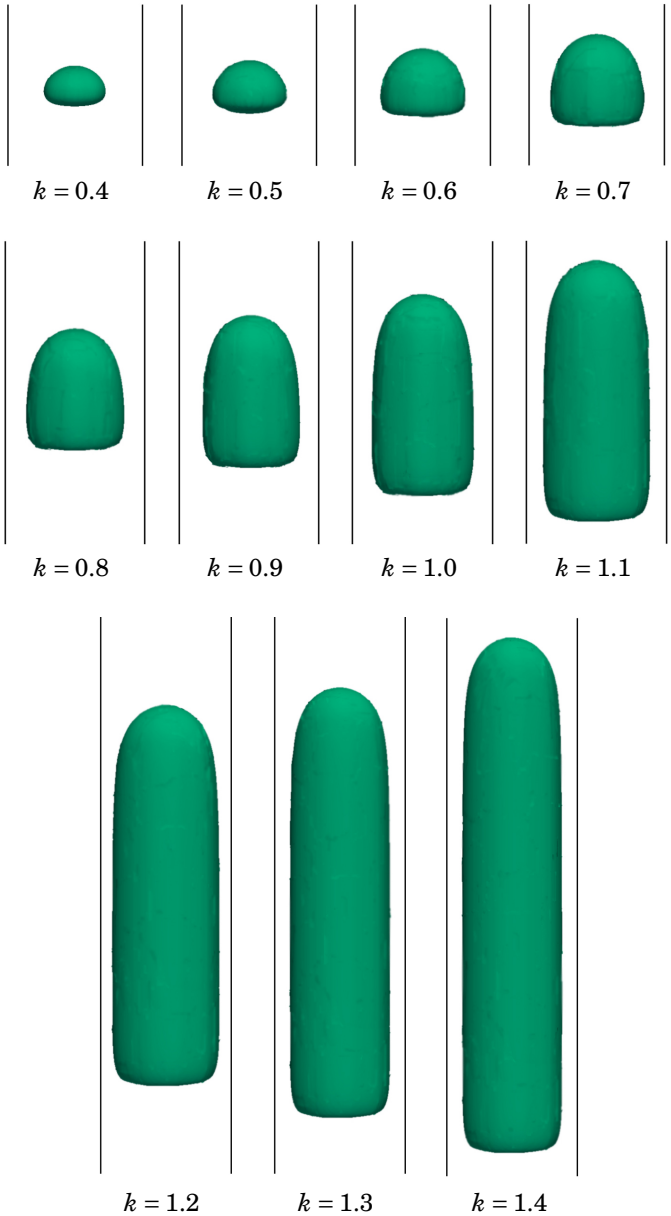

Figure 3.8: Final shapes in the study of the sensibility to the initial volume of the bubble, listed in increasing order from $k = 0.4$ to $k = 1.4$, with 0.1 increases.

Case	h	Re_T	Δ	E_{Re_T}	E_Δ
$k = 0.4$	$h = D/44$	24.776	−0.2175	6.7%	7.5%
	$h = D/58$	25.450	−0.2341	4.2%	0.5%
	$h = D/70$	26.067	−0.2362	1.9%	0.4%
	$h = D/84$	26.575	−0.2352	–	–
$k = 1.4$	$h = D/44$	26.032	0.6543	3.6%	5.1%
	$h = D/58$	26.311	0.6629	2.6%	3.7%
	$h = D/70$	26.883	0.6429	0.5%	1.9%
	$h = D/84$	27.012	0.6307	–	–

Table 3.3: Mesh independence study for the extreme cases $k = 0.4$ and $k = 1.4$, where h is the characteristic cell size, Re_T is the terminal Reynolds number, Δ is the deformation parameter, E_{Re_T} is the relative error of the terminal Reynolds number referred to the case with a denser mesh, and E_Δ is analogously the relative error of the deformation parameter.

stant and the increment of the bubble volume has an impact exclusively on the bubble axial length, but not on its proximity to the walls. This pattern is coherent with the behaviour observed in the evolution of the deformation parameter $\Delta = (L - B)/(L + B)$, where L is the length of the bubble and B is its width. Δ increases as k increases, with a decreasing slope, due to the fact that B achieves an approximately constant value for high values of k. Finally, the fraction of the total channel cross-sectional area occupied by the bubble $A_{\text{bubble}}/A_{\text{channel}}$ is plotted as function of k in Fig. 3.9d. This figure reflects how large bubbles ($k > 1.1$) occupy the same fraction of the total cross-sectional area available. All these results corroborate the findings of Li et al. [33] and Amaya et al. [20], presenting similar tendencies and analogous general behaviours.

3.3.5 Effect of the Eötvös number

The importance of surface tension forces compared to body forces is measured by terms of the Eötvös number Eo. In order to quantify this influence in the Taylor bubble problem, some experiments proposed by Hayashi et al. [23] have been addressed. In this paper, several cases are studied for different sets of Eötvös and Morton numbers. For a fixed Morton number, up to four different Eötvös numbers are studied. Therefore, we chose a Morton number Mo of $10^{-2.5}$ and we took the following set of Eötvös numbers: $Eo = \{10, 33, 55, 77\}$.

Experimental conditions of these four cases are described below. First, density and viscosity of the suspending fluid are respectively 1220kg/m^3 and $85.0 \cdot 10^{-3}$Pa$\cdot$s. The density ratio η_ρ and the viscosity ratio η_μ are respectively set to 1.26 and 0.88. The surface tension coefficient is 0.031N/m. Variations in the Eötvös number are obtained

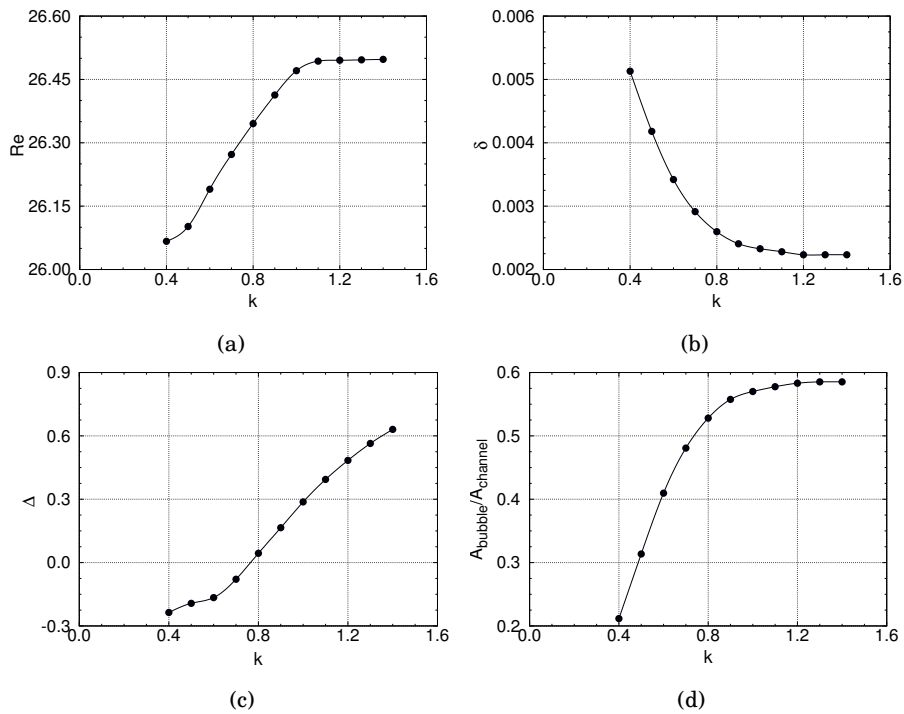

Figure 3.9: Comparison of (a) Reynolds number Re, (b) film thickness δ, (c) deformation parameter Δ and (d) fraction of maximum channel cross-sectional area occupied by the bubble $A_{\text{bubble}}/A_{\text{channel}}$, as a function of the bubble size characterized by the parameter k.

by changing the diameter of the tube, $D = \{0.011, 0.0201, 0.0261, 0.0308\}$ m. The initial bubble has a cylindrical shape with two hemispheres, and a total volume corresponding to a parameter k of 1.25. The initial radius of the bubble r is calculated from Eq. 3.17. The used meshes are the same as the `M2` mesh described above, but scaled to the new sizes.

A comparison between obtained results and reference data is summarized in Tab. 3.4, where a good agreement can be noticed. Furthermore, Fig. 3.10 depicts the profiles evolution for the run cases. The final shapes represented in this figure match qualitatively well with the images of the bubble provided by Hayashi et al. [23]. As can be further seen from these results, velocity increases when the Eötvös number increases. Due to the higher buoyant forces, the elongation of the bubble also increases whit the Eötvös number. For small Eötvös numbers, the bubble tends to take an elongated egg shape

(Fig. 3.10a and 3.10b). On the contrary, the bubble acquires a slug shape when higher Eötvös numbers are used (Fig. 3.10c and 3.10d).

Eo	Re_T		E_{Re_T}
	Present work	Hayashi et al. [23]	
10	0.40	0.41	2.43%
33	8.48	8.7	2.53%
55	19.62	20.2	2.87%
77	30.57	31.0	1.39%

Table 3.4: Results comparison against the experiments of Hayashi et al. [23], where E_{Re_T} is the relative error of the terminal Reynolds number Re_T.

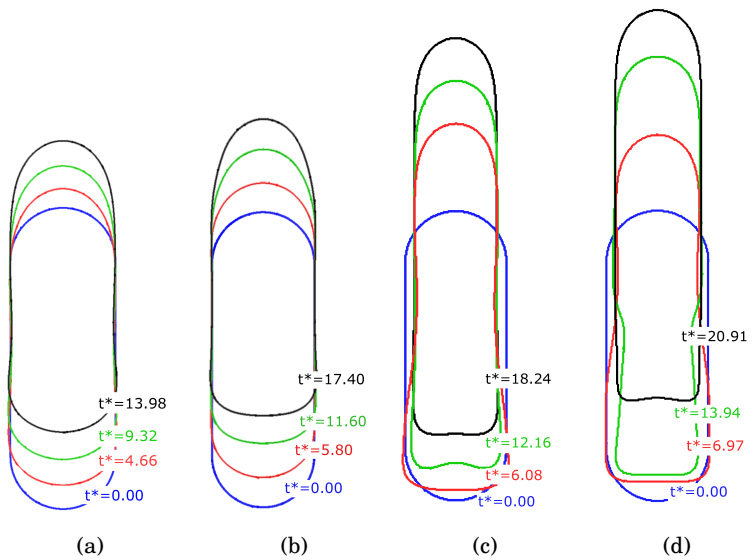

Figure 3.10: Evolution profiles of the three-dimensional Taylor bubble, corresponding to the different Eötvös numbers tested, i.e. (a) $Eo = 10$, (b) $Eo = 33$, (c) $Eo = 55$ and (d) $Eo = 77$. The other parameters have remained the same.

3.3.6 Effect of the Morton number

In order to study the particularities of the problem when varying the Morton number, we chose some of the cases studied by Quan [18], and we simulated them. In the mentioned paper, the inverse viscosity number N_f is used to describe the flow regime,

instead of the Morton number Mo. Both dimensionless numbers are related by the following expression:

$$N_f = \left(\frac{Eo^3}{Mo}\right)^{1/4} \tag{3.18}$$

On the one hand, the viscosity of the first fluid is determined from N_f, taking $g = 9.85\text{m/s}^2$. We select the following set of inverse viscosity numbers to be tested: $N_f = \{291, 200, 109, 44, 22, 16\}$. On the other hand, the density of the suspending fluid is 1220kg/m^3. The density ratio η_ρ and the viscosity ratio η_μ are both set to 100. The surface tension coefficient is 0.06N/m. The tube's diameter D is 0.032m. The initial bubble has a cylindrical shape with two hemispheres, with $k = 1.14$. The initial radius of the bubble r is obtained by computing Eq. 3.17. The used mesh is the same as the `M2` mesh described above, but scaled to fit the new geometry.

Tab. 3.5 summarizes the obtained terminal Reynolds numbers (Re_T) compared against those reported by Quan [18]. Good agreement was found between both sets of results. The slight differences between these results are caused by the different numerical approaches, and mainly because Quan is using an axisymmetric solver. Fig. 3.11 shows the profile's evolution and the final form of the tested cases. Again, the agreement of these results is qualitatively good in comparison with those obtained by Quan [18]. When decreasing Mo (i.e. increasing N_f), some general effects are observed in the performance of the problem. First, the bubble rises faster, as a result of the decrease in the viscous force. Additionally, the slug shape is progressively transformed into a skirted oval shape. The length of the main body of the bubble decreases, which indicate that the reduction of the viscous forces tends to compress the bubble. It becomes thicker, which is evidenced by a narrower film region between the tube wall and the bubble.

Regime		Re_T		E_{Re_T}
N_f	Mo	Present work	Quan [18]	
291	$2.12 \cdot 10^{-3}$	95.97	97.0	1.06%
200	$9.53 \cdot 10^{-3}$	65.65	65.6	0.07%
109	$1.36 \cdot 10^{-1}$	32.78	33.6	2.44%
44	4.07	10.59	10.9	2.83%
22	$6.31 \cdot 10^{1}$	3.59	3.8	5.42%
16	$2.33 \cdot 10^{2}$	1.69	1.8	6.11%

Table 3.5: Results comparison against the numerical experiments of Quan [18], where E_{Re_T} is the relative error of the terminal Reynolds number Re_T.

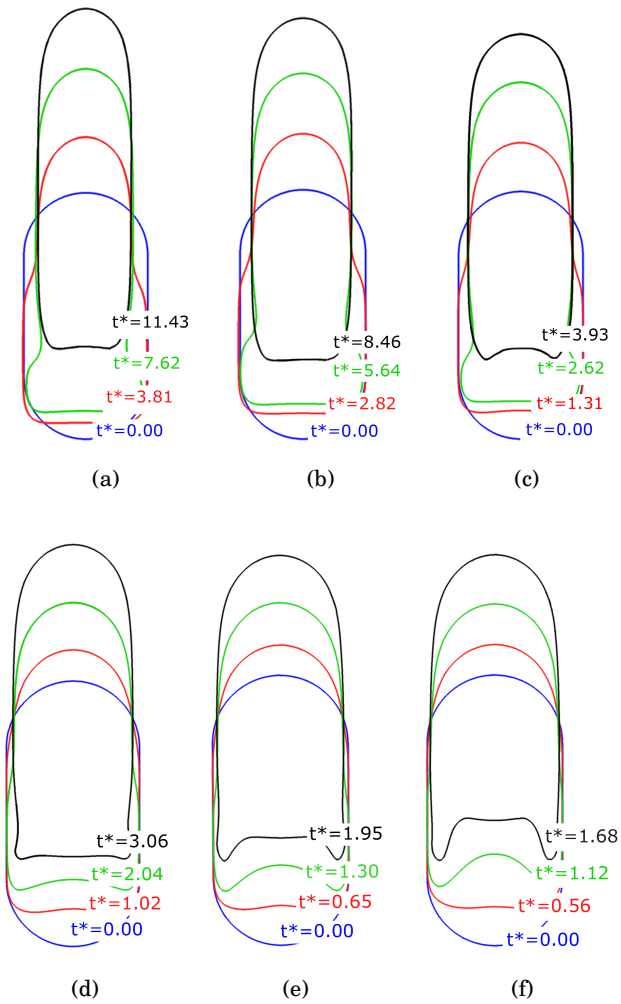

Figure 3.11: Evolution profiles of the three-dimensional Taylor bubble problem when varying the Morton number. These graphs show different inverse viscosity numbers tested, i.e. (a) $N_f = 16$, (b) $N_f = 22$, (c) $N_f = 44$, (d) $N_f = 109$, (e) $N_f = 200$ and (f) $N_f = 291$.

3.3.7 Effect of channel inclination

A comprehensive study of the Taylor bubble behaviour under non-vertical inclinations is herewith presented. We chose the work of Shosho and Ryan [14] as reference. In this paper, several mixtures were experimentally tested in cylindrical inclined tubes.

The selected parameters for the study are presented below. The inside diameter of the tube D is 0.0254m. The bubble's initial shape is a cylinder with a diameter d of $0.84D$. This cylinder is ended by two hemispheres, and it has a total length of $2d$, corresponding to $k = 1.14$. The density of the suspending fluid is 1320.02g/m^3 and its viscosity 0.191Pa$\cdot$s. Surface tension coefficient is set to 0.051N/m. These parameters give rise to a Eötvös number Eo of 40.97 and a Morton number Mo of 0.0746. The density ratio η_ρ and viscosity ratio η_μ are both set to 100. It is important to point out that these ratios do not match with the actual ratio of corn syrup-air mixture used in the experiment of Shosho and Ryan [14]. However, such large density and viscosity ratios give rise to numerical instabilities, and terminal velocity and bubble shapes are minimally upset when smaller ratios are used [18].

The new flow regime and the non-axisymmetric configuration of the current case, bring about a more challenging problem compared to the previous ones. Thus, a new mesh is designed to meet the resolution requirements of the current simulations. It is composed of triangular prismatic control volumes. A mesh independence study has been performed for the extreme case ($\theta = 5\pi/12$), in order to obtain a suitable mesh which accurately reproduce the physics of the problem. The results of this study are presented in Tab. 3.6, showing that a mesh with 147 control volumes per diameter seems to be a suitable mesh to study this problem.

Case	h	Fr	Δ	E_{Fr}	E_Δ
$\theta = 5\pi/12$	$h = D/103$	0.3297	0.7239	1.0%	6.5%
	$h = D/123$	0.3304	0.6585	0.4%	3.1%
	$h = D/147$	0.3307	0.6755	0.2%	0.6%
	$h = D/165$	0.3316	0.6796	–	–

Table 3.6: Results of the mesh independence study for the extreme case $\theta = 5\pi/12$, where h is the characteristic cell size, Fr is the Froude number, Δ is the deformation parameter, E_{Fr} is the relative error of the Froude number referred to the case with denser mesh, and E_Δ is analogously the relative error of the deformation parameter.

The distance h_o from the bubble rear end to the outflow should also be reconsidered. The use of Eq. 2.44 could a priori not be convenient for inclined cases, where their particular configurations give rise to longer wakes. Therefore, a particular study of the influence of the distance h_o (controlled by the safety constant $\mathscr{C}_{h_o}$) has been conducted. Results of this study have been summarized in Tab. 3.7), showing that the deformation parameter and the Froude number are minimally upset by increasing h_o, when $\mathscr{C}_{h_o} \approx$

2.5. This fact reveals that for $\mathscr{C}_{h_o} = 2.27$ the obtained h_o from Eq. 2.44 is enough to accurately reproduce the physics of the problem.

Case	$\mathscr{C}_{h_o}$	Fr	Δ	E_{Fr}	E_Δ
	$\mathscr{C}_{h_o} = 2.27$	0.3307	0.6755	0.6%	1.0%
$\theta = 5\pi/12$	$\mathscr{C}_{h_o} = 2.60$	0.3318	0.6749	0.3%	0.5%
	$\mathscr{C}_{h_o} = 2.90$	0.3328	0.6735	–	–

Table 3.7: Study of the influence of the distance h_o (controlled by $\mathscr{C}_{h_o}$) for the extreme case $\theta = 5\pi/12$, where $\mathscr{C}_{h_o}$ is the safety constant of Eq. 2.44, Fr is the Froude number, Δ is the deformation parameter, E_{Fr} is the relative error of the Froude number referred to the case with longer domain, and E_Δ is analogously the relative error of the deformation parameter.

Thus, the new mesh consists of $2.9 \cdot 10^6$ cells and is obtained by a constant step extrusion of a two-dimensional grid along the tube axis. The total tube length y_{length} is $5D$, the number of planes in which the vertical axis is divided N_{length} is 334, the number of cells per plane is 8546, and the characteristic cell dimension is $h_{\min} = 2.283 \cdot 10^{-4}$m.

The inclination of the channel is controlled by setting the angle θ between the tube's axis and the gravity vector. The set of studied angles is $\theta = \{0, \pi/6, \pi/4, \pi/3, 5\pi/12\}$ (in radians).

In Tab. 3.8 and Fig. 3.13 a comparison of the results obtained in the present work against those of Shosho and Ryan [14] is presented. This comparison is made in terms of the Froude number Fr, finding a good agreement. Furthermore, Fig. 3.13 shows the general tendency of the Taylor bubble terminal velocity when the channel inclination increases: it rises and reaches its maximum at an inclination close to $\pi/4$, and then decreases. This behaviour was noted by other researchers in many different configurations, i.e. with arbitrary cross-section channels [34] or with different types of mixtures [14]. Moreover, Fig. 3.12 shows the time evolution of the Froude number for the different inclination angles.

θ	Fr		E_{Fr}
	Present work	Shosho and Ryan [14]	
0	0.2949	0.2854	3.33%
$\pi/6$	0.3504	0.3520	0.45%
$\pi/4$	0.3733	0.3760	0.72%
$\pi/3$	0.3679	0.3627	1.43%
$5\pi/12$	0.3307	0.3173	4.22%

Table 3.8: Comparison of results against the experiments of Shosho and Ryan [14], where Fr is the Froude number and E_{Fr} is the relative error.

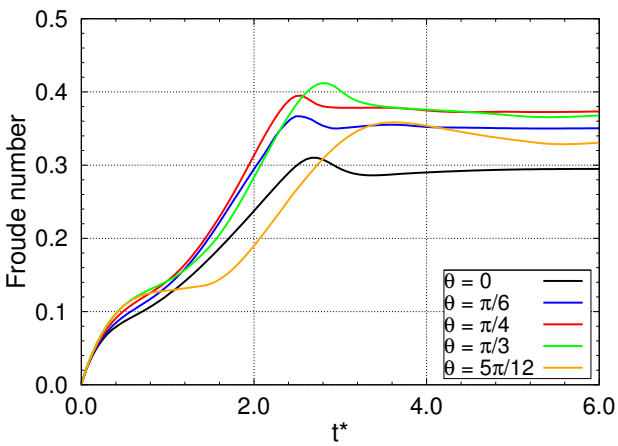

Figure 3.12: Sketch of the evolution of the Froude number over dimensionless time $t^* = tg^{1/2}D^{-1/2}$ for the tested inclinations, compared against results of Shosho and Ryan [14].

Further results are presented in the following figures. First, the final 3D bubble shapes are shown in Fig. 3.14. This figure shows how the average diameter of the bubble is reduced as the inclination increases, leading to a growth in the bubble length. Additionally, the distance between the bubble and the wall is reduced as the inclination angle increases. Similarly, the bubble nose gets closer to the wall as the channel is inclined. The lateral region opposite to the wall remains practically parallel to it.

Fig. 3.15 depicts the pressure fields of the different studied inclinations. As seen in this figure, the range of variation of the pressure is similar for the different angles. Moreover, the illustrations show how the pressure isosurfaces have a tendency of being perpendicular to the gravity vector.

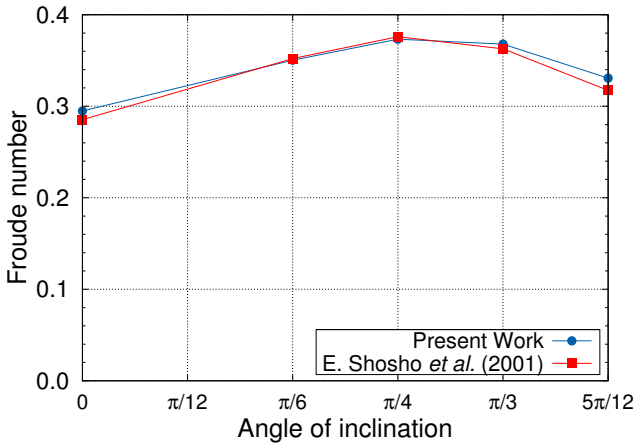

Figure 3.13: Evolution of the terminal Froude number over dimensionless time $t^* = tg^{1/2}D^{-1/2}$ for the tested inclination angles, compared against the results of Shosho and Ryan [14].

Furthermore, Fig. 3.16 shows the streamlines for all inclination angles in the XY plane. In the vertical case (Fig. 3.16a), a pair of elongated counter-rotating vortices are found inside the bubble. The symmetry of this configuration is lost as the tube is inclined. The vortex at the far side of the wall is still formed, while the one close to the wall opens up reducing its size and moving downward.

Finally, Figs. 3.17-3.21 depict the streamlines and the Y-component of the vorticity field in the XZ plane at three different elevations of y-axis. The placement of these elevations is obtained by dividing the bubble's total length into four parts. Fig. 3.14 shows these positions for the different inclination angles, labeled as `Y1`, `Y2` and `Y3` in order of increasing height. The variation range of the vorticity is within the same order of magnitude in all inclination angles and all elevations, although it slightly increases with the inclination angle. For the vertical case (Fig. 3.17), the streamlines present a well-defined configuration of counter-rotating vortices along the bubble perimeter. This axis-symmetric arrangement is vanished as the inclination angle increases. In general, for the inclined cases (Figs. 3.18-3.21), two regions of opposite vorticity can be found in both sides of the bubble. This configuration becomes increasingly clear when the inclination rises. The lowest elevation `Y1` seems more perturbed and asymmetric due to the effect of the instability of the rear end. Secondary vortices appear at the perimeter of the tube in some specific configurations (e.g. see Fig. 3.20a). The `Y3` plot seems similar for the different inclination angles (see Figs. 3.18c, 3.19c, 3.20c and 3.21c), presenting an asymptotic-like pattern starting at the right side of the tube and going

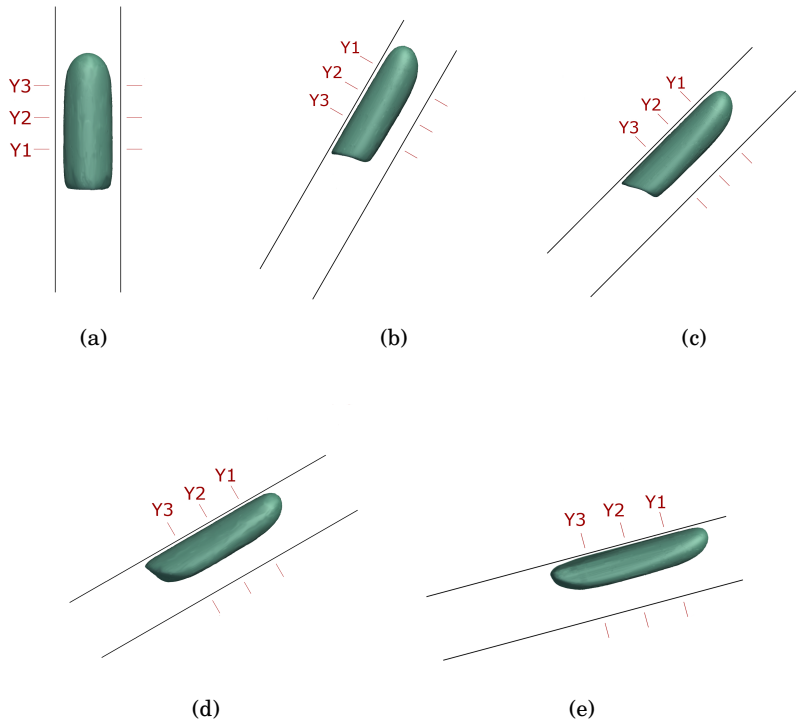

Figure 3.14: Three dimensional shape of the tested cases in the study of tube inclination:(a) 0, (b) $\pi/6$, (c) $\pi/4$, (d) $\pi/3$ and (e) $5\pi/12$. Labels Y1, Y2 and Y3 mark the elevations at where streamlines and the vorticity field are analyzed in Figs. 3.17-3.21.

to the centre of the bubble. This behaviour is consistent with results reported by [20].

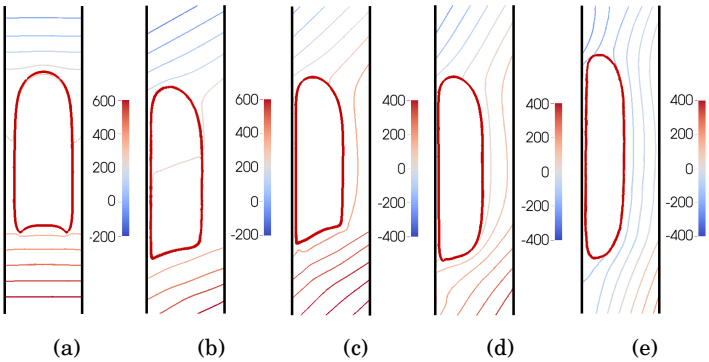

Figure 3.15: Pressure fields (in Pa) for all inclination angles studied: (a) 0, (b) $\pi/6$, (c) $\pi/4$, (d) $\pi/3$ and (e) $5\pi/12$.

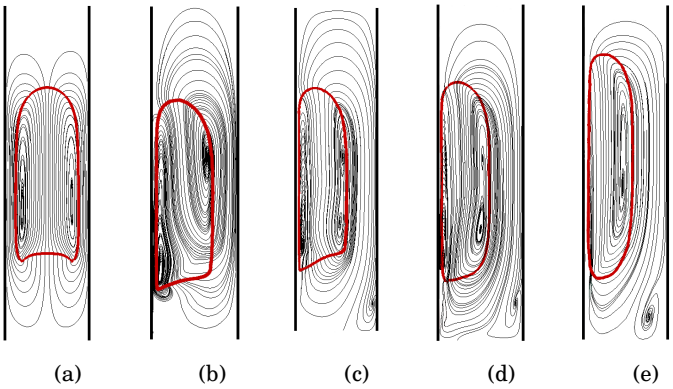

Figure 3.16: Streamlines in XY plane for all inclination angles studied: (a) 0, (b) $\pi/6$, (c) $\pi/4$, (d) $\pi/3$ and (e) $5\pi/12$.

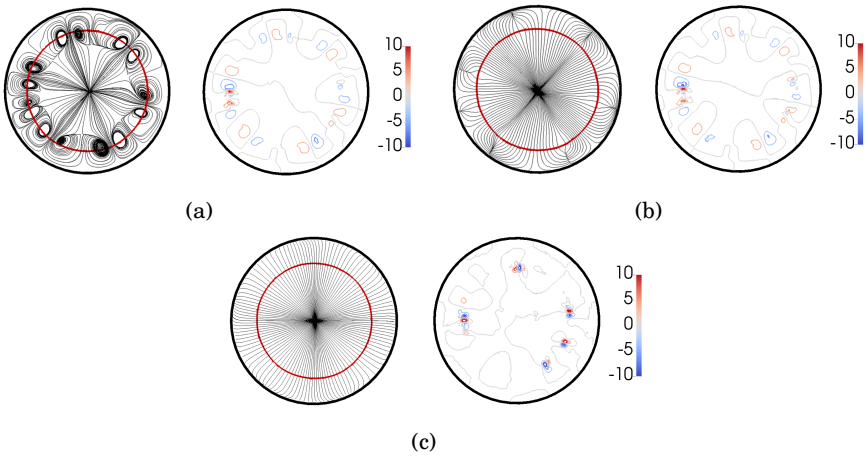

Figure 3.17: Streamlines and vorticity field (s^{-1}) in XZ plane at the three different elevations (a) `Y1`, (b) `Y2` and (c) `Y3`, corresponding to the 0 inclination case.

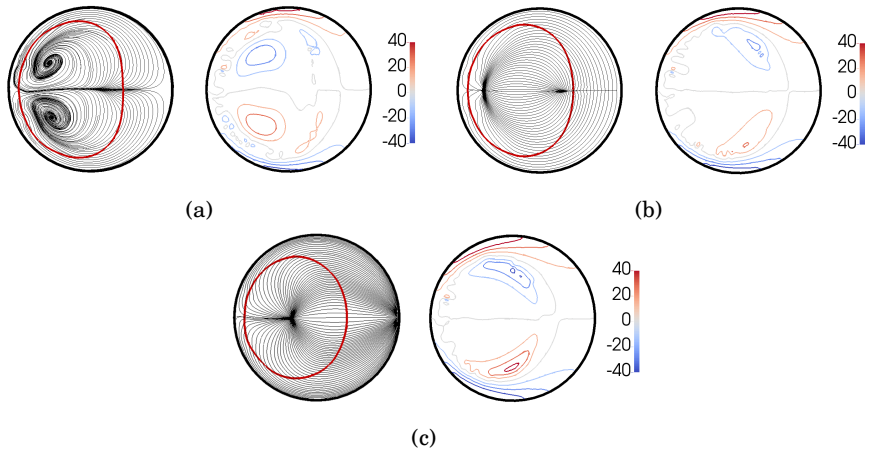

Figure 3.18: Streamlines and vorticity field (s^{-1}) in XZ plane at the three different elevations (a) `Y1`, (b) `Y2` and (c) `Y3`, corresponding to the $\pi/6$ inclination case.

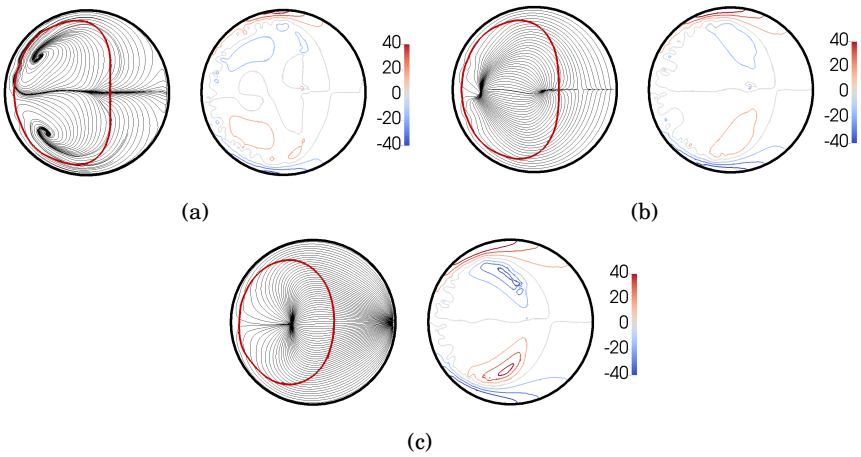

Figure 3.19: Streamlines and vorticity field (s^{-1}) in XZ plane at the three different elevations (a) `Y1`, (b) `Y2` and (c) `Y3`, corresponding to the $\pi/4$ inclination case.

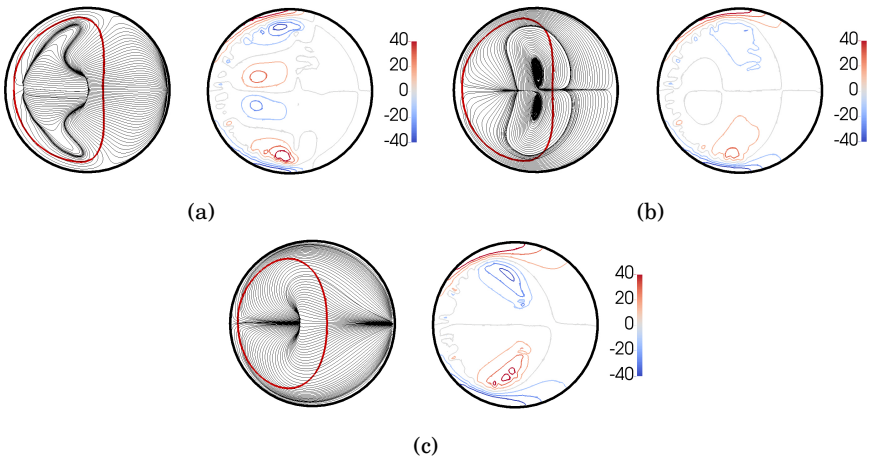

Figure 3.20: Streamlines and vorticity field (s^{-1}) in XZ plane at the three different elevations (a) `Y1`, (b) `Y2` and (c) `Y3`, corresponding to the $\pi/3$ inclination case.

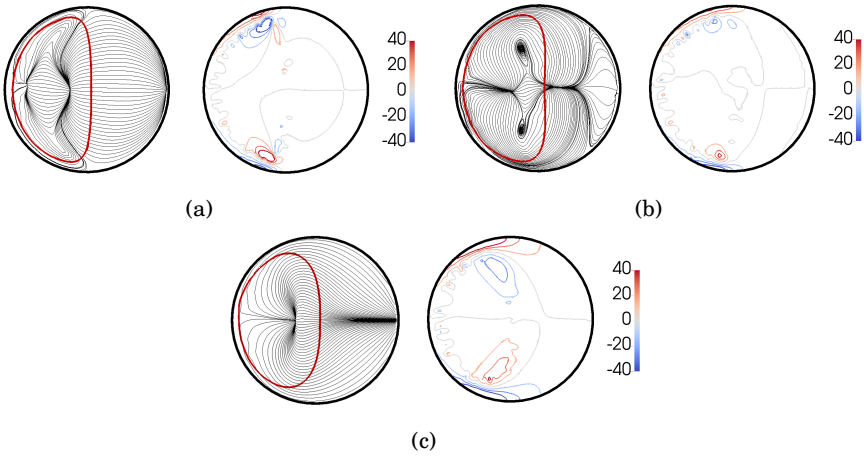

Figure 3.21: Streamlines and vorticity field (s^{-1}) in XZ plane at the three different elevations (a) Y1, (b) Y2 and (c) Y3, corresponding to the $5\pi/12$ inclination case.

3.4 Conclusions

In the present work, an Arbitrary Lagrangian-Eulerian approach to optimize the computational domain in Taylor bubbles problems have been posed, within a conservative level set framework. The method was used to perform a deep study of the Taylor bubble problem.

By using an optimized domain, the efficiency of the simulation can be notably improved, due to the fact that it is no longer necessary to solve regions far from the vicinities of the bubble, which are not of interest in rising bubble problems. The method is based on a moving grid that follows the ascent of the buoyant bubble. It showed a proper numerical stability and a good performance. The only noteworthy disadvantage of this method is that it needs using open boundaries (namely, inflow and outflow), which usually requires a careful numerical treatment, as explained in Sec. 3.2.4. In effect, the formulation and the placement of the open boundaries (specially the outflow) are burdensome factors to be taken into account in designing these boundaries. Those difficulties were handled by taking into account the conclusions obtained in Sec. 2.4 and 2.5 about the design and placement of these boundaries.

The previous method was used to tackled the challenging problem of the three dimensional Taylor bubble. To the best knowledge of the authors, this problem has not been previously addressed by using a CLS method. An in-depth study was carried out, including the sensitivity analyses with respect to the initial shape of the bubble, the initial volume of the bubble, the flow regime and the inclination of the channel. All

the aforementioned tests have been compared with both experimental and numerical studies available in the literature, finding a very good agreement.

References

[1] W. Salman, A. Gavriilidis, P. Angeli, On the formation of Taylor bubbles in small tubes, Chem. Eng. Sci. 61 (2006) 6653-6666.

[2] E. W. Llewellin, E. Del Bello, J. Taddeucci, P. Scarlato, S. J. Lane, The thickness of the falling film of liquid around a Taylor bubble, Proc. R. Soc. A. 468 (2012) 1041-1064.

[3] O. Estruch, O. Lehmkuhl, R. Borrell, C. D. Pérez Segarra, A. Oliva, A parallel radial basis function interpolation method for unstructured dynamic meshes, Comput. Fluids. 80 (2013) 44-54.

[4] J.T. Batina, Unsteady Euler airfoil solutions using unstructured dynamic meshes, AIAA J. 28 (1990) 1381-1388.

[5] Y. Bazilevs, K. Takizawa, T.E. Tezduyar, Computational Fluid-Structure Interaction, Wiley, Hoboken, 2013.

[6] N. Balcázar, L. Jofre, O. Lehmkuhl, J. Castro, J. Rigola, A finite-volume/level-set method for simulating two-phase flows on unstructured grids, Int. J. Multiph. Flow. 64 (2014) 55-72.

[7] N. Balcázar, O. Lehmkuhl, J. Rigola, A. Oliva, A multiple marker level-set method for simulation of deformable fluid particles, Int. J. Multiph. Flow. 74 (2015) 125-142.

[8] N. Balcázar, O. Lehmkuhl, L. Jofre, A. Oliva, Level-set simulations of buoyancy-driven motion of single and multiple bubbles, Int. J. Heat Fluid Flow. 56 (2015) 91-107.

[9] R.M. Davies, G. Taylor, The Mechanics of Large Bubbles Rising through Extended Liquids and through Liquids in Tubes, Proc. R. Soc. A Math. Phys. Eng. Sci. 200 (1950) 375-390.

[10] E.T. White, R.H. Beardmore, The velocity of rise of single cylindrical air bubbles through liquids contained in vertical tubes, Chem. Eng. Sci. 17 (1962) 351-361.

[11] R.Sh. Abiev, I.V. Lavretsov, Hydrodynamics of gas liquid Taylor flow and liquid solid mass transfer in mini channels: Theory and experiment, Chem. Eng. J. 176-177 (2011) 57-64.

[12] S. Bhusan, S. Ghosh, G. Das, P.K. Das, Rise of Taylor bubbles through narrow rectangular channels, Chem. Eng. J. 155 (2009) 326-332.

[13] J.D. Bugg, G.A. Saad, The velocity field around a Taylor bubble rising in a stagnant viscous fluid: Numerical and experimental results, Int. J. Multiph. Flow. 28 (2002) 791-803.

[14] C.E. Shosho and M.E. Ryan, An experimental study of the motion of long bubbles in inclined tubes, Chem. Eng. Sci. 56 (1999) 2191-2204.

[15] Y.B. Zudin, Analytical solution of the problem of the rise of a Taylor bubble, Phys. Fluids. 25 (2013).

[16] T. Funada, D.D. Joseph, T. Maehara, S. Yamashita, Ellipsoidal model of the rise of a Taylor bubble in a round tube, Int. J. Multiph. Flow. 31 (2005) 473-491.

[17] M. Dang, J. Yue, G. Chen, Q. Yuan, Formation characteristics of Taylor bubbles in a microchannel with a converging shape mixing junction, Chem. Eng. J. 223 (2013) 99-109.

[18] S. Quan, Co-current flow effects on a rising Taylor bubble, Int. J. Multiph. Flow. 37 (2011) 888-897.

[19] A. Kuzmin, M. Januszewski, D. Eskin, F. Mostow, J. J. Derksen, Lattice Boltzmann study of mass transfer for two-dimensional Bretherton/Taylor bubble train flow, Chem. Eng. J. 225 (2013) 580-596.

[20] L. Amaya-Bower, T. Lee, Numerical simulation of single bubble rising in vertical and inclined square channel using lattice Boltzmann method, Chem. Eng. Sci. 66 (2011) 935-952.

[21] R.Sh. Abiev, Bubbles velocity, Taylor circulation rate and mass transfer model for slug flow in milli- and microchannels, Chem. Eng. J. 227 (2013) 66-79.

[22] N.V. Ndinisa, D.E. Wiley, D.F. Fletcher, Computational Fluid Dynamics Simulations of Taylor Bubbles in Tubular Membranes: Model Validation and Application to Laminar Flow Systems, Chem. Eng. Res. Des. 83 (2005) 40-49.

[23] K. Hayashi, R. Kurimoto, A. Tomiyama, Terminal velocity of a Taylor drop in a vertical pipe, Int. J. Multiph. Flow. 37 (2011) 241-251.

[24] G. Tryggvason, B. Bunner, A. Esmaeeli, D. Juric, N. Al-Rawahi, W. Tauber, J. Han, S. Nas, Y.J. Jan, A Front-Tracking Method for the Computations of Multiphase Flow, J. Comput. Phys. 169 (2001) 708-759.

[25] E. Olsson and G. Kreiss, A conservative level set method for two phase flow, J. Comput. Phys. 210 (2005) 225-246.

[26] A. Harten, The artificial compression method for computation of shocks and contact discontinuities. III - Self-adjusting hybrid schemes, Math. Comp. 32 (1978) 363-389.

[27] J.U. Brackbill, D.B. Kothe, C. Zemach, A continuum method for modeling surface tension, J. Comput. Phys. 100 (1992) 335-354.

[28] S. Gottlieb and C. Shu, Total variation diminishing Runge-Kutta schemes, Math. Comp. (1998), 67, 73-85.

[29] A.J. Chorin. Numerical solution of the Navier-Stokes equations, Math. Comp. 22 (1968), 745-762.

[30] J.L. Guermond, P. Minev, J. Shen, An overview of projection methods for incompressible flows, Comput. Methods Appl. Mech. Eng. 195 (2006) 6011-6045.

[31] N. Balcázar, J. Rigola, J. Castro, A. Oliva, A level-set model for thermocapillary motion of deformable fluid particles, Int. J. Heat Fluid Flow. October 2016.

[32] R. A. S. Brown, The mechanics of large gas bubbles in tubes: I. Bubble velocities in stagnant liquids, Can. J. Chem. Eng. 43 (1965) 217-223.

[33] J. Li, V. Bulusu, N.R. Gupts, Buoyancy-driven motion of bubbles in square channels, Chem. Eng. Sci. 63 (2008) 3766-3774.

[34] C. Clanet, P. Héraud, G. Searby, On the motion of bubbles in vertical tubes of arbitrary cross-sections: some complements to the Dumitrescu-Taylor problem, J. Fluid Mech. 519 (2004) 359-376.

4

Bubbles and drops evolving through complex geometries

Main contents of this chapter have been published in:

E. Gutiérrez, F. Favre, N. Balcázar, A. Amani and J. Rigola Numerical approach to study bubbles and drops evolving through complex geometries by using a level set - moving mesh - immersed boundary method, Chemical Engineering Journal 349 (2018), 662-682

Abstract. The present chapter proposes a method to study problems of drops and bubbles evolving in complex geometries. First, a conservative level set (CLS) method is enforced to handle the multiphase domain while keeping the mass conservation under control. An Arbitrary Lagrangian-Eulerian (ALE) formulation is proposed to optimize the simulation domain. Thus, a moving mesh (MM) will follow the motion of the bubble, allowing the reduction of the computational domain size and the improvement of the mesh quality. This has a direct impact on the computational resources consumption which is notably reduced. Finally, the use of an Immersed Boundary (IB) method allows to deal with intricate geometries and to reproduce internal boundaries. The resulting method is capable of dealing with full unstructured meshes. Different problems have been studied to assert the proposed formulation. In particular, the following problems have been addressed: a 2D gravity-driven bubble interacting with a highly-inclined plane, a 2D gravity-driven Taylor bubble turning into a curved channel, the approach of a 3D drop towards a solid plane, the 3D passage of a drop through a periodically constricted channel, and the impingement of a 3D drop on a flat plate. Good agreement was found for all these cases, which proves the suitability of the proposed CLS+MM+IB method to study this type of problems.

4.1 Introduction

The motion of drops and bubbles in complex geometries is of fundamental importance in many scientific and engineering applications. To cite a few examples, chemical reactors generally involve many drop-wall collision processes [1], and its understanding could seriously determine the efficiency of the reactor. The field of microfuidics [2] and lab-on-a-chip concept are fed from the knowledge of the behaviour of bubbles and drops evolving through microgeometries. Additionally, the oil extraction processes could ultimately be reduced to the evolution of a slug flow through constricting solids.

The motion of bubbles and drops in unbound mediums has attracted significant scientific attention in the last decades (see Tryggvason et al. [3] for an extensive numerical review). On the contrary, the literature about bubbles/drops evolving through complex geometries is far more limited. A meaningful distinction within these problems is stressed here, depending on the relation between the secondary phase and the surrounding geometry. On the one hand, the solid could constrict the bubble or drop, and its trajectory is somehow predetermined by the own shape of the solid. On the other hand, the bubble/drop could freely evolve in an unbounded media, whereas the present solids alter its motion, but in an unconstrained manner. The border between both types of cases is diffuse, and the classification of a specific problem in one group or the other can be ambiguous. See Fig. 4.1 for a graphical interpretation of both types of problems.

In order to face both types of problems, different approaches have been proposed in the literature. Experimental procedures usually isolate the basic phenomenon to macroscopically study the motion of the secondary phase. See [4–7] for some valuable experimental works. Additionally, the problem of drops or bubbles evolving in complex geometries can also be addressed theoretically by simplifying the governing equations to extract analytical conclusions (see e.g. [8, 9]). Finally, some valuable numerical approaches have been conducted to solve the aforementioned problem [10–13]. Tab. 4.1 compiles some of the outstanding works present in the literature, highlighting the method used to solve the problem and the relationship between drop/bubble and geometry.

When facing this type of problems by using a numerical approach, three paramount issues should be addressed in order to satisfactorily solve the case study:

1. The fluid interface must be computed accurately while conserving integral properties.

2. The computational cost should be kept within reasonable bounds.

3. The solid geometries, which could be complex and intricate, should be represented effectively and robustly.

Reference (year)	Nature of study	Problem description [**C**onstrained / **U**nconstrained]
Worthington [5] (1876)	Experimental	Qualitative analysis of the impact of a gravity-driven falling drop against a horizontal plane. [**U**]
Hemmat and Borhan [4] (1996)	Experimental	Motion of buoyancy-driven drops in periodically constricted tubes. [**C**]
Hills and Chèty [14] (1998)	Experimental	Gravity-driven rising Taylor bubble in a concentric annulus tube. [**C**]
Zhao et al. [15] (1998)	2D Numerical (LS)	Gravity-driven drop flowing through an asymmetric funnel. [**C**]
Aleinov et al. [16] (1999)	3D axisymmetric Numeric (LS)	Ejection of a ink drop from a constricting nozzel. [**C**]
Klaseboer et al. [8] (2001)	Experimental and theoretical	Gravity-driven rising bubble impinging on a horizontal plate. [**U**]
Olgac et al. [17] (2006)	3D axisymmetric Numeric (FT)	Motion of buoyancy-driven drops in periodically constricted tubes. [**C**]
Podvin et al. [9] (2008)	Experimental and theoretical	Interaction of a bubble with a plane at different inclinations. [**U**]
Deen et al. [10] (2009)	3D Numerical (FT)	Bubbles impacting against a single sphere or an array of them. [**U**]
Protière et al. [18] (2010)	Experimental	Passage of a 2D Taylor bubble through a cylindrical obstacle. [**C**]
Roudet et al. [19] (2011)	Experimental	Pressure-driven slug flow in meandering millimetric square channels. [**C**]
Pozrikidis [20] (2012)	2D Numerical (FT)	Passage of a viscous liquid through a bifurcation. [**C**]
Liu et al. [6] (2015)	Experimental and 3D numerical (LB)	Drop falling against curved surfaces. [**U**]
Maitra et al. [7] (2014)	Experimental	Drops impacting superhydrophobic textures. [**U**]
Gupta et al. [11] (2014)	2D Numerical (LB)	Squeezing mechanism in a droplet formation device. [**U**]
Misra et al. [21] (2016)	3D axisymmetric Numeric (VoF)	Gravity-driven rising bubble passing through a circular orifice. [**C**]
Izbassarov and Muradoglu [22] (2016)	3D axisymmetric Numeric (FT)	Pressure-driven drop through a sudden contraction and expansion. [**C**]
Baltussen et al. [23] (2017)	3D Numerical (VoF)	Interaction of a gravity-driven rising bubble with a cylindrical solid. [**U**]

Table 4.1: Literature summary for bubbles/drops motion through complex geometries, ordered by year of publication. Here "LS" refers to "Level Set method", "FT" to "Front-Tracking method", "LB" to "Lattice-Boltzmann method", and "VoF" to "Volume of Fluids method".

Regarding the first item, there are two main groups of methods to deal with multiphase domains. On the one hand, the interface between fluids could be reproduced by using a Front-Tracking method [24]. These techniques accurately describe the multiphase flow, although their implementation may be burdensome due to the need of recomputing the mesh at each time step. On the other hand, the eulerian methods represent the multiphase domain by a continuous (though sharp) change of properties. Those methods include volume-of-fluid (VoF) techniques [25], level set (LS) methods [26, 27] and hybrid procedures (CLSVoF) [28]. Level set approaches have the advantage of precisely calculating the geometrical properties of the interface (i.e. normal and curvature). However, they present mass conservation drawbacks. On the contrary, the volume-of-fluid methods inherently conserve mass, but at the expense of a troublesome process of computing geometrical properties of the interface. Hybrid methods solve the two issues present in the above-mentioned techniques, but the computational cost significantly increases. In the present work, we propose a methodology based on a conservative level set (CLS) formulation for unstructured meshes, first reported by Balcázar et al. [29]. The CLS formulation dramatically reduces the mass conservation error in comparison with a standard level set method. This technique has been thoroughly verified [30, 31].

Further efforts have been reported in the development of conservative level-set methods, e.g. the level set remedy approach based on sigmoid function [32], and the accurate conservative level-set method [33]. In the present CLS formulation [29], interface normals are computed using a least-squares method on a wide and symmetric nodes-stencil around the vertexes of the current cell [29]. These normals are then used for an accurate computation of surface tension, without additional reconstruction of the distance function, as in geometrical volume-of-fluid/level-set methods [28] or fast-marching methods [33]. Moreover, most computational operations are local. Therefore this method is efficiently implemented for parallel platforms [29, 34]. The CLS method has been designed for general unstructured meshes [29]. Indeed, the grid can be adapted to any domain, enabling for an efficient mesh distribution in regions where interface resolution has to be maximized [28, 29, 31, 34, 35], which is difficult by using structured grids. Furthermore, a TVD flux-limiter scheme [29] is used to advect the CLS function, avoiding numerical oscillations around discontinuities, whereas the numerical diffusion is minimized. Finally, the present finite-volume formulation is attractive due to its simplicity and the satisfaction of the integral forms of the conservation laws over the entire domain [29].

When facing the problem of a bubble/drop evolving in complex geometries by using DNS methodologies, the computational resources consumption should be a topic of major concern. This is because the need of enough resolution to represent real geometries, together with the high-demanding process of solving the Navier-Stokes equations. With the exception of basic configurations, a decision should be taken regarding this point.

An option is to work under a 2D or axisymmetric hypothesis [11, 22]. However, if a full 3D approach is sought, a domain optimization method becomes mandatory (e.g. non-inertial reference frame, periodic domain, etc.). In the present work, we enforce a moving mesh (MM) technique to deal with small simulation domains. This Arbitrary Lagrangian-Eulerian (ALE) formulation is based upon the work of Estruch et al. [36]. The mesh follows the motion of the bubble/drop. Under those circumstances, the simulation domain can be limited to the important regions of the problem (i.e. the bubble/-drop and its surroundings). This allows a great saving of computational effort, together with other benefits (see Sec. 4.4). The drawback of this technique is introducing open boundary conditions at the domain limits, hindering the enforcement of solid conditions. The synergy with the immersed boundary method (introduced below) provides a workable solution to this inconvenience.

In the past few years the Immersed Boundary (IB) method has gained a special interest as an alternative to the body-conformal mesh methods. The IB methods highly simplify the mesh generation process, as they allow the use of cartesian meshes and the inclusion of moving and/or deforming bodies. In the present framework the IB method constitutes an efficient and simple way to include solid boundaries in the DNS simulations. The boundary condition is imposed by the modification of the discretized Navier-Stokes equations, generally by including a forcing term. Depending on how this forcing term is defined, the IB method is classified into two categories [37]: continuous forcing approach and the discrete forcing approach. The original IB method introduced by Peskin [38] in 1972 constitutes a continuous approach. In that work, the immersed boundary is represented by a series of Lagrangian markers linked by springs, which exert a singular force on the fluid by a discrete approximation to the Dirac delta function. This approach has been applied to numerous problems, e.g. biological flows with elastic boundaries [38–41]. It has also been used to represent rigid boundaries by increasing the stiffness of the body [42]. However, this approach can lead to stability problems. The discrete forcing approach was introduced by Mohd-Yusof [43] in a spectral method and applied by Fadlun et al. [44] using a finite difference approach. In this case, the forcing is defined in the discrete space by imposing the boundary condition in the solution. This process can be seen as a reconstruction procedure. In fact, in [44] the forcing is not evaluated explicitly. Numerous variants of this approach have been proposed, such as the direct forcing approach [45, 46], the ghost cell method [47, 48] and the Cartesian cut-cell method [49, 50]. The discrete forcing approach allows a sharp representation of the immersed boundary, and is well suited for rigid boundaries. For these reasons, a discrete forcing approach has been taken in the present work.

When an IB method is combined with a CLS method, the mass fluxes at the faces in the vicinity of the solid must be carefully computed to have an accurate convective term, and to ensure that the bubble/drop does not penetrate into the solid regions. The IB method is based on a velocity field reconstruction. However, due to the nature of

the fractional step method, the boundary condition is imposed to the predictor velocity. Therefore, an error is made as a result of performing the projection step after imposing the non-slip boundary condition. In this methodology, the solid boundaries are not impermeable and mass flux can pass through them. Thus, in the present formulation this undesirable effect is avoided by imposing a boundary condition to the pressure field using a cut cell based discretization [50, 51] only to the Poisson equation as in [52].

In light of the foregoing, the present work proposes a new insight to face problems where a bubble or drop is evolving through an arbitrary geometry (constricting or non-constricting). The method is a combination of a CLS technique to deal with the multiphase domain, an ALE framework to optimize the size of the simulation domain, and an IB method to represent the embedded solids. To the best of our knowledge, this work is the first approach to multiphase DNS problems combining a CLS technique, a dynamic mesh framework and an IB method. The resulting method is capable of dealing with full unstructured meshes, which greatly increases the versatility of this methodology.

The chapter is organized as follows: Sec.4.2 presents the mathematical description of the proposed CLS+MM+IB method. The numerical treatment of these equations is then addressed through Sec. 4.3, followed by a discussion on the applicability of the method (Sec. 4.4). Then, results of the validation and verification cases are presented in Sec. 4.5. Finally, conclusions are summarized in Sec. 4.6.

4.2 Mathematical formulation

In the present section, the mathematical foundation of the proposed CLS+MM+IB method to solve multiphase flows in complex geometries is presented. The equations to be solved are the Navier-Stokes equations with the hypotheses of incompressible flow, Newtonian fluids, no mass transfer at the fluids interface, Arbitrary Lagrangian-Eulerian framework, constant surface tension coefficient σ and embedded solids. Those equations are given by the conservation laws of mass and momentum, as follows:

$$\nabla \cdot \mathbf{v} = 0 \tag{4.1}$$

$$\frac{\partial}{\partial t}\left(\rho \mathbf{v}\right) + \nabla \cdot \left(\rho \mathbf{v}(\mathbf{v} - \mathbf{v}_{\text{domain}})\right) = -\nabla p + \nabla \cdot \mu \left(\nabla \mathbf{v} + (\nabla \mathbf{v})^T\right) + \rho \mathbf{g} + \sigma \kappa \mathbf{n} \delta_\Gamma + \Psi_{\text{IB}} \tag{4.2}$$

where t is the time, $\mathbf{v}$ is the velocity vector, $\mathbf{v}_{\text{domain}}$ is the domain velocity, p is the pressure, $\mathbf{g}$ is the gravity acceleration, σ is the constant surface tension coefficient, κ and $\mathbf{n}$ are respectively the curvature and the unit normal vector of the interface between fluids, δ_Γ is the Dirac delta function located at that interface, and Ψ_{IB} is an extra source term introduced by the immersed boundary method (see Sec. 4.3.2). Finally, ρ and μ are the fluid density and viscosity, respectively. These properties are

constant within each fluid. Thus, they can be expressed as a single property with a jump discontinuity at the interface, yielding the following equations:

$$\rho = \rho_1 H + \rho_2 (1 - H) \tag{4.3}$$

$$\mu = \mu_1 H + \mu_2 (1 - H) \tag{4.4}$$

Subscripts 1 and 2 refer to the suspending fluid and secondary phase, respectively; and H is the Heaviside function with its discontinuity located at the fluids interface. H is equal to zero in the secondary phase, and equal to 1 in the suspending fluid.

4.2.1 Interface capturing

Equations from 4.1 to 4.4 close a non-continuous problem, due to the jump of properties located at the interface and the surface tension source term of the momentum equation (Eq. 4.2) acting only at that interface. However, aiming to avoid numerical instabilities at the interface, a continuous treatment of the fluids properties is more convenient. A conservative level set (CLS) method, as introduced by [29] in the context of unstructured grids, is used to tackle with the fluid interface. Therefore, the interface is implicitly represented by an indicator function ϕ, defined as:

$$\phi(\mathbf{x}, t) = \frac{1}{2}\left(\tanh\left(\frac{d(\mathbf{x}, t)}{2\varepsilon}\right) + 1\right) \tag{4.5}$$

Here $d(\mathbf{x}, t)$ is the signed distance function, and ε is a parameter to control the thickness of the interface between fluids. This interface can be located by obtaining the $\phi = 0.5$ isosurface.
By means of the level set function, Eqs. 4.3 and 4.4 can be expressed as follows:

$$\rho = \rho_1 \phi + \rho_2 \left(1 - \phi\right) \tag{4.6}$$

$$\mu = \mu_1 \phi + \mu_2 \left(1 - \phi\right) \tag{4.7}$$

The solution of the Navier-Stoke equations (Eqs. 4.1 and 4.2) provides the velocity field $\mathbf{v}$ used to advect ϕ. This transport equation can be written as follows:

$$\frac{\partial \phi}{\partial t} + \nabla \cdot \phi(\mathbf{v} - \mathbf{v}_{\text{domain}}) = 0 \tag{4.8}$$

Note that this equation slightly differs from the advection equation used in previous chapters. The reason is that now the velocity of the mesh is not anymore constant within the domain, so it cannot be removed from the divergent operator. After advection, a reinitialization step is needed to complete the calculus of the level set function. In this step, the interface is compressed seeking to maintain a constant thickness, as

it tends to widen in the advection process due to numerical diffusion [53]. Therefore, the following differential equation is computed:

$$\frac{\partial \phi}{\partial \tau} + \nabla \cdot \phi \left(1 - \phi\right) \mathbf{n}_{\tau=0} = \nabla \cdot \varepsilon \nabla \phi \tag{4.9}$$

This equation is advected in pseudo-time τ. On the one hand, the term $\phi\left(1-\phi\right)\mathbf{n}_{\tau=0}$ compresses the level set function along the unit normal vector $\mathbf{n}$, aiming to sharpen the interface. On the other hand, the diffusive term $\nabla \cdot \varepsilon \nabla \phi$ ensures that the characteristic thickness of the profile is proportional to $\varepsilon = 0.5h^{0.9}$, where h is the grid size computed as the cubic root of the cell volume [29].

4.2.2 Surface tension treatment

By implementing an appropriate surface tension model, a twofold goal is sought. First, the calculus of the curvature κ, and second, the application of the pressure jump to the fluid domain. With this aim, a CSF model [54] has been adopted. This technique enables the conversion of the singular term $\sigma\kappa\mathbf{n}\delta_\Gamma$ into a volume force:

$$\sigma\kappa\mathbf{n}\delta_\Gamma = \sigma\kappa\left(\phi\right)\nabla\phi \tag{4.10}$$

where $\kappa\left(\phi\right)$ and $\mathbf{n}$ are given by:

$$\kappa\left(\phi\right) = -\nabla \cdot \mathbf{n} \tag{4.11}$$

$$\mathbf{n} = \frac{\nabla\phi}{\left\|\nabla\phi\right\|} \tag{4.12}$$

Here, $\nabla\phi$ is computed by means of a least-square method [29].

4.3 Numerical solution

The set of equations posed above has been discretized onto a collocated grid arrangement. A finite-volume method has been enforced, according to [29]. The diffusion terms of the governing equations (Eqs. 4.2 and 4.9) are discretized by using a Central Difference (CD) scheme. In addition, a superbee flux limiter for unstructured meshes [29] is applied to the convective term of the advection equation (Eq. 4.8), and a CD scheme is used for the convective term of the momentum equation (Eq. 4.2). For time discretization, a 3-step-third-order accurate TDV Runge-Kutta scheme [55] is enforced in the advection and reinitialization equations (Eqs. 4.8 and 4.9). Finally, both compressive and diffusive terms of the reinitialization equation (Eq. 4.9) are discretized by using a CD scheme [29].

The pressure-velocity coupling is solved by means of a Fractional Step method [29, 56–58]. Momentum equation (Eq. 4.2) is computed in two steps:

$$\frac{\rho \mathbf{v}^{\mathrm{p}} - \rho^n \mathbf{v}^n}{\Delta t} = \nabla \cdot \left[\rho \mathbf{v}^n \left(\mathbf{v}^n - \mathbf{v}^n_{\mathrm{domain}}\right)\right] + \nabla \cdot \mu \left(\nabla \mathbf{v}^n + \nabla^T \mathbf{v}^n\right) + \rho \mathbf{g} + \sigma \kappa \nabla \phi + \Psi_{\mathrm{IB}} \tag{4.13}$$

For the sake of simplicity, this equation has been discretized using an explicit Euler scheme, although an explicit Adams-Bashforth scheme has been used for computations. Superscript "p" refers to predictor variables, n to the current time step, and $n+1$ to the following one. The next step of the method is the calculation of the following expression:

$$\mathbf{v}^{n+1} = \mathbf{v}^{\mathrm{p}} - \frac{\Delta t}{\rho} \nabla p^{n+1} \tag{4.14}$$

By adding the continuity equation (Eq. 4.1), the following Poisson equation is obtained to solve the pressure field:

$$\nabla \cdot \left(\frac{1}{\rho} \nabla p^{n+1}\right) = \frac{1}{\Delta t} \nabla \cdot \mathbf{v}^{\mathrm{p}} \tag{4.15}$$

The discretization of this equation leads to a linear system, which is solved by means of a preconditioned conjugate gradient method. Cell-face velocity is calculated according to [29, 58], in order to avoid pressure-velocity decoupling and to fulfill the incompressible constraint. This cell-face velocity is used to advect the `CLS` function in Eq. 4.8, and momentum in Eq. 4.2.

4.3.1 Mesh movement and boundary conditions

The mesh is moved following the evolution of the bubble/drop. Thus, to an observer standing on the mesh, the bubble/drop will be always around its initial position (although its shape may change). The first consequence of this approach is the need of open boundaries at the domain limits. Consequently, inflow or outflow conditions are imposed at the boundary faces of the fluid domain.

The inflow boundary condition imposes a null velocity vector at the corresponding boundary, and a zero gradient condition for the pressure. The outflow boundary condition is a combination of a convective boundary condition and the formulation proposed by Davis and Moore [59]. The reader is referred to Sec. 2.4 for further notes on the formulation of the outflow boundary condition.

To determine whether a specific boundary face is inflow or outflow, the following dot product is evaluated: $\mathbf{v}_{\mathrm{G}} \cdot \mathbf{n}_{bf}$, where $\mathbf{v}_{\mathrm{G}}$ is the velocity of the bubble/drop centroid G (see App. A), and $\mathbf{n}_{bf}$ is the outward unit normal vector to the boundary face. If the value of this dot product is positive, it means that the bubble/drop is moving towards this face. Thus, the boundary face should be an inflow. Otherwise the boundary face

under consideration is set as outflow. It is worth emphasizing that both conditions inflow/outflow collapse into the same formulation in the limit case where the aforementioned dot product is close to 0 (see Sec. 2.4). It is also worth to mention that in cases with long distances between the bubble/drop centroid and the boundaries (where the fluid velocity near the domain limits is close to zero), the treatment of the inflow and outflow becomes less important, and even free-slip conditions could work well (see e.g. [12]).

Additionally, when an Arbitrary Lagrangian-Eulerian approach is adopted, the mass flux through a face f needs to be modified as follows [36]:

$$\dot{m}_f^{\text{modified}} = \int_{S_f} \rho(\mathbf{v} - \mathbf{v}_S) \cdot \mathbf{n} \mathrm{d}S \approx \rho_f (\mathbf{v} \cdot \mathbf{n})_f S_f - \rho_f (\mathbf{v}_S \cdot \mathbf{n})_f S_f \tag{4.16}$$

where subscript f denotes that the corresponding variable is evaluated at face f, and $\mathbf{v}_S$ is the surface velocity whose outward unit vector is represented by $\mathbf{n}$. Linear interpolation between nodes is used when a certain variable is unknown at a specific face (e.g. for the density ρ). The term $(\mathbf{v}_S \cdot \mathbf{n})_f S_f$ represents the volume swept by the CV face f per unit of time. As no deformation is allowed, the movement of the mesh is a combination of a linear translation and a rotation from the bubble/drop centroid G. Therefore, if the term $\mathbf{v}_S$ is evaluated at the centroid of the face, the error in the calculation of the swept volume is first order accuracy. For some particular cases, it is possible to compute the exact swept volume. See App. B for a detailed derivation on how to compute this volume. The cells volumes remain unchanged due to the nature of the mesh movement, which combined with the accurate calculation of the swept volume ensure the accomplishment of the so-called Space Conservation Law (SCL) [36]:

$$\frac{d}{dt} \int_{\Omega_{\text{CV}}} \mathrm{d}\Omega_{\text{CV}} + \int_S \mathbf{v}_S \cdot \mathbf{n} \mathrm{d}S = 0 \tag{4.17}$$

where Ω_{CV} is the volume of the moving cell, and S is its closed surface. Note that the first term of this equation is strictly zero because Ω_{CV} is constant, and the second term is also zero because it is computed exactly as explained above. Therefore, the SCL is ensured and the mass conservation is procured.

The definition of the translation and rotation of the mesh is not imposed by the physic, but should be coherent with the evolution of the bubble/drop within the domain. Two main scenarios can be identified (see Fig. 4.1):

1. When the bubble/drop is evolving in an unconstrained domain where its trajectory can not be easily predicted in advance. In this case, the linear velocity of the mesh $\mathbf{v}_{\text{domain}}$ is taken equal to the bubble/drop velocity $\mathbf{v}_{\text{G}}$. Additionally, its angular velocity $\boldsymbol{\omega}_{\text{domain}}$ is taken equal to the one that the bubble/drop velocity vector has: $\boldsymbol{\omega}_{\text{domain}} = \frac{\mathrm{d}\alpha}{\mathrm{d}t}$ where α is the angle rotated by the velocity vector of the bubble/drop. The centre of rotation is the bubble/drop centroid G.

2. When the bubble/drop is evolving in a tube or, in general, in a constricting geometry generated by the extrusion of a curve through a driving curve. Note that the extruded curve could vary along the driving curve. The only requirement is that the driving curve should be unequivocally defined. In this case, the linear velocity of the mesh is taken equal to the projection of the bubble/drop velocity onto the driving curve. Consequently, $\mathbf{v}_{\text{domain}} = (\mathbf{v}_{\text{G}} \cdot \hat{\mathbf{n}}_{\mathbf{t}})\hat{\mathbf{n}}_{\mathbf{t}}$, where $\hat{\mathbf{n}}_{\mathbf{t}}$ is the tangent vector of the driving curve at the projection of the centroid of the bubble/drop G onto the driving curve (namely $G^{'}$). In addition, the angular velocity of the domain $\boldsymbol{\omega}_{\text{domain}}$ is equal to the one that the tangent vector $\hat{\mathbf{n}}_{\mathbf{t}}$ of the driving curve has: $\boldsymbol{\omega}_{\text{domain}} = \frac{\mathrm{d}\hat{\mathbf{n}}_{\mathbf{t}}}{\mathrm{d}t}$. The centre of rotation is the point $G^{'}$. Fig. 4.2 sketches this geometrical configuration.

The first approach described above should be able to tackle the second situation. However, the distinction seems desirable in order to get a more natural movement of the mesh in cases with a constricting geometry. It is also intended to avoid an instance where the mesh does not cover the whole cross section of the pipe. See Sec. 4.5.2 for cases with both implementations. Regarding the second scenario, there are some further considerations to be taken into account. The formulation presented above assumes the analytical description of the driving curve as known. In some situations (e.g. in industrial applications) this issue constitutes a limitation, as the tubular geometry of the problem might not be analytically described. In this case, two alternatives are proposed: the use of the general approach for unconstrained geometries, and the calculation of a "predicted" driving curve by interpolation between points of the tubular geometry. An additional problem is establishing the shape and the dimensions of the fluid domain. The longitudinal length is set by the physics of the problem (see Sec. 2.5). However, the lateral distance must be kept as small as possible in order to save resources, but it should be enough to cover the whole transversal section of the tube during the whole simulation. There is no straightforward solution for this issue, although it is analytically approachable for easy geometries (see e.g. the case presented in Sec. 4.5.2).

4.3.2 Immersed boundary treatment

The forcing term Ψ_{IB} in Eq. 4.13 is included to enforce the non-slip immersed boundary condition. It affects the nodes in the vicinity and the interior of the immersed bodies. If the solid moves with respect to the mesh, the nodes are classified at every iteration into three categories: interior, forcing and exterior points (see Fig. 4.3). The interior points are those falling within the immersed body. The forcing points are those outside the solid, which meet one or both of these conditions: (i) the node has a neighbour which is inside the object, (ii) their cell-volume is cut by the immersed boundary. The remaining nodes are the so-called exterior points.

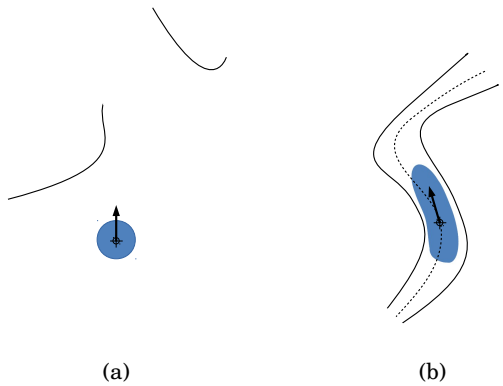

Figure 4.1: Two main scenarios may appear when studying the evolution of bubbles/drops in complex geometries: (a) an unconstrained situation, in which the geometry does not determine beforehand the movement of the bubble/drop; and (b) a constrained situation where a tubular geometry forces the movement of the bubble/-drop following a driving curve.

To classify the nodes, a signed distance field $\varphi(\mathbf{x},t)$ is defined as the minimum distance from the node position to the immersed boundary. In order to be able to handle any geometry, the immersed boundary is represented by an unstructured surface mesh, composed by a series of triangles in stereo-lithography (STL) format [60]. To calculate the minimum distance between a particular node of the mesh to the Immersed Boundary, the closest triangle is found and the closest point of that triangle is computed. Finally, the sign of the distance is defined using the outpointing normal vector of that particular triangle, given positive values for internal nodes and negative for the external ones.

Once the nodes have been classified, the source term is calculated. This source term is zero in the exterior points, and it is evaluated with the following expression for the rest of the nodes [61]:

$$\Psi_{\mathrm{IB}} = \frac{\rho\mathbf{V} - \rho\mathbf{v}^n}{\Delta t} - \left\{\nabla\cdot\left[\rho\mathbf{v}^n\left(\mathbf{v}^n - \mathbf{v}^n_{\mathrm{domain}}\right)\right] + \nabla\cdot\mu\left(\nabla\mathbf{v}^n + \nabla^T\mathbf{v}^n\right) + \rho\mathbf{g} + \sigma\kappa\nabla\phi\right\} \tag{4.18}$$

where $\mathbf{V}$ is the desired value of the velocity field. For a prescribed movement of the body, the velocities V of the interior points are directly calculated from their coordinates. However, in order to compute the velocities of the forcing points, some approx-

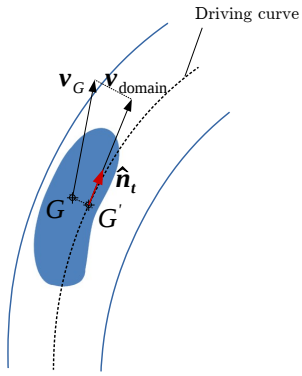

Figure 4.2: Geometrical objects needed to define the mesh movement in problems with a constricting geometry. G is the bubble/drop centroid, $G^{'}$ is its projection onto the driving curve of the pipe, $\mathbf{v}_G$ is the velocity of the bubble/drop centroid, $\hat{\mathbf{n}}_\mathbf{t}$ is the unit tangent vector of the driving curve at $G^{'}$, and $\mathbf{v}_{\text{domain}}$ is the velocity of the computational domain.

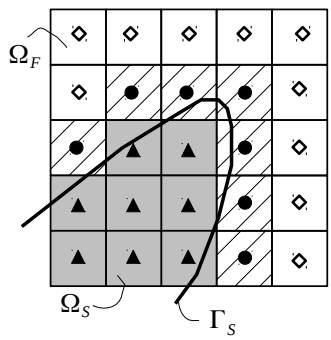

Figure 4.3: Example of the control volumes intersected by an object. (Ω_S) is the solid region, (Ω_F) is the fluid region, and (Γ_S) is the solid-fluid interface. The nodes are classified as: ($\Diamond$) exterior points, ($\bullet$) forcing points, and ($\blacktriangle$) interior points.

imations have to be used, as by definition these nodes are outside the object. In this particular case, $\mathbf{V}$ is computed by means of a second-order interpolation among the local velocity of the solid, and the predictor velocity $\mathbf{v}^{\mathrm{p}}_{\Psi_{\mathrm{IB}}=0}$ of neighbour nodes calculated when $\Psi_{\mathrm{IB}} = 0$. The reader is referred to the work by Favre et al. [61] for further details about the calculation of Ψ_{IB}.

Due to the nature of the fractional step method, in the present formulation of the IB method the boundary condition is imposed to the predictor velocity. Some inaccuracy is introduced in the solution, because the projection step is performed after imposing the non-slip boundary condition. As a result of this procedure, some mass flux may pass through the solid boundaries, which does not affect the accuracy of the solution but can produce unphysical results, e.g. a particular fluid-phase could penetrate into an immersed body. This undesirable effect can be avoided by imposing a boundary condition to the pressure field using a cut-cell based discretization [50, 51] only to the Poisson equation, as in [52]. A cut-cell is a cell with some of its volume at the fluid region and some at the solid region. Two types of cut-cells can be distinguished: those with the node in the fluid region (generally called "regular cut-cells"), and those with the node in the solid (called "small cut-cells", because the fluid fraction of it could be arbitrarily small). Both types of cells are shown in Fig. 4.4.

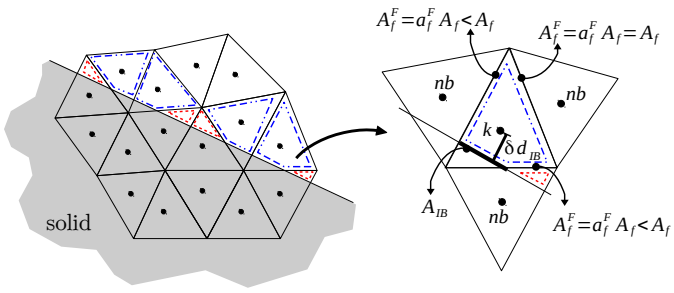

Figure 4.4: Definition of regular cut-cells and small cut-cells. The blue dot-dash lines denote the regular cut-cells, and the red dash lines mark the small cut-cells. Some of the faces of a cut-cell are divided into a fluid-face and a solid-face, where A_f^F represents the surface of the fluid-face. The surface of the solid-fluid interface contained within the cut-cell is indicated here as A_{IB}. Finally, δd_{IB} is the distance between the node of the cut-cell and the solid-fluid interface.

The finite-volume discretization of the Poisson equation for a generic cell k is written as:

$$\dot{m}^{\mathrm{p}}_{\mathrm{IB}} + \sum_{f\in\mathscr{F}(k)} \dot{m}^{\mathrm{p}}_{f} = \Delta t \left((p^{n+1}_{\mathrm{IB}} - p^{n+1}_{k}) \frac{A_{\mathrm{IB}}}{\delta d_{\mathrm{IB}}} + \sum_{f} \left(p^{n+1}_{nb} - p^{n+1}_{k} \right) \frac{a^F_f A_f}{\delta d_f} \right) \tag{4.19}$$

$$\mathbf{v}^{n+1}_{k} = \mathbf{v}^{\mathrm{p}}_{k} - \frac{\Delta t}{\rho \gamma V_k} \left(p^{n+1}_{\mathrm{IB}} \mathbf{n}^F_{\mathrm{IB}} A_{\mathrm{IB}} + \sum_{f} p^{n+1}_{f} \mathbf{n}^F_f a^F_f A_f \right) \tag{4.20}$$

$$\dot{m}^{n+1}_{f} = \dot{m}^{\mathrm{p}}_{f} - \Delta t a^F_f A_f \frac{(p^{n+1}_{\mathrm{IB}} - p^{n+1}_{k})}{\delta d_f} \tag{4.21}$$

where the superscript "p" denotes that the corresponding variable is a "predictor" one, $\mathscr{F}(k)$ is the set of faces of cell k, $a^F_f = A^F_f / A_f$ is the fluid surface fraction of face f and $\gamma = V^F_k / V_k$ is the volume fraction of cell k. The subscript IB refers to the section of the immersed boundary intersected by cell k called ∂IB, A_{IB} is its surface, δd_{IB} is the distance between the node of k and ∂IB, and p_{IB} is the pressure at that location. The subscript nb refer to the face-neighbour of k, and δd_f is the normal-projected distance between the nodes k and nb. Superscript F in the normal vectors $\mathbf{n}^F_{\mathrm{IB}}$ and $\mathbf{n}^F_f$ indicates that those vectors point to the fluid region. For the cells that are not cut by an immersed boundary, all the coefficients a^F_f and γ are equal to 1. Therefore, the discretization corresponds to the classic second-order spectro-consistent scheme [62]

However, small cells are treated with a different approach. As they can be arbitrarily small, the use of the same approach as for the regular cut-cells could lead to an ill-conditioned pressure Poisson equation. Small cut-cells can also cause viscous stability problems. Therefore, the so-called "virtual cell merging technique" is used in the present work. It was first proposed by Meyer et al. [63] for the momentum equation, and adapted by Seo and Mittal [52] for the pressure Poisson equation. It consists of modifying the independent term of the Poisson equation. First, the independent terms $b(k) = \sum_f \dot{m}^P_f$ are computed for every cell, including the small ones. Thus, the term b_{small} of each small cell is transferred to its regular neighbours. This means that the term b_{nb} of each regular neighbour is incremented by a fraction of b_{small}. Given a small cell, the fraction of b_{small} which is transferred to each regular neighbour is proportional to the fluid surface shared with that neighbour. Once this transfer is done, the independent terms of the Poisson equation corresponding to the small cells become zero. The reader is referred to [64] for a detailed study of the `IB` implementation.

4.3.3 Time step

In order to obtain a suitable time step at each iteration, a `CFL` condition is enforced. Therefore, the following condition is obtained by comparison of the different terms of

the momentum equation (Eq. 4.2):

$$\Delta t = \mathscr{C}_{\mathrm{CFL}} \cdot \min\left(\frac{h}{\|\mathbf{v}^n\|}, \frac{h^2 \rho^n}{\mu^n}, \sqrt{\frac{h}{g}}, \left(\frac{\rho_1 + \rho_2}{4\pi\sigma}\right)^{1/2} h^{3/2}, \frac{h}{\|\mathbf{v}_{\mathrm{domain}}\|} \right) \tag{4.22}$$

where $\mathscr{C}_{\mathrm{CFL}}$ is a safety constant ($\mathscr{C}_{\mathrm{CFL}} \approx 0.1$). It is worth noting that the source term from the immersed boundary method (namely, Ψ_{IB}) does not additionally restrict the time step. At this point, the effect of the embedded body has already been taken into account in the calculus of the velocity field. Therefore, the convective restriction (first term of the left-hand part of Eq. 4.22) already includes the effect of the IB method on the time step.

4.3.4 Calculation algorithm

Alg. 1 summarizes the calculation procedure needed to advance from the current time step t^m to the next one t^{m+1}. This procedure has been implemented in a parallel in-house c++/MPI code called *TermoFluids* [65].

Algorithm 1 CLS+MM+IB method

repeat:
- Compute Δt (Sec. 4.3.1)
- Advect ϕ (Eq. 4.8)
- Reinitialize ϕ (Eq. 4.9)
- Update ρ, μ, κ and $\mathbf{n}$ (Eqs. 4.6, 4.7, 4.11 and 4.12)
- Evaluate Ψ_{IB} (Sec. 4.3.2)
- Compute $\mathbf{v}^{\mathrm{p}}$ (Eq. 4.13)
- Solve the Poisson equation to obtain p (Eq. 4.15)
- Compute the velocity at the faces [29]

} Fractional step method

- Calculate the $\mathbf{v}_{\mathrm{domain}}$ (Sec. 4.3.1)
- Move the mesh
- Update mass flow by imposing the SCL (Eq. 4.16)

} Mesh movement

- Move the solid (if needed)

until $t > t_{\mathrm{end}}$

4.4 Discussion on the method

The proposed approach exploits some striking features of the comprising methods. First, the CLS method allows dealing with multiphase domains, while keeping the mass

error under control [29]. Second, the dynamic mesh technique enables using small computational domains, covering only the important regions of the problem (see. Ch. 2). Finally, using an IB method leads to representing intricate solids which do not conform the mesh shape (see Sec. 4.3.2). Furthermore, the synergy among those methods brings additional benefits:

- It is possible to reproduce internal boundaries (i.e. solid and free-slip conditions) in an ALE framework working with open boundaries.
- Long temporal evolutions can be studied with no need of increasing the size of the mesh, e.g. problems involving infinity domains (i.e. tubes).
- The mesh quality is homogenised, regardless of the geometry. That avoids the worsening of the mesh quality due to the potential need of reproducing certain intricate geometries.
- The method greatly facilitates on-the-go testing and parametric studies. This is because, in general, a modification of the geometry or flow conditions does not imply a change of the mesh.
- Since the bubble/drop stays steady at a specific location within the computational domain, the mesh can be improved by refining the important regions of the problem (e.g. the interface between fluids). This notably complements the increased versatility achieved by working in a full unstructured framework. In general terms the global benefit is similar to the one obtained by using an adaptive mesh refinement technique.
- By using the proposed CLS+MM+IB method, the obtained solution of a specific multiphase problem conserves the mass, as all of the consisting methods are mass-conservative (i.e. CLS method [29], ALE methodology [36], and the IB method explained in Sec.4.3.2).
- The method allows to modify geometrical conditions during the simulation. This is particularly useful when studying the impact of bubbles/drops against objects. In the analysis of these problems, terminal conditions in the motion of the bubble/drop are usually assumed. With the proposed method, by placing the solids out of the fluid domain, free motion conditions are initially applied to the motion of the drop/bubble. When this drop/bubble achieves its steady state, the solid is positioned in the appropriate place. Otherwise, the initial distance from the bubble/drop centroid to the solid could not be enough to achieve the terminal velocity, or it could be excessive entailing unnecessary computational expenditure.

There are also some few drawbacks to keep in mind when considering the proposed method:

- The CLS+MM+IB method does not easily deal with multiple bubbles/drops problems, or cases involving break-up. Complications arise in defining the mesh movement, as it is specified based on the velocity of a bubble/drop centroid (see Sec. 4.3.1). This criterion becomes obsolete in cases with multiple bubbles/drops, and it should be revised. Cases with large deformations could also be problematic, since the drop/bubble might get too close to a domain boundary.

- The boundary condition design becomes troublesome due to the inherent presence of open limits. Both the formulation of these boundaries and their placement within the domain require a careful treatment. See Ch. 2 for a detailed discussion on this issue.

- When dealing with constricting geometries, a minimum domain is desirable (although not essential) in order to save computational resources. The domain dimensions should assure that the computational domain covers the whole transversal section of the pipe throughout the complete simulation. However, the sizing of this minimum domain is not straightforward. See Sec. 4.3.1 for further notes on this topic.

4.5 Results and validation

In the present section, some studies are conducted in order to assert the validity and accurateness of the proposed CLS+MM+IB method presented above. First, in order to capture the particular potentialities of the method, we designed one pair of two-dimensional experiments, which involve complex geometries, mesh translation and mesh rotation. Reference results are obtained by running the same case within a static mesh, and without employing immersed boundaries. This last approach is the usual way to proceed when facing multiphase DNS problems. In these reference cases, although the mesh resolution is kept constant, the fluid domain is the same as the physical domain. Therefore, much bigger meshes are needed. By proceeding this way, the particularities of the presented method can be successfully evaluated in comparison with the general approach for multiphase DNS in complex geometries, providing a consistent way to make measurable comparisons. In addition, a clear discussion on the simulation times and the resource consumption can be drawn. After these cases, three three-dimensional problems are presented. By doing so, it is intended to validate the proposed method in full 3D configurations. In these cases, the obtained results are compared with those found in the literature.

4.5.1 Two-dimensional gravity-driven bubble approaching an inclined plane

In this section, we propose the study of the passage of a bouncing bubble through a highly-inclined plane. This case is very convenient to accomplish the goals of the present section, due to the following reasons. First, it involves a clear-cut rotating process which allows the evaluation of the rotational mesh mechanism. Second, the well-defined boundary treatment and the fact that the flow regime has been extensively studied [66] allow us to focus attention on the phenomenology of the bubble-wall interaction. Finally, it is affordable to simulate the same problem with the complete domain, without moving the mesh or using immersed boundaries. This is very useful for the sake of comparison, as differences in the obtained results can be attributed exclusively to particularities of the proposed CLS+MM+IB method. This comparison technique has been broadly used in CFD, e.g. when validating a new LES formulation against a DNS case.

Therefore, the problem has been solved by using two methods: a traditional approach, with the complete domain and ordinary boundaries, and the CLS+MM+IB method. Fig. 4.5 sketches the geometrical configuration and initial set up of both cases, showing the distances from the bubble to the boundaries. It is worth noting that an increased left lateral distance is needed for the case of moving mesh, as the bubble could move beyond the initial left distance to the wall after bouncing (and in fact it does). Distances from the bubble to the inflow and outflow when solving the problem with the proposed CLS+MM+IB method are overestimated in comparison with those obtained with the method proposed in Ch. 2. Thus, a smaller domain would actually be capable of capturing the physics involved in the problem. However, with the aim of minimizing the discrepancies among methods caused by this reason, bigger distances were chosen. Physical properties are determined by the following dimensionless numbers:

$$\eta_\rho = \frac{\rho_1}{\rho_2} \quad , \quad \eta_\mu = \frac{\mu_1}{\mu_2} \quad , \quad Eo = \frac{g d^2 \left(\rho_1 - \rho_2\right)}{\sigma} \quad , \quad Mo = \frac{g \mu_1^4 \left(\rho_1 - \rho_2\right)}{\rho_1^2 \sigma^3} \tag{4.23}$$

where d is the initial bubble diameter, and η_ρ and η_μ are the density and viscosity ratios, respectively. Eo is the Eötvös number and Mo is the Morton number. In the present problem, $\eta_\rho = 10$, $\eta_\mu = 10$, $Eo = 9.0$ and $Mo = 6{\cdot}10^{-4}$. This flow regime coincides with that of the well-known benchmark case first studied in [66].

In both methodologies, the employed meshes are full unstructured and composed of triangular control volumes. In order to ensure the mesh independence of the obtained results, several cell sizes h are tested. In particular, three different meshes are used for both the case with full domain and the one with moving mesh. The chosen resolutions are $d/15$, $d/23$ and $d/30$. Therefore, the meshes are labelled from M1 to M3 in increasing order of resolution, adding the subscript "FD" for the full domain case, and "MM" for the moving mesh case.

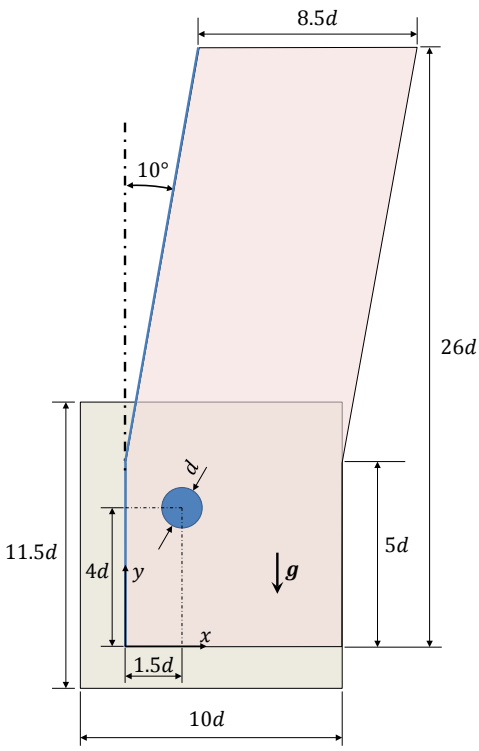

Figure 4.5: Outline of the initial set-up of the problem of a bubble bouncing through a highly-inclined plane. Simulation domains are highlighted in shaded boxes for both the complete domain case and the one with the moving mesh.

Two integral quantities are chosen to assess the aforementioned mesh resolutions. The first one is the average dimensionless velocity in the sliding state $\left\|\mathbf{v}^*_{\text{sliding}}\right\| = \left\|\mathbf{v}_{\text{sliding}}\right\|/\sqrt{dg}$, which is computed from the moment when the bubble starts interacting with the wall. This moment is determined as the point where the lateral velocity $\mathbf{v}_{\text{bubble},x}$ ceases to be negligible compared to the vertical one $\mathbf{v}_{\text{bubble},y}$: $\mathbf{v}_{\text{bubble},x}/\mathbf{v}_{\text{bubble},y} > 0.05$, which happens at dimensionless time $t^* = t\sqrt{g/d}$ approximately equal to 1.8. Furthermore, the variation of the bubble shape is evaluated in terms of the circularity ζ_{2D}, which compares a perfect circular bubble against the actual one (see App. A for details on how to compute it). The value of the average circularity in the sliding stage (defined as explained above) is denoted by $\zeta_{2D,\text{sliding}}$. Tab. 4.2 summarizes these integral val-

ues for the different tested resolutions. It shows that the mesh convergence has been already achieved for meshes labelled as M2. Therefore, a resolution of $h = d/23$ seems enough to accurately reproduce the physics of the problem.

Furthermore, the proposed CLS+MM+IB method presents also a good performance concerning the mass conservation. By using this method, the obtained final mass error E_{V} for the meshes $M1$, $M2$ and $M3$ is respectively $1.12 \cdot 10^{-11}$, $6.64 \cdot 10^{-12}$ and $5.78 \cdot 10^{-12}$. Finally, the convergence rate has been computed by using the results of the sliding velocity shown in Tab. 4.2. Result of the finer mesh has been taken as reference value. Therefore, the obtained value of the convergence rate is 1.23.

Case	Mesh	$\left\lVert \mathbf{v}^*_{\mathrm{sliding}} \right\rVert$	$\zeta_{2D,\mathrm{sliding}}$	$E_{\left\lVert \mathbf{v}^*_{\mathrm{sliding}} \right\rVert}$	$E_{\zeta_{2D,\mathrm{sliding}}}$
Full domain	$\mathtt{M1}_{\mathrm{FD}}$ ($h = d/15$)	0.5413	0.8580	2.64%	1.89%
	$\mathtt{M2}_{\mathrm{FD}}$ ($h = d/23$)	0.5519	0.8452	0.74%	0.37%
	$\mathtt{M3}_{\mathrm{FD}}$ ($h = d/30$)	0.5560	0.8421	–	–
CLS+MM+IB	$\mathtt{M1}_{\mathrm{MM}}$ ($h = d/15$)	0.5488	0.8580	2.20%	2.13%
	$\mathtt{M2}_{\mathrm{MM}}$ ($h = d/23$)	0.5398	0.8470	0.52%	0.82%
	$\mathtt{M3}_{\mathrm{MM}}$ ($h = d/30$)	0.5370	0.8401	–	–

Table 4.2: Integral results and mesh independence study for the problem of the passage of a bouncing bubble through a highly-inclined plane. Here h is the characteristic cell size, $\left\lVert \mathbf{v}^*_{\mathrm{sliding}} \right\rVert$ is the absolute value of the sliding velocity, $\zeta_{2D,\mathrm{sliding}}$ is average circularity in the sliding stage, $E_{\left\lVert \mathbf{v}^*_{\mathrm{sliding}} \right\rVert}$ is the relative error of the absolute value of the sliding velocity referred to the case with denser mesh, and $E_{\zeta_{2D,\mathrm{sliding}}}$ is analogously the relative error of the average circularity in the sliding stage.

Further results are presented below, comparing those of M3 meshes. First, the evolutions of the dimensionless velocity components $v^*_y = v_{\mathrm{bubble},y}/\sqrt{dg}$ and $v^*_x = v_{\mathrm{bubble},x}/\sqrt{dg}$ are presented in Fig. 4.6a and 4.6b, respectively. In these figures, it is clearly shown the oscillatory nature of the velocity evolution. The bubble speeds up from rest with almost null lateral velocity, until it starts interacting with the solid. In this bouncing stage, its velocity fluctuates around an average value remaining fairly constant with a very light increase. This oscillatory trend is also observed in the evolution of the dimensionless minimum distance from bubble centroid to the left wall $d^*_{\mathrm{min}} = d_{\mathrm{min}}/d$, which is plotted in Fig. 4.6c. This figure shows that the first stage of the bubble ascent is characterized by a slight increase in the distance to the wall. This is caused by the constriction effect of the left lateral wall, that tends to expel the bubble. After this period, this distance drops sharply. Finally, the evolution of the circularity ζ_{2D} is plotted in Fig. 4.6d, showing a clear fluctuating pattern around 0.85 approximately. All these plots show that the proposed CLS+MM+IB method provides reasonably good agreement

in comparison with the reference data.

Finally, a comparison between profiles evolution is presented in Fig. 4.7, together with the bubble trajectory. This image highlights once more the oscillatory nature of the bubble path. During the bouncing stage, the bubble loses its symmetry, and it alternatively elongates towards right and left. Again, CLS+MM+IB method yields nearly indistinguishable results from the reference method.

The very small deviations between the results of both methods arise for three reasons. First, the mesh rotation makes the lateral distance from bubble centroid to the right boundary to vary slightly along the simulation, causing small disturbances in the velocity field. Second, the used open boundaries in the CLS+MM+IB method may also affect the far field. And third, the treatment of the IB and MM methods intrinsically introduce a small numerical error in the obtained results [36].

The great advantage of the proposed CLS+MM+IB method is the resources consumption savings. Tab. 4.3 summarizes some performance data to give an idea of those savings. In particular, simulation times are much lower compared with the case with a complete mesh (approximately one third). Furthermore, it is worth noting that the longer the simulation is, the more notable these differences are.

Mesh label	$t_{\mathrm{sim,MM}}/t_{\mathrm{sim,FD}}$	$N_{\mathrm{MM}}/N_{\mathrm{FD}}$
M1	0.58	0.53
M2	0.55	0.49
M3	0.53	0.46

Table 4.3: Resources consumption comparison of the problem of a bubble approaching a highly-inclined plane. Here, the results of the proposed CLS+MM+IB method are compared against those obtained by using a standard approach with the complete domain. $t_{\mathrm{sim,MM}}/t_{\mathrm{sim,FD}}$ represents the ratio between simulation times and $N_{\mathrm{MM}}/N_{\mathrm{FD}}$ the ratio between total mesh sizes.

4.5.2 Two-dimensional gravity-driven Taylor bubble through a curved channel

In the present section, the 2D problem of an elongated bubble rising in a curved channel is addressed. The channel whereby the bubble evolves has a curved part connecting two straight sections: a vertical one and an inclined one. This case is particularly convenient to validate the rotating mesh process in constricting geometries (see Sec. 4.3.1). Therefore, the mesh does not exactly follow the motion of the bubble, but slides over the driving curve of the pipe. The results of the proposed CLS+MM+IB method are compared against a numerical simulation run using the complete domain, i.e. without immersed boundaries and moving mesh. As was stated in the section above, this way of compar-

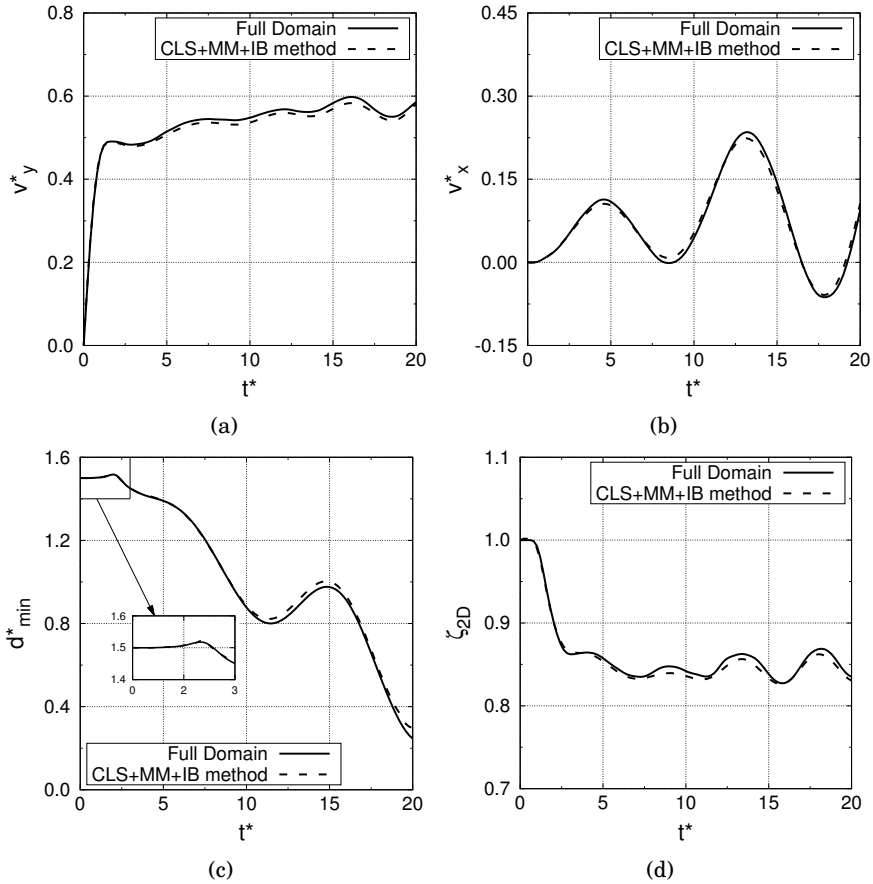

Figure 4.6: Result of the 2D problem of a bubble approaching an inclined plane. The graphs show (a) the vertical dimensionless velocity $v_y^* = v_{\text{bubble},y}/\sqrt{dg}$ (b) the lateral dimensionless velocity $v_x^* = v_{\text{bubble},x}/\sqrt{dg}$, (c) the dimensionless minimum distance $d_{\text{min}}^* = d_{\text{min}}/d$ from the bubble centroid to the wall, and (d) circularity ζ_{2D}. Those magnitudes are plotted against dimensionless time $t^* = t\sqrt{g/d}$, for the mesh resolution $h = d/30$ (meshes $\texttt{M3}_{\text{FD}}$ and $\texttt{M3}_{\text{MM}}$).

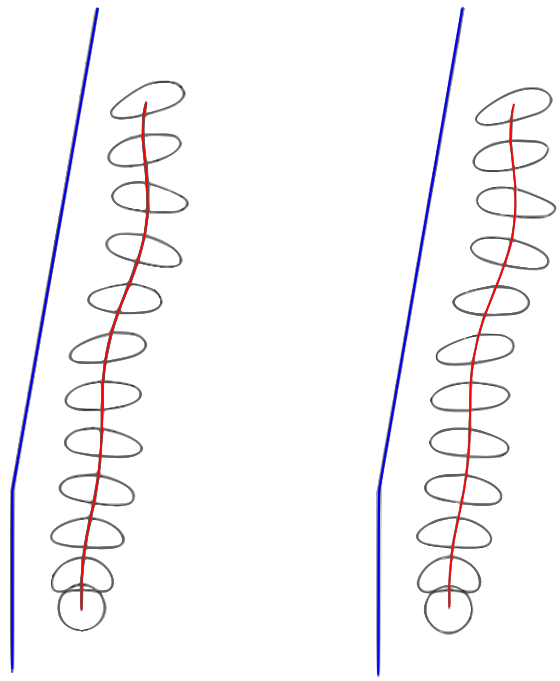

(a) (b)

Figure 4.7: Profiles evolution in the problem of a bubble approaching a highly-inclined plane, for (a) the full domain case and (b) the CLS+MM+IB case. Successive profiles are plotted each 1.85 dimensionless time units.

ing models provides a clear process to discern the deviations caused by the use of a moving mesh and an immersed boundary method.

Fig. 4.8 sketches the initial setting up of the numerical experiment, as well as the mesh dimensions for both cases. As shown in this figure, the initial shape of the bubble is a two-dimensional cylinder with two hemispheres. The diameter d of the initial bubble is equal to $0.8D$, where D is the diameter of the pipe. The length of the initial bubble is $1.1534D$, giving rise to an equivalent total volume equal to $\pi D^2/4$. The mesh width in the proposed CLS+MM+IB method is equal to the diameter of the pipe D plus a value e given by:

$$e = \left(R_\Upsilon - \frac{d}{2}\right) - \sqrt{\left(R_\Upsilon - \frac{d}{2}\right)^2 - h_i^2} \approx 0.292D \tag{4.24}$$

where $R_\Upsilon = 4.5D$ is the turning radius of the driving curve, and $h_i = 1.5D$ is the chosen distance from the bubble centroid to the inlet. This assures that the mesh is able to cover the whole transversal section of the pipe during its ascent. Eq. 4.24 is a particular expression for circular turns, and it should be expressly revised in any other case. See Sec. 4.3.1 for further notes on the calculus of this distance. Additionally, distances from bubble centroid to inlet and outlet are set based on the indications given in Sec. 2.5.

Different mesh resolutions are tested in both the case with the complete domain, and the case with moving mesh. Thus, three different meshes are used in each case, namely from `M1` to `M3` in order of increasing resolution. These meshes are unstructured and composed of triangular control volumes. The chosen resolutions are $D/50$, $D/75$, $D/100$.

For this problem, dimensionless numbers characterizing the flow regime are defined as follows:

$$\eta_\rho = \frac{\rho_1}{\rho_2} \quad , \quad \eta_\mu = \frac{\mu_1}{\mu_2} \quad , \quad Eo = \frac{gD^2\rho_1}{\sigma} \quad , \quad Mo = \frac{g\mu_1^4}{\rho_1\sigma^3} \tag{4.25}$$

Here $\eta_\rho = 756.02$, $\eta_\mu = 4597.70$, $Eo = 100.0$ and $Mo = 0.015$. Note that the definition of those dimensionless numbers differs from the one given in Eq. 4.23 for the previous problem. The chosen slug flow regime has been broadly studied, starting from the original work by Bugg and Sad [67].

Some integral magnitudes are shown in Tab. 4.4 in order to assert the adequateness of the different meshes tested. Two integral values are shown in that table. On the one hand, the dimensionless sliding velocity $\left\|\mathbf{v}^*_{\text{sliding}}\right\| = \left\|\mathbf{v}_{\text{sliding}}\right\|/\sqrt{Dg}$ is presented for the different mesh resolutions. This value is obtained by averaging the dimensionless bubble velocity during the inclined ascent, i.e from dimensionless time $t^* = t\sqrt{g/D}$ approximately equal to 12.6. On the other hand, the shape of the bubble is evaluated in terms of the deformation parameter $\Delta = (L-B)/(L+B)$ in the sloping part of the ascent, where L is the length of the bubble from nose to tail, and B is its average transversal length. The results comparison shows that $h = D/75$ seems a reasonable resolution to accurate reproduce the ascent of the Taylor bubble.

By using the CLS+MM+IB method, the mass error E_V is kept under control. For the meshes $M1$, $M2$ and $M3$, the obtained values of this magnitude at the end of the simulation are respectively $8.72 \cdot 10^{-13}$, $2.78 \cdot 10^{-13}$ and $1.33 \cdot 10^{-13}$.

Additional results of the current problem are shown in Fig. 4.9, for `M3` meshes. First, the vertical component of the dimensionless velocity $v^*_y = v_{\text{bubble},y}/\sqrt{Dg}$ is plotted against dimensionless time $t^* = t\sqrt{g/D}$. This magnitude rises from zero to a terminal value, which is slightly modified due to the change of the channel inclination. On the other hand, the evolution of the lateral dimensionless velocity $v^*_x = v_{\text{bubble},x}/\sqrt{Dg}$ shows a similar behaviour. It presents two clearly distinct sections: one before the pipe elbow, and another one after the pipe elbow. In the first one, this velocity component is close to zero. In the passage of the bubble through the elbow, an adaptation region

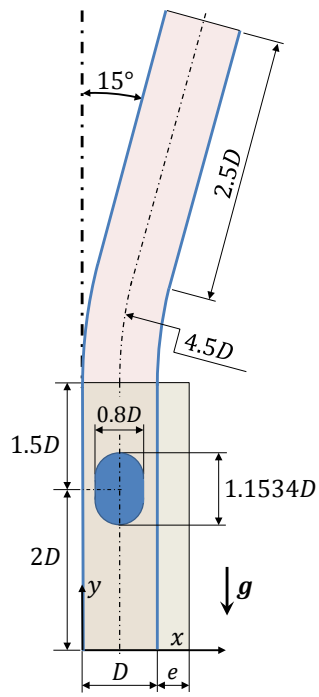

Figure 4.8: Outline of the initial set-up of the problem of a Taylor bubble evolving in a curved channel. The initial length of the bubble is set to $1.1534D$ in order to get a 2D volume of the bubble equal to $\pi D^2/4$. Simulation domains are highlighted in shaded boxes for both the complete domain case and the one with the moving mesh. The mesh width in the moving mesh case is equal to $D + e$, where $e \approx 0.292D$.

is identified. Here, $v_x^* = v_{\text{bubble},x}/\sqrt{Dg}$ rises and eventually stabilizes in the inclined zone. Both methods provide very close results.

Finally, Fig. 4.10 sketches the profiles evolution for both methods. In the corresponding image of the proposed `CLS+MM+IB` method, the positions of the mesh at each time instant are also represented. The figure shows the well-defined rotation process of the mesh, following the driving curve of the channel. All of these results suggest that the `CLS+MM+IB` method is certainly capable of reproducing the physics of the problem with enough level of accuracy. Small differences are explained in terms of the presence

Case	Mesh	$\lvert\mathbf{v}_{\text{sliding}}\rvert$	Δ	$E_{\lvert\mathbf{v}_{\text{sliding}}\rvert}$	E_Δ
Full domain	$\texttt{M1}_{\text{FD}}$ ($h = D/50$)	0.2104	0.2646	0.32%	4.74%
	$\texttt{M2}_{\text{FD}}$ ($h = D/75$)	0.2109	0.2722	0.10%	2.02%
	$\texttt{M3}_{\text{FD}}$ ($h = D/100$)	0.2111	0.2778	–	–
CLS+MM+IB	$\texttt{M1}_{\text{MM}}$ ($h = D/50$)	0.2014	0.2528	1.93%	5.72%
	$\texttt{M2}_{\text{MM}}$ ($h = D/75$)	0.2025	0.2590	1.41%	3.39%
	$\texttt{M3}_{\text{MM}}$ ($h = D/100$)	0.2053	0.2682	–	–

Table 4.4: Integral results and mesh independence study of the problem of a Taylor bubble rising in a pipe with a change in its inclination. Here h is the characteristic cell size, $\lvert\mathbf{v}_{\text{sliding}}\rvert$ is the absolute value of the sliding velocity (in the inclined section), Δ is the deformation parameter at the sloping part, $E_{\lvert\mathbf{v}_{\text{sliding}}\rvert}$ is the relative error of the absolute value of the sliding velocity referred to the case with denser mesh, and E_Δ is analogously the relative error of the deformation parameter at the inclined section.

of open boundaries and numerical issues (e.g. the meshes, although sharing the same resolution, are not identical).

In a reference to the resource consumption comparison, the proposed CLS+MM+IB method performs much better than a traditional DNS approach with a complete domain. Tab. 4.5 presents a comparison among simulation times and mesh sizes. Note that if the physical domain were bigger, those savings would be much more notable.

Mesh label	$t_{\text{sim,MM}}/t_{\text{sim,FD}}$	$N_{\text{MM}}/N_{\text{FD}}$
M1	0.67	0.65
M2	0.65	0.61
M3	0.59	0.56

Table 4.5: Resources consumption comparison of the problem of a Taylor bubble turning in a curved pipe. Results of the proposed CLS+MM+IB method are compared against those obtained by using a standard DNS approach with the complete domain. $t_{\text{sim,MM}}/t_{\text{sim,FD}}$ represents the ratio between simulation times and $N_{\text{MM}}/N_{\text{FD}}$ the ratio between total mesh sizes.

4.5.3 Three-dimensional gravity-driven falling drop against a plane surface

The problem of a drop falling against a plane is addressed in the present section. As reference case, we chose one of the cases studied by Han and Tryggvason [68]. In particular, the one corresponding with the following dimensionless numbers (see Eq. 4.23):

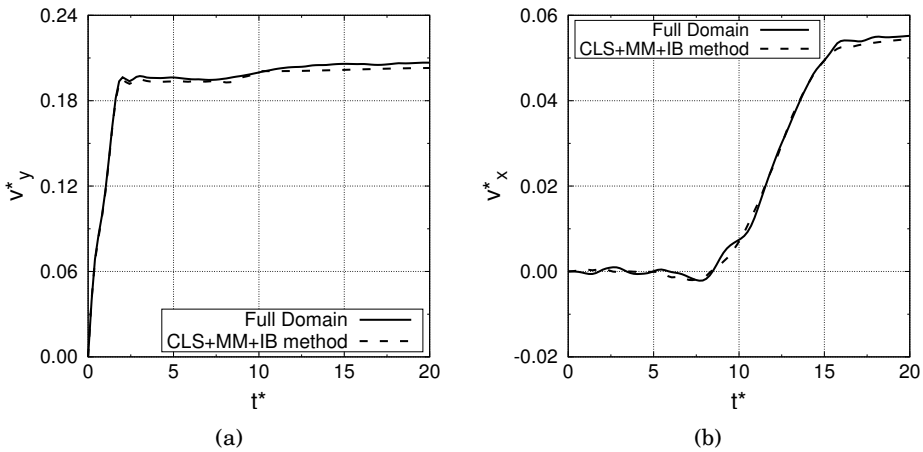

Figure 4.9: Result of the 2D problem of a Taylor bubble turning in a curved pipe. The graphs show (a) the vertical dimensionless velocity $v_y^* = v_{\text{bubble},y}/\sqrt{Dg}$ (b) the lateral dimensionless velocity $v_x^* = v_{\text{bubble},x}/\sqrt{Dg}$. Those magnitudes are plotted against dimensionless time $t^* = t\sqrt{g/D}$, for the mesh resolution $h = d/100$ (meshes $\texttt{M3}_{\text{FD}}$ and $\texttt{M3}_{\text{MM}}$).

$\eta_\rho = 1.15$, $\eta_\mu = 1.0$, $Eo = 12.0$, and $Oh_d = 0.0466$, where $Oh_d = \mu_2/\sqrt{\rho_2 d\sigma}$ is the Ohnesorge number, and d is the initial droplet diameter. These parameters give rise to a very homogeneous flow regime, with a slow and straight movement of the drop. We chose this simple regime in order to simplify the study case in this first approach to a three-dimensional problem.

A sketch of the initial arrangement is presented in Fig. 4.11. The initial shape of the drop is a sphere with diameter d. The initial distance from the drop center to the solid is set to $12d$. We used that value since, based on previous studies available in the literature [13], it is enough in order to assure that the drop achieves its steady state before interacting with the solid. The lateral distance from the drop centroid to the lateral boundaries is fixed to $5d$, since it gives rise to enough accurate results, as studied in [69]. The values of the distances from the drop to the inlet $h_i = 2.9$ and to outlet $h_o = 5.1$ are founded on a compromise between domain size and disturbance of the solution due to the proximity of the boundaries to the drop. See Sec. 2.5 for further notes about the setting of these magnitudes.

We used an unstructured mesh composed by tetrahedral control volumes. The drop will stay steady at its initial position. Therefore, we designed a mesh with a dense core of radius equal to d, and a radial exponential growing in the size of the control volumes (see Fig. 4.11b). A mesh independence study is included in the results description,

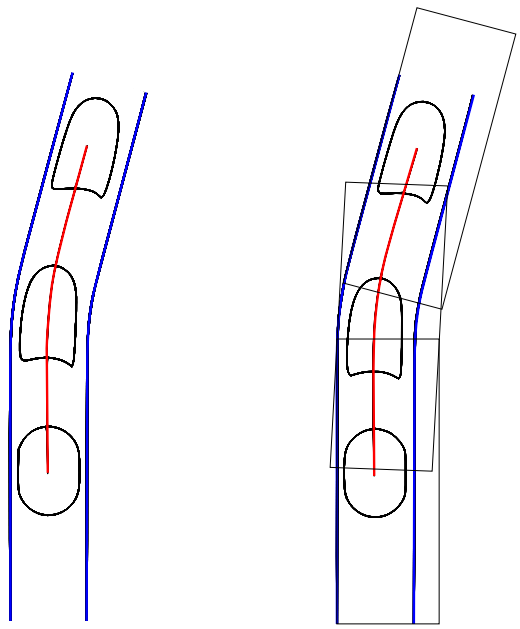

(a) (b)

Figure 4.10: Profiles evolution in the problem of a Taylor bubble turning in a curved pipe. Results correspond to (a) the full domain case and (b) the `CLS+MM+IB` one. Successive profiles are plotted at 0, 11.9 and 20 dimensionless time units.

where the meshes presented in Tab. 4.6 are used.

Results of the problem are summarized below. First, a comparison of the dimensionless terminal velocity $U_T^* = U_T/\sqrt{dg}$ and the deformation parameter $\Delta = (L-B)/(L+B)$ at the falling state is presented in Tab. 4.7, where L is the average length of the bubble and B is its average width. Good agreements were found in those results, specially for the finer mesh `M3`, with errors of less than 5% in both magnitudes in comparison with reference data [68]. Furthermore, Fig. 4.12a shows the time evolution of the dimensionless velocity in comparison with the reference data [68]. It can be seen from this figure that the proposed method properly capture the time in which the drop achieves to the solid (at a dimensionless time $t^* = t\sqrt{g/D}$ of around 45).

The time evolution of the vertical distance from the drop center to the plane surface is plotted in Fig. 4.12b. The last part of this evolution reveals that the the mesh `M3` is

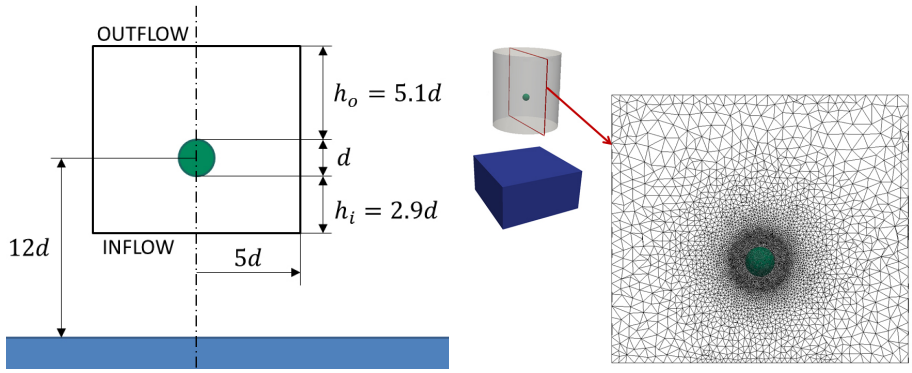

(a) (b)

Figure 4.11: Initial arrangement and mesh configuration for the Gravity-Driven falling drop problem.

.

Mesh name	Mesh size	$h_{\min}$	$h_{\max}$
M1	$1.4 \cdot 10^5$	$d/10$	$1.5d$
M2	$4.1 \cdot 10^5$	$d/16$	d
M3	$9.1 \cdot 10^5$	$d/22$	$0.8d$

Table 4.6: Description of the meshes used in the Gravity-Driven falling drop problem, where $h_{\min}$ is the cell size in the core of the mesh and $h_{\max}$ is the maximum cell size.

the sole one capable to maintain a constant distance from the drop interface to the wall. This shows that the coarser meshes do not properly capture the interaction of the bubble with the plane, even though the falling behaviour is accurately reproduced.

The mass conservation is evaluated in Tab. 4.8 by means of the percentage change in the drop volume. This table shows that, in that sense, the proposed CLS+MM+IB method behaves better than other methods available in the literature. This may be attributed to the smaller numerical errors of the CLS method, to a proper design and placement of the open boundaries, and to a better resolution in the regions of interests. Note also that the references use axisymmetric solvers.

Streamlines and vorticity fields are plotted in Figs. 4.13 and 4.14b, obtained by using the results from M3 mesh. First, Fig. 4.13a shows the streamlines and the vorticity field in a plane perpendicular to the surface toward which the bubble heads for. A single vortex is observed in the wake of the bubble, close to the bubble interface.

Case	U_T^*	Δ	$E_{U_T^*}$	E_Δ
Present work (M1)	0.2958	0.4466	2.38%	13.03%
Present work (M2)	0.3029	0.4677	0.03%	8.92%
Present work (M3)	0.2983	0.4885	1.56%	4.87%
Muradoglu and Kayaalp [13]	0.306	—	1.00%	—
Han and Tryggvason [68]	0.303	0.5135	—	—

Table 4.7: Summary of achieved results at the falling steady state ($t^* = 35.0$), where $U_T^* = U_T/\sqrt{dg}$ is the dimensionless terminal velocity, Δ is the deformation parameter, $E_{U_T^*}$ is the relative error of the dimensionless terminal velocity referred to the results of [68], and E_Δ is analogously the relative error of the deformation parameter.

Case	E_{Ω_2}
Present work (M1)	$3.24 \cdot 10^{-6}$%
Present work (M2)	$8.99 \cdot 10^{-7}$%
Present work (M3)	$1.70 \cdot 10^{-7}$%
Muradoglu and Kayaalp [13]	1.2%
Han and Tryggvason [68]	0.4%

Table 4.8: Comparison of the percentage of change in the drop volume Ω_2 by means of its relative error E_{Ω_2}, showing that the proposed method presents lower errors than reference data.

Fig. 4.13b shows that this vortex moves upwards and losses intensity when the bubble is closest to the solid. Additionally, two low-intensity counter-rotating vortices appears on the periphery of the bubble. Figs. 4.14a and 4.14b show the streamlines and vorticity fields in a plane parallel to the floor, through the center of the bubble. Both graphs highlight the fact that the problem is intrinsically axisymmetric. Moreover, a clear pattern of low-intensity counter-rotating vortices can be observed in the vicinities of the interface, for both states.

Finally, the profiles evolution is presented in Fig. 4.15 in comparison with the reference data [68]. Those profiles were obtained by using the mesh M3. As can be observed in that graph, results from the present method qualitatively match the reference results. Note also that, for the mesh M1, the implicit axisymmetric of the problem is not properly reproduced, and results do not seem enough accurate in terms of the instantaneous shapes of the drop.

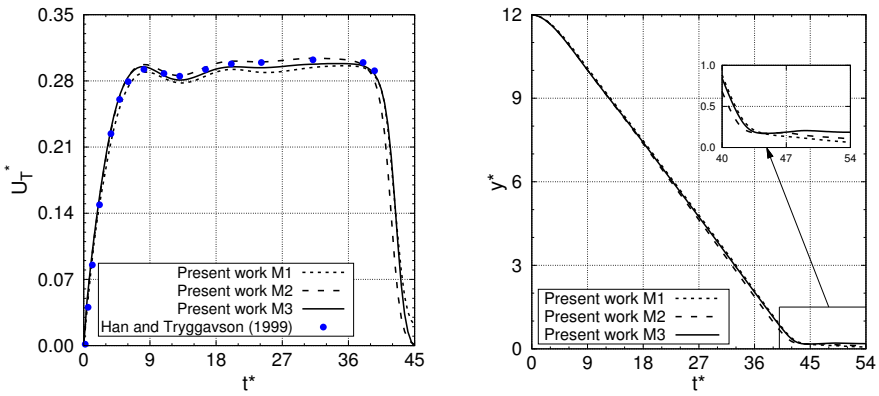

(a) (b)

Figure 4.12: Falling drop problem results for the tested method. The graphs show (a) dimensionless terminal velocity U_T^* and (b) axial coordinate from the solid $y^* = y/d$ over dimensionless time $t^* = t\sqrt{g/d}$, for the different mesh resolutions tested.

4.5.4 Three-dimensional gravity-driven buoyant drop in a constricted circular channel

In the present section, we analyze the motion and evolution of a drop as it passes through a periodically constricted pipe. The proposed `CLS+MM+IB` method is enforced to tackle this problem in a full three-dimensional domain. Some of the advantages of the proposed method are clearly highlighted in this problem. First, a three-dimensional approach is only computationally affordable by using a domain optimization method, i.e. the moving mesh technique in this case. Any method involving the complete 3D domain would be prohibitive in terms of the `DNS`, as the physical domain needs to be very long to collect average data in the periodic motion of the drop. Additionally, the use of an immersed boundary method allows a simple mesh generation process, as well as facilitates parametric studies or geometrical modifications (e.g. in the wavelength or amplitude of the constrictions). A classical approach would have required a complete re-meshing process when varying the original conditions, while the present methodology would just need a redefinition of the surface mesh (STL) of the solid, with no changes in the fluid mesh.

Numerical data of Olgac et al. [17] is taken as reference, which in turn is based on the experimental work of Hemmat and Borhan [4]. On the basis of these references, the set-up sketched in Fig. 4.16 is used in the present study. The pipe is trivially generated by radial extrusion of a sinusoidal curve. Therefore, the wavelength λ is set to $4D$,

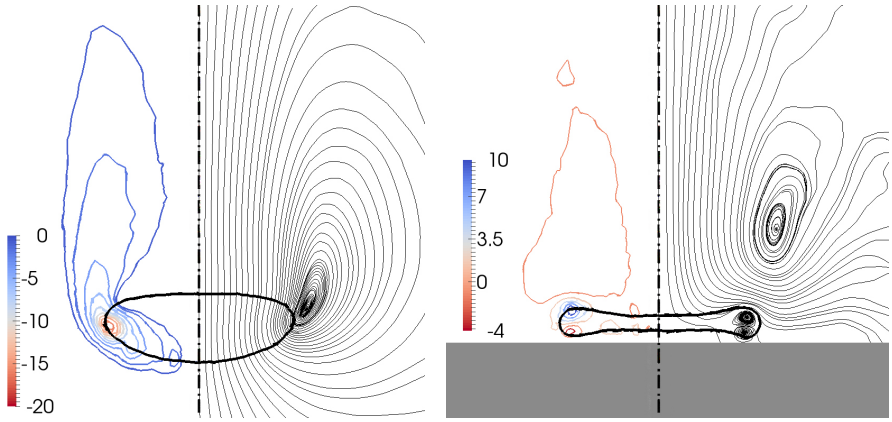

(a) (b)

Figure 4.13: Streamlines and vorticity field (s^{-1}) in XY plane (a) in the steady falling state ($t^* \approx 31.0$) and (b) when the drop is closest to the solid ($t^* = 44.85$)

.

where D is the average pipe diameter, and the amplitude A is set to $0.07D$. The drop initial axial position is chosen to be at the point of maximum tube diameter $D+2A$. A drop dimensionless diameter is defined as $k = d/D$, where d is its dimensional diameter. In this experiment, k is set to 0.78. Distances from drop centroid to inlet ($1.8D$) and outlet ($2.2D$) are chosen considering the notes given in Sec. 2.5. Those distances assure that the presence of the open boundaries does not disturb the motion of the drop.

The simulation domain is cylindrical, with a diameter equal to $D+2A$. This size guarantees that the mesh covers the whole transversal section of the solid throughout the ascent. This domain has been meshed using unstructured triangular prisms. The meshes have been generated by a constant step extrusion of a two-dimensional grid along the cylinder axis, being h the step size, and also the characteristic size of the triangular elements of the extruded grid. Three different meshes have been considered, labelled from `M1` to `M3` in increasing order of mesh resolution h. This resolution has been set by dividing the pipe average diameter D into 22, 30 and 39, respectively. See Tab. 4.9 for a complete description of these meshes. The simulation domain is moved following the ascent of the drop as explained in Sec. 4.3.1. Nevertheless, for this particular case the procedure explained in that section for constricting geometries collapses in a linear translation, due to the intrinsic axisymmetric of the problem.

The flow regime is characterized by the dimensionless numbers given in Eq. 4.25. Therefore, $\eta_\rho = 1.200$, $\eta_\mu = 0.7565$, $Eo = 270.9$ and $Mo = 6.539$. These flow conditions

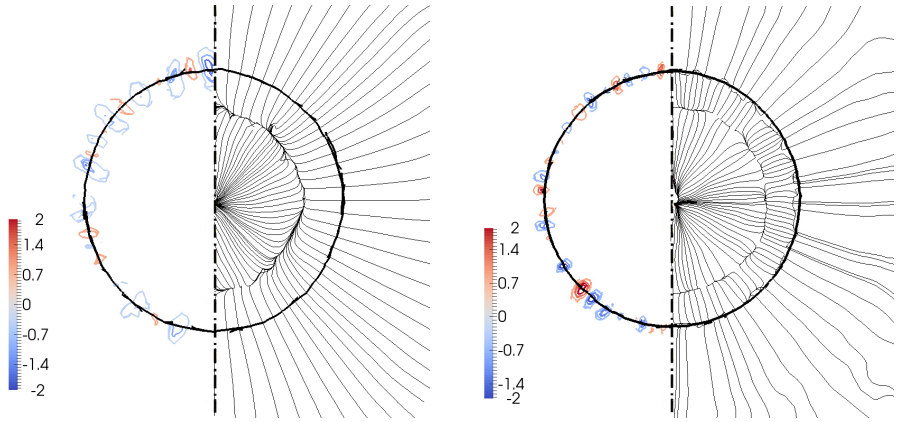

(a) (b)

Figure 4.14: Streamlines and vorticity field (s^{-1}) in XZ plane (a) in the steady falling state ($t^* \approx 31.0$) and (b) when the drop is closest to the solid ($t^* = 44.85$)

.

are obtained when using a two-phase system composed by Diethylene glycol-glycerol ($63.8wt\%$) as suspending fluid and $UCON-285$ as drop fluid [17]. It corresponds to the system labeled as DEGG12 of the references [4, 17].

Results are expressed in terms of dimensionless quantities. Time and velocities are made dimensionless using the following reference values, respectively:

$$t_{\text{ref}} = \frac{2\mu_1}{(\rho_1 - \rho_2)gD} \quad ; \quad \text{v}_{\text{ref}} = \frac{(\rho_1 - \rho_2)gD^2}{4\mu_1} \tag{4.26}$$

For distances, $\lambda = 4D$ is taken as reference magnitude.

The average dimensionless terminal velocity of the drop $\left|\bar{\mathbf{v}}^*_{\text{drop}}\right|$ has been taken as reference value to measure the accurateness of a specific simulation. Tab. 4.10 shows the value of this magnitude for the different meshes tested, as well as a comparison against reference data. Additionally, mass error E_{V} is kept under control for the three tested meshes ($M1$, $M2$ and $M3$). The obtained values for this magnitude at the end of the simulation are respectively $6.83 \cdot 10^{-8}$, $2.44 \cdot 10^{-8}$ and $4.74 \cdot 10^{-9}$.

Further outcomes of the current study are presented in subsequent figures. First, a comparison among profile shapes are presented in Fig. 4.17[1]. In this figure, results form the present work are compared with those by Olgac et al. [17] and Hemmat and

[1]Right column of Fig. 4.17 was reprinted from Chemical Engineering Communications, 148-150, M.

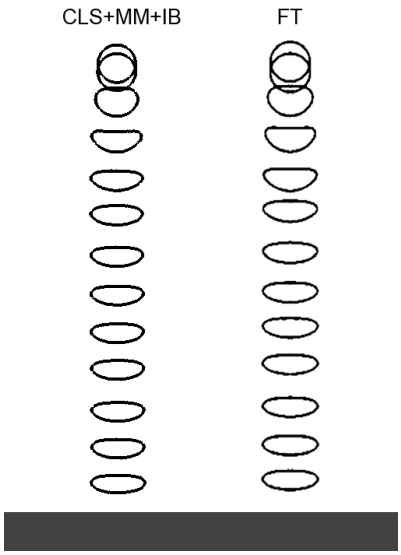

Figure 4.15: Comparison of the evolution of drop profiles of the present work (mesh M3) against results of [68] obtained by using a Front-Tracking method. The gap between successive drop profiles represents the distance the drop falls at a fixed time interval, and the last time instant corresponds with $t^* = 38.30$. Note that, for the reference results, some intermediate profiles were suppressed from those punished in [68], in order to make the evolution coherent with the chosen vertical initial position.

Borhan [4]. Those profiles are plotted when the drop is in its periodical steady state, and when it is passing through the minimum transversal section of the pipe (throat) and the maximum one (expansion). The snapshots are qualitatively in good agreement with the reference data. Slight disagreements are explained based on the ambiguity of locating the drop at a specific axial position, as the profile shape notably changes in a very tight range.

Time evolutions of the dimensionless velocity $\mathbf{v}^*_{\text{drop}}$ and risen distance y^* are depicted in Fig. 4.18 for the different tested meshes. A well-defined oscillatory behaviour is observed in the rising steady state. The drop speeds up during the expansion passage, and slows down while approaching the throat. The mesh convergence behaviour is clearly seen in these graphs. Additionally, Fig. 4.19 sketches some geometrical mag-

Hemmat and A. Borhan, *Buoyancy-driven motion of drops and bubbles in periodically constricted capillary*,

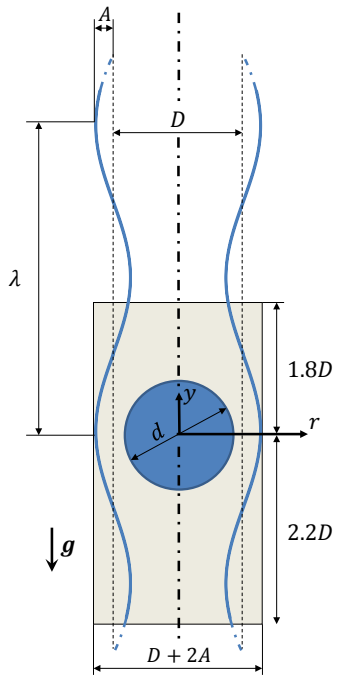

Figure 4.16: Initial set-up of the problem of a drop rising in a periodically constricted circular channel. Here, D is the average pipe diameter, d is the initial drop diameter, λ is the wavelength of the corrugations and A is their amplitude. The shaded grey box represents the simulation domain.

nitudes throughout a single period of corrugation, in comparison with reference data of [4]. Note that there is a discrepancy in the reference for the dimensionless drop diameter k. In [4] this parameter is set to $k = 0.73$, and the chosen one in the present work is $k = 0.78$. The dimensionless distance $\hat{y}^*$ indicates the axial position of the advancing drop meniscus, varying from 0 to 1 (from a specific throat to the next). In Fig. 4.19, the deformation parameter Δ determines the ratio of the perimeter of the deformed drop profile to that of the equivalent spherical drop. Additionally, the dimensionless drop length L^* is defined as the maximum axial drop distance. Those magnitudes were

p. 371, Copyright 1996, with permission from Taylor & Francis.

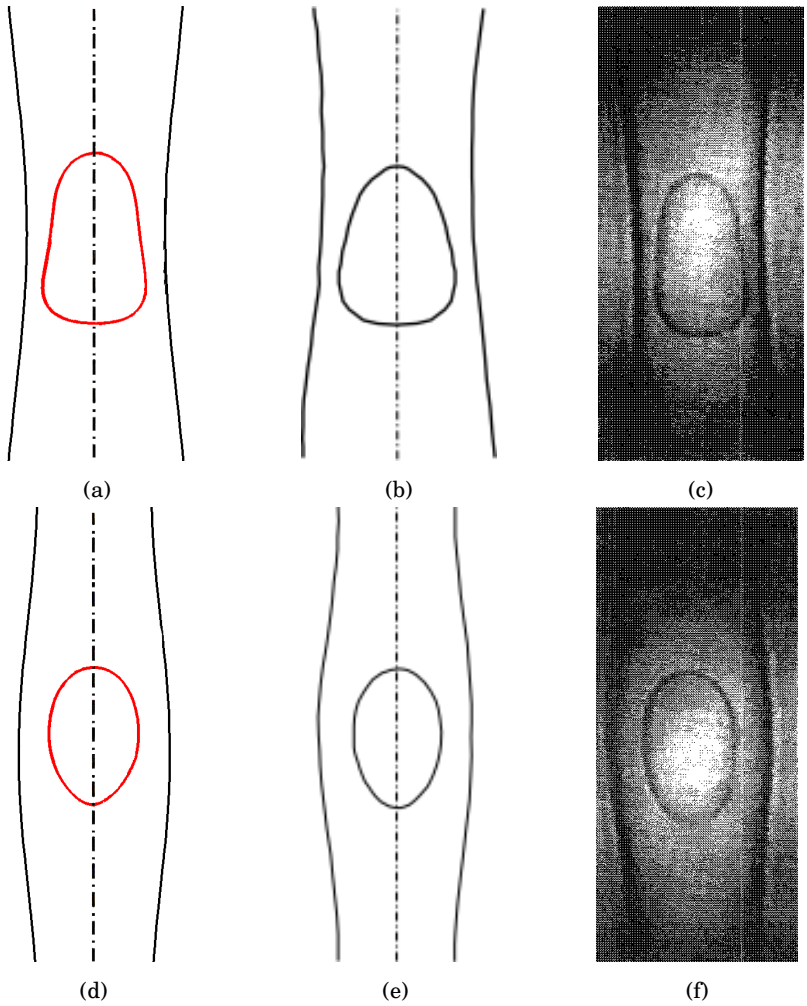

Figure 4.17: Comparison of the profile shapes among different results. Graphs (a) and (d) correspond to the present work, (b) and (e) to Olgac et al. [17], and (c) and (f) to Hemmat and Borhan [4] [1]. The snapshots of the first row correspond to the moment when the drop is passing through the channel throat, and those of the second row correspond to the moment when the drop is located at the expansion section.

Mesh label	Mesh size	Cells per plane	N_{planes}	h
M1	$1.1 \cdot 10^5$	1290	84	$D/22$
M2	$3.9 \cdot 10^5$	2744	132	$D/33$
M3	$5.9 \cdot 10^5$	3872	156	$D/39$

Table 4.9: Description of the meshes used in the problem of a drop passing through a periodically constricted pipe, where N_{planes} is the number of planes in which the vertical axis is divided.

Results	$\left\lvert \bar{\mathbf{v}}^*_{\text{drop}} \right\rvert$	$E_{\left\lvert \bar{\mathbf{v}}^*_{\text{drop}} \right\rvert}$
Present work M1	$6.686 \cdot 10^{-3}$	26.07%
Present work M2	$7.832 \cdot 10^{-3}$	13.40%
Present work M3	$8.558 \cdot 10^{-3}$	5.37%
Olgac et al. [17]	$9.648 \cdot 10^{-3}$	6.68%
Hemmat and Borhan [4]	$9.044 \cdot 10^{-3}$	–

Table 4.10: Integral results of the problem of a drop rising through a periodically constricted channel, in comparison with reference data [4, 17]. $\left\lvert \bar{\mathbf{v}}^*_{\text{drop}} \right\rvert$ is the average dimensionless terminal velocity of the drop, and $E_{\left\lvert \bar{\mathbf{v}}^*_{\text{drop}} \right\rvert}$ is the relative error associated with that magnitude, in comparison with the reported results of Hemmat and Borhan [4].

found to be periodic in the steady ascent of the drop. Despite the aforementioned discrepancy in the dimensionless drop diameter k, results are in reasonable agreement with those of [4], and overall trends are very well represented.

Furthermore, Fig. 4.20 depicts the streamlines and the vorticity field in a plane containing the y-axis of the corrugated channel. In that figure, four states of the periodic steady motion of the drop are presented: the drop passing through the throat, passing through the expansion, and the upward and downward intermediate states. When the drop is at the throat, it presents an elongated mushroom shape (Fig. 4.20a) with a vortex at the rear end of the drop, close to the point of minimum distance between the drop interface and the wall. As the drop rises and expands, the drop tail becomes narrower, acquiring a bullet shape (Fig. 4.20b). Likewise, the vortex shifts towards the nose of the rising drop. This vortex reaches maximum intensity in the expansion (Fig. 4.20c), where the drop shape becomes elliptical. Finally, at the early stage of the constriction (Fig. 4.20d), the drop tail begins to widen, and the vortex recovers its initial position at the rear end of the drop.

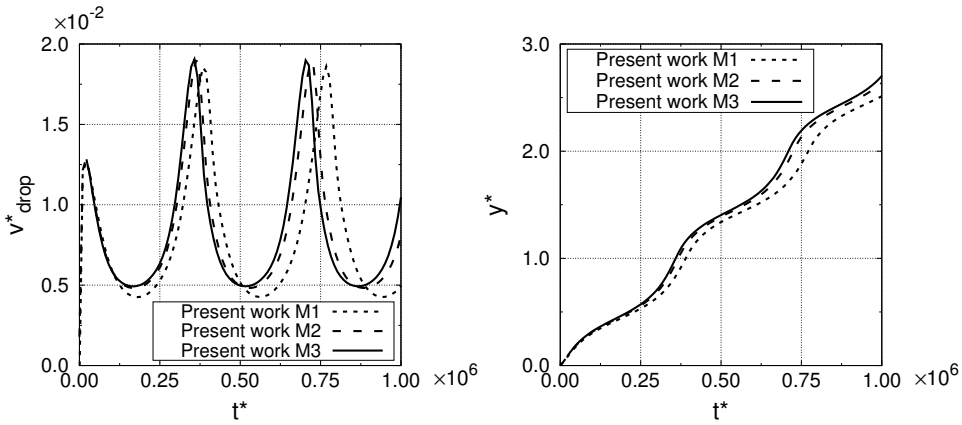

(a) (b)

Figure 4.18: Evolution of (a) dimensionless drop velocity and (b) dimensionless axial position of the centroid of the drop, against dimensionless time t^*, for the three different meshes tested in the present work.

4.5.5 Three-dimensional gravity-driven unconstrained drop impinging on a horizontal plane

The last problem considered to validate the proposed CLS+MM+IB method is the 3D approach of a drop against a horizontal rigid plane. The study of this problem is relevant in fields as mineral flotation, sprays or cooling of nuclear reactors. It constitutes a very interesting problem to solve with the proposed methodology, as some of the main advantages discussed in Sec. 4.4 are plainly shown here. The experimental work by Klaseboer et al. [8] is taken as reference. In this paper, twelve flow conditions are tested, studying the trajectory of the drop when approaching the plane at its terminal velocity. We chose one of those experiments, and we simulated it by using the outlined CLS+MM+IB methodology.

By using the proposed method, only a small computational domain around the drop is taken. Initially, the drop is at rest, and the horizontal solid is placed far away from the drop, outside of the simulation domain. When the drop achieves its steady state, the solid is suddenly moved at the upper limit of the computational domain. This procedure constitutes a major improvement in comparison with other DNS approaches to this problem. With the proposed CLS+MM+IB method, the distance which the drop travels before impinging on the wall is unimportant, as it can be dynamically set during the simulation. This feature facilitates the carrying out of parametric studies, and the easy modification of the flow conditions (e.g. the inclination of the solid or its geometry).

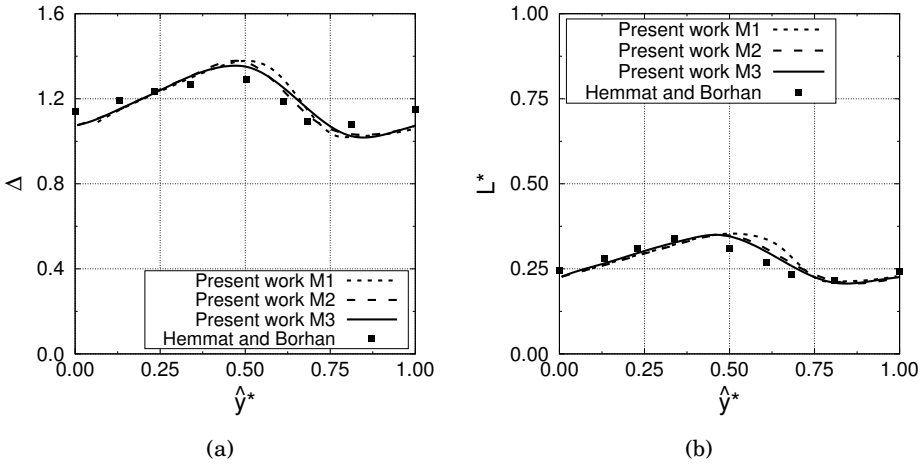

Figure 4.19: Evolution of (a) deformation parameter Δ, and (b) dimensionless length L^* throughout a single period of corrugation for the different mesh resolutions tested in the present work. Results are compared against those by Hemmat and Borhan [4]. The position of the drop is controlled by the dimensionless distance $\hat{y}^*$, which indicates the axial position of the advancing drop meniscus.

The initial arrangement of the problem is sketched in Fig. 4.21, and the mesh configuration is shown in Fig. 4.22. Initially, the drop is spherical-shaped with a diameter equal to d. The initial distance from the drop to the plane y_{plane} is set to a high value (e.g. $y_{\text{plane}} = 100d$). The plane is suddenly moved from that position to the upper limit of the domain at the moment when the drop achieves its terminal state. The motion of the drop within the domain is unbounded until the interaction with the plane starts. In order to assure this condition, distances form the bubble to the boundaries are chosen based on the notes given in Sec. 2.5. By doing this, we aim to find a compromise between domain size and disturbance of the solution.

Flow regime has been set by choosing the following dimensionless numbers (see Eq. 4.23): $\eta_\rho = 1.1547$, $\eta_\mu = 1.6949$, $Eo = 0.1502$ and $Mo = 3.066 \cdot 10^{-11}$. This flow regime corresponds to the system labeled as 1 in the work of Klaseboer et al. [8].

The employed meshes are fully unstructured and composed by tetrahedral control volumes. The location of the drop will remain steady within the simulation domain, as the mesh is moved following its ascent. This behaviour can be exploited during the mesh design process. Therefore, the used meshes have a dense core of a diameter equal to d around the initial position of the drop, with a characteristic cell size of h_{min}. A radial exponential growth is imposed over the cell sizes, reaching the maximum value h_{max} at the borders (see Fig. 4.22). Tab. 4.11 summarizes the meshes employed in the

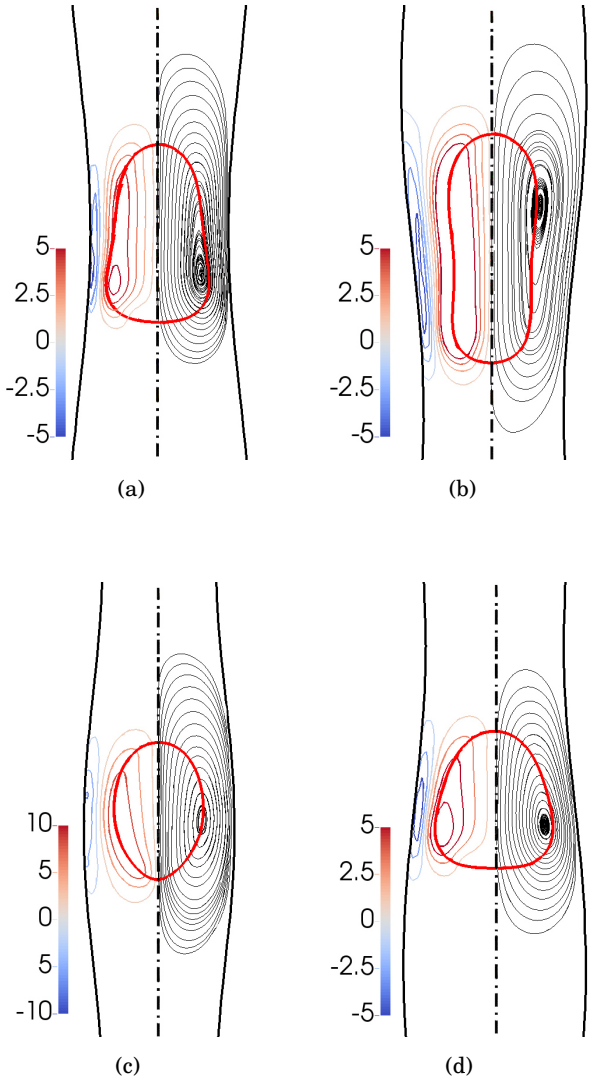

Figure 4.20: Streamlines and vorticity field (s^{-1}) in a plane containing the y-axis of the channel. Different instants are obtained through the periodic steady motion of the drop, at (a) the throat, (c) the expansion, and (b) and (d) the upward and downward intermediate points.

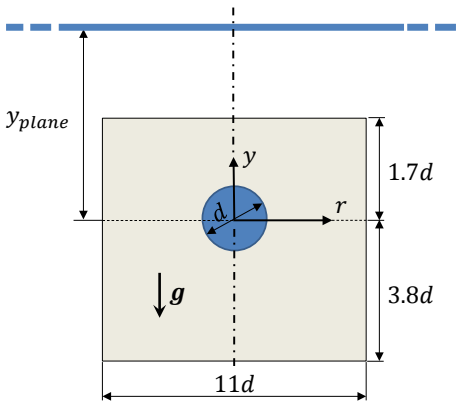

Figure 4.21: Initial arrangement of the problem of a drop impinging on an immersed horizontal wall. d is the drop initial diameter and y_{plane} is the initial distance from drop centroid to the solid plane.

present study. Those meshes are obtained by varying h_{min} and h_{max} sizes.

Mesh label	Mesh size	h_{min}	h_{max}
M1	$5.5 \cdot 10^5$	$d/25$	$d/3$
M2	$9.0 \cdot 10^5$	$d/35$	$d/4$
M3	$1.8 \cdot 10^6$	$d/45$	$d/5$

Table 4.11: Description of the meshes used in the problem of a drop impinging on a horizontal plane, where h_{min} and h_{max} are the minimum and the maximum cell sizes, respectively.

Velocities are made dimensionless by means of the reference value $\sqrt{dg}$. For the time, the reference magnitude is $\sqrt{g/d}$. Finally, distances are made dimensionless by using the initial drop diamiter d as reference value.

The dimensionless terminal distance d^*_{final} from drop centroid to the wall at the final steady point has been taken as the reference integral result to assert the mesh independence. Tab. 4.12 shows a comparison of the obtained results.

Further results are presented in subsequent figures. Fig. 4.23 shows the time evolution of some magnitudes of the problem. First, the dimensionless distance d^* from the drop centroid to the plate has been represented against dimensionless time t^* (Fig. 4.23a). Results include those obtained with the three tested meshes, as well as

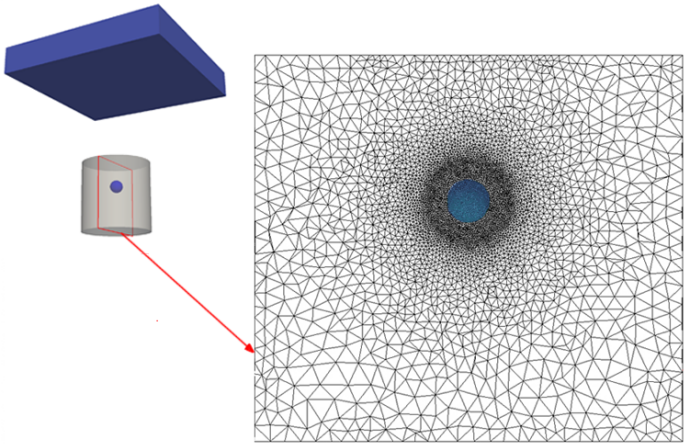

Figure 4.22: Mesh configuration of the problem of a drop impinging on an immersed horizontal wall.

Results	d^*_{final}	$E_{d^*_{\text{final}}}$
Present work M1	0.4645	4.05%
Present work M2	0.4694	3.02%
Present work M3	0.4841	–

Table 4.12: Integral results for the problem of a drop rising and impacting against a solid horizontal plane. The magnitude d^*_{final} represents the dimensionless terminal distance from drop centroid to the wall, and $E_{d^*_{\text{final}}}$ is the relative error associated with this distance, in comparison with the results obtained by using the finer mesh.

those of Klaseboer et al. [8]. Present results are in good agreement with the reference data. When studying the impact of drops/bubbles against obstacles, the mass conservation error becomes a paramount concern. This is because the immersed boundary method should work properly when acting together with the chosen interface tracking technique. To evaluate this issue, Fig. 4.23b represents the evolution of the mass error E_V, defined as the relative error of the volume of the drop V_2 in comparison with the initial one (see App. A). This error remains on the order of 10^{-8} throughout the simulation (which is a considerable small value).

Finally, some snapshots of the impinging process have been plotted in Fig. 4.24. The velocity and the pressure fields are represented over successive time instants from the moment when the drop achieves its terminal velocity. In the rising state, the drop is roughly spherical (Fig. 4.24a). The velocity of the drop remains almost unaltered

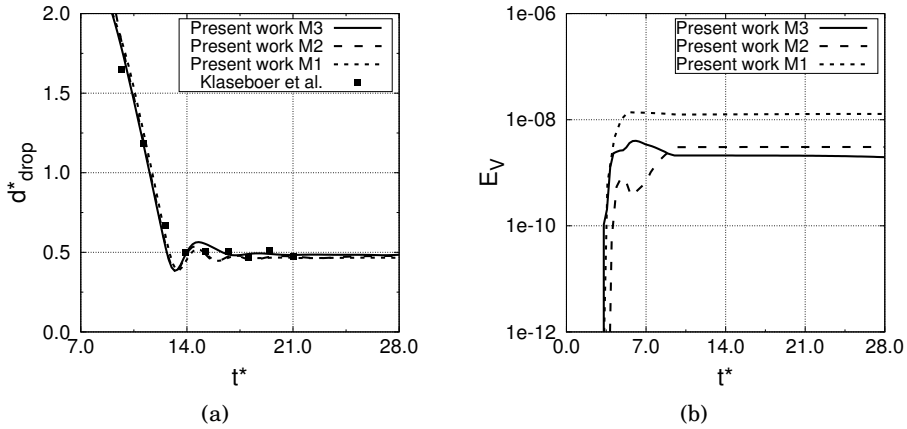

Figure 4.23: Evolution of (a) dimensionless distance from the drop centroid to the plate and (b) mass error, against dimensionless time t^*, for the three different meshes tested in the present work. Results are compared against those of Klaseboer et al. [8].

at the time instant represented in Fig. 4.24b, without noticing the presence of the plate. This reveals that the effect of the immersed wall becomes evident only when the distance from the drop centroid to the wall is very small. The drop lightly tends to acquire an oval shape from the moment where it starts interacting with the wall. The velocity of the drop is dramatically reduced when the drop reaches the wall (Fig. 4.24c), and eventually changes its direction (Figs. 4.24d and 4.24e). At the final stage of the simulation, the velocity of the drop remains close to zero, slightly hovering around this value (Fig. 4.24f). It is worth noting that the obtained velocity fields are not exactly axisymmetric, causing small lateral deviations. This issue stresses the importance of using a full 3D approach to overcome this problem.

4.6 Conclusions

In the present chapter, a coupling between a conservative level set (CLS), a moving mesh (MM) and an immersed boundary (IB) methods has been proposed to address problems of drops and bubbles evolving in complex geometries. First, the CLS method assures a correct representation of the multiphase domain, while the mass error is kept under control [29]. Second, the Arbitrary Lagrangian-Eulerian formulation (i.e. the dynamic mesh) constitutes a robust domain optimization method for bubbles/drops

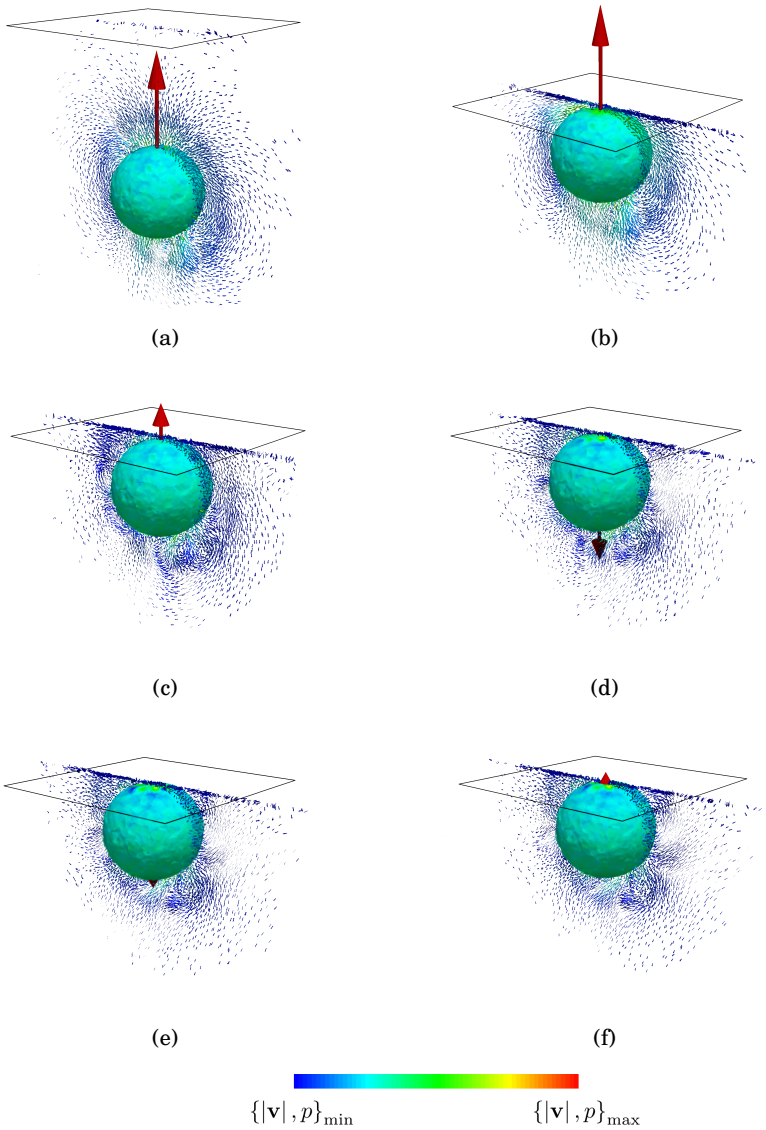

Figure 4.24: Velocity field and pressure field at different time instants. The pressure field is plotted over the drop surface, and the velocity field is represented in a plane containing the vertical axis. The first image is plotted when the terminal velocity is achieved. Successive images are plotted each $t^* \approx 3.1$. The velocity of the centroid of the drop is also represented with a red arrow (not to scale). In these plots, the size of the plate has been reduced to fit the images.

problems, as shown in previous chapters. It allows the use of a small domain covering only the important regions of the problem, i.e. the current position of the drop/bubble and its surroundings. Otherwise very long domains may be needed in order to leave enough space for the bubble/drop to evolve. Finally, geometrical challenges can be addressed by using the IB method, which constitutes a versatile and robust method to represent intricate solids which do not conform the grid shape.

The proposed method presents some synergetic advantages for the study of bubbles/drops. First, the mesh design process is greatly improved. The control volume sizes are homogenised, and the mesh can be refined at the important regions of the problem as the bubble/drop remains steady within the domain. Moreover, the method greatly facilitates conducting parametric studies, due to the fact that in general there is no need to modify the mesh when a slight variation in the geometry is applied. The IB method also allows to represent solid boundaries within a moving domain. This would otherwise be impossible due to the inherent need of open boundaries (i.e. inflow and outflow) in the moving mesh approach. Finally, it is worth noticing that the use of a framework which supports full unstructured meshes increases the applicability of these features.

Results of the validation cases confirmed the aforementioned ideas. First, a couple of 2D cases were studied in order to be able to compare the results with the same case run with a complete domain. By doing this, differences in the obtained results can be attributed solely to the particularities of the proposed CLS+MM+IB method. Those results indicate a reasonable agreement, with slight differences mainly caused by the presence of the open boundaries in the proposed method. Result comparisons for 3D cases yield a good level of agreement between reference results (mostly experimental) and the ones in the presented method. Apart from the accurateness tests, the result section highlights some important features of the method. First, the differences between simulating a drop/bubble through a non-constricting geometry (cases in Secs. 4.5.1, 4.5.3 and 4.5.5), and through a constricting one (cases in Secs. 4.5.2 and 4.5.4). In particular, the rotational mesh process is clearly illustrated in the problems solved in Secs. 4.5.1 and 4.5.2. The capability of solving long physical domains with sort computational domains is plainly stressed in the problem presented in Sec. 4.5.4. In this case study, the average results were computed after a significant elapsed computational time. The improvement of the design mesh process is well represented in the problems studied in Sec. 4.5.3 and 4.5.5. The region of the bubble/drop and its surroundings are meshed with a high resolution, whereas the regions far from the bubble/drop are coarse-meshed. This adaptability is highlighted throughout all these cases. For example, a change in the inclination of the oblique paths of the problems presented in Secs. 4.5.1 and 4.5.2 would only require a simple deformation of the solid. No change in the mesh or code is needed. The versatility of the method also comes into relief when studying the problem presented in Sec. 4.5.5. In this case study, a rising

drop is impacting with an object (a plate). With a classical approach, the distance from the initial drop position to the solid would be a paramount magnitude. It should be reasonably long to assure that the drop reaches the plate at its steady state, but also as short as possible in order to save computational resources. This problem is avoided by using the proposed `CLS+MM+IB` approach. In this case, the drop starts rising freely, and when it is provided that it has achieved its steady motion, the plate is placed at the computational domain limit.

References

[1] S. Haase, Characterization of gas-liquid two-phase flow in minichannels with co-flowing fluid injection inside the channel, part II: gas bubble and liquid slug lengths, film thickness, and void fraction within Taylor flow, Int. J. Multiph. Flow. 88 (2017) 251-269.

[2] H.A. Stone, A.D. Stroock, A. Ajdari, Engineering flows in small devices: microfluidics toward lab-on-a-chip. Ann. Rev. Fluid Mech. 36 (2004) 381-411.

[3] G. Tryggvason, R. Scardovelli, S. Zaleski, Direct Numerical Simulations of Gas-Liquid Multiphase Flows, 1st ed. Cambridge University Press, New York, 2011.

[4] M. Hemmat, A. Borhan, Buoyancy-driven motion of drips and bubbles in a periodically constricted capillary, Chem. Eng. Com. 148-150 (1996) 363-384.

[5] A.M. Worthington, On the forms assumed by drops of liquids falling vertically on a horizontal plate. Proc. R. Soc. Lond. 25 (1876) 261-272.

[6] Y. Liu, M. Andrew, J. Li, J. M. Yeomans, Z. Wang, Symmetry breaking in drop bouncing on curved surfaces, Nature Com. 6 (2015).

[7] T. Maitra, C. Antonini, M.K. Tiwari, A. Mularczyk, Z. Imeri, P. Schoch, D. Poulikakos, Supercooled Water Drops Impacting Superhydrophobic Textures, Langmuir 30:36 (2014) 10855-10861.

[8] E. Klaseboer, J.P. Chevaillier, A. Mate, O. Masbernat, C. Gourdon, Model and experiments of a drop impinging on an immersed wall, Phys. Fluids 13:1 (2001) 45-57.

[9] B. Podvin, S. Khoja, F. Moraga, D. Attinger, Model and experimental visualizations of the interaction of a bubble with an inclined wall, Chem. Eng. Sci. 63 (2008) 1914-1928.

[10] N.G. Deen, M. Annaland, J. Kuipers, Direct numerical simulation of complex multi-fluid flows using a combined front tracking and immersed boundary method, Chem. Eng. Sci. 64 (2009) 2186-2201.

[11] A. Gupta, H. Marharoo, D. Makkar, R. Kumar, Droplet formation via squeezing mechanism in a microfluidic flow-focusing device, Comp. & Fluids 100 (2014) 218-226.

[12] M.W. Baltussen, Q.I.E Segers, J.A.M. Kuipers, N.G. Deen, Cutting bubbles with a single wire, Chem. Eng. Sci. 157 (2017) 138-146.

[13] M. Muradoglu, A.D. Kayaalp, An auxiliary grid method for computations of multiphase flows in complex geometries, J. Comp. Phys., 214 (2006) 858-877.

[14] J.H. Hills, P. ChÃ©ty, The Rising Velocity of Taylor Bubbles in an Annulus, Chem. Eng. Res. & Des. 76:6 (1998) 723-727.

[15] H.K. Zhao, B. Merriman, S. Osher, L. Wang, Capturing the behavior of bubbles and drops using the variational level set approach, J. Comput. Phys. 143 (1998) 495-518.

[16] I.D. Aleinov, E.G. Puckett, M.M. Sussman, Formation of droplets in microscale jetting devices, Proceedings of FEDSM99 (1999).

[17] U. Olgac, A.D. Kayaalp, M. Muradoglu, Buoyancy-driven motion and breakup of viscous drops in constricted capillaries, Int. J. Multiph. Flow 32:9 (2006) 1055-1071.

[18] S. Protière, M. Z. Bazant, D. A. Weitz, H. A. Stone, Droplet breakup in flow past an obstacle: A capillary instability due to permeability variations, Europhysics Lett., 92:5 (2010) 54002.

[19] M. Roudet, K. Loubiere, C. Gourdon, M. Cabassud, Hydrodynamic and mass transfer in inertial gas-liquid flow regimes through straight and meandering millimetric square channels, Chem. Eng. Sci. 66:13 (2011) 2974-2990.

[20] C. Pozrikidis, Passage of a liquid drop through a bifurcation, Eng. Anal. Bound. Elem. 36:2 (2012) 93-103.

[21] S. Misra, B.K. Rana, A.K. Das, P. K. Das, Taylor Bubble Dynamics in Pipe Fittings: A Numerical Study, Fluid Mechanics and Fluid Power - Contemporary Research (2017) 989-1002.

[22] D. Izbassarov, M. Muradoglu, A computational study of two-phase viscoelastic systems in a capillary tube with a sudden contraction/expansion, Phys. Fluids 28:1 (2016).

[23] M.W. Baltussen, J.A.M. Kuipers, N.G. Deen, A numerical study of cutting bubbles with a wire mesh, Chem. Eng. Sci. 165 (2017) 25-32.

[24] G. Tryggvason, B. Bunner, A. Esmaeeli, D. Juric, N. Al-Rawahi, W. Tauber, J. Han, S. Nas, Y.J. Jan, A Front-Tracking Method for the Computations of Multiphase Flow, J. Comput. Phys. 169 (2001) 708-759.

[25] R. Scardovelli, S. Zaleski, Direct numerical simulation of free surface and interfacial flow, Annu. Rev. Fluid Mech. 31 (1999) 567-603.

[26] M. Sussman, E. Fatemi, An efficient interface-preserving level set redistancing algorithm and its application to interfacial incompressible fluid flow, SIAMJ. Sci. Comput. 20 (1999) 1165-1191.

[27] E. Olsson, G. Kreiss, A conservative level set method for two phase flow, J. Comput. Phys. 210 (2005) 225-246.

[28] N. Balcázar, O. Lehmkuhl, L. Jofre, J. Rigola, A. Oliva, A coupled volume-of-fluid/level-set method for simulation of two-phase flows on unstructured meshes, Comp. & Fluids 124 (2016) 12-19.

[29] N. Balcázar, L. Jofre, O. Lehmkuhl, J. Castro, J. Rigola, A finite-volume/level-set method for simulating two-phase flows on unstructured grids, Int. J. Multiph. Flow. 64 (2014) 55-72.

[30] N. Balcázar, O. Lehmkuhl, L. Jofre, A. Oliva, Level-set simulations of buoyancy-driven motion of single and multiple bubbles, Int. J. Heat Fluid Flow. 56 (2015) 91-107.

[31] N. Balcázar, O. Lehmkuhl, J. Rigola, A. Oliva, A multiple marker level-set method for simulation of deformable fluid particles, Int. J. Multiph. Flow. 74 (2015) 125-142.

[32] M. Chai, K. Luo, C. Shao, J. Fan, An efficient level set remedy approach for simulations of two-phase flow based on sigmoid function, Chem. Eng. Sci. 172 (2017) 335-352.

[33] O. Desjardins, V. Moureau, H. Pitsch, An accurate conservative level set/ghost fluid method for simulating turbulent atomization, J. Comput. Phys. 227 (2008) 8395-8416

[34] N. Balcázar, J. Castro, J. Rigola, A. Oliva, DNS of the wall effect on the motion of bubble swarms. Procedia Comput. Sci. 108 (2017) 2008-2017.

[35] E. Gutiérrez, N. Balcázar, E. Bartrons, J. Rigola, Numerical study of Taylor bubbles rising in a stagnant liquid using a Level-set / Moving-Mesh method, Chem. Eng. Sci. 164 (2017) 158-177.

[36] O. Estruch, O. Lehmkuhl, R. Borrell, C. D. Pérez Segarra, A. Oliva, A parallel radial basis function interpolation method for unstructured dynamic meshes, Comput. Fluids. 80 (2013) 44-54.

[37] R. Mittal, G. Iaccarino, Immersed Boundary Methods. Annual Review of Fluid Mechanics, 37:1 (2005) 239-261.

[38] C.S. Peskin, Flow patterns around heart valves: a numerical method, J. Comput. Phys., 10 (1972) 252-271.

[39] C.S. Peskin, D.M. McQueen, Modeling prosthetic heart valves for numerical analysis of blood flow in the heart, J. Comput. Phys., 37:1 (1980) 113-132.

[40] C.S. Peskin, D.M. McQueen, Cardiac fluid dynamics, Crit. Rev. Biomed. Eng., 20:5-6 (1997) 451-459.

[41] D.M. McQueen, C. S. Peskin, Shared-Memory Parallel Vector Implementation of the Immersed Boundary Method for the Computation of Blood Flow in the Beating Mammalian Heart, J. Supercomput., 236 (1997) 213-236.

[42] M.C. Lai, C.S. Peskin. An immersed boundary method with formal second-order accuracy and reduced numerical viscosity, J. Comput. Phys., 160:2 (2000) 705-719.

[43] J. Mohd-Yusof, Development of immersed boundary methods for complex geometries, Center for Turbulence Research, Annual Research Briefs, 1997, 325-336.

[44] E.A. Fadlun, R. Verzicco, P. Orlandi, J. Mohd-Yusof. Combined immersed-boundary finite-difference methods for three-dimensional complex flow simulations, J. Comput. Phys., 161:1 (2000) 35-60.

[45] E. Balaras, Modeling complex boundaries using an external force field on fixed Cartesian grids in large-eddy simulations, Comp. & Fluids, 33:3 (2004) 375-404.

[46] K. Nagendra, D.K. Tafti, K. Viswanath, A new approach for conjugate heat transfer problems using immersed boundary method for curvilinear grid based solvers, J. Comput. Phys., 267 (2014) 225-246.

[47] Y.H. Tseng, J.H. Ferziger, A ghost-cell immersed boundary method for flow in complex geometry, J. Comput. Phys., 192:2 (2003) 593-623.

[48] K. Luo, Z. Zhuang, J. Fan, N. Erland, L. Haugen, A ghost-cell immersed boundary method for simulations of heat transfer in compressible flows under different boundary conditions, Int. J. Heat Mass Transfer, Volume 104, 2017, Pages 98-111.

[49] G. Yang, D. M. Causon, D. M. Ingram. Calculation of compressible flows about complex moving geometries using a three-dimensional Cartesian cut cell method. Int. J. Numer. Methods Fluids., 33:8 (2000) 1121-1151.

[50] H.S. Udaykumar, R. Mittal, P. Rampunggoon, A. Khanna, A sharp interface Cartesian grid method for simulating flows with complex moving boundaries, J. Comput. Phys. 174:1 (2001) 345-380.

[51] T. Ye, R. Mittal, H.S. Udaykumar, W. Shyy. An Accurate Cartesian Grid Method for Viscous Incompressible Flows with Complex Immersed Boundaries, J. Comput. Phys., 156:2 (1999) 209-240.

[52] J.H. Seo, R. Mittal, A sharp-interface immersed boundary method with improved mass conservation and reduced spurious pressure oscillations, J. Comput. Phys., 230:19 (2011) 7347-7363.

[53] A. Harten, The artificial compression method for computation of shocks and contact discontinuities. III - Self-adjusting hybrid schemes, Math. Comp. 32 (1978) 363-389.

[54] J.U. Brackbill, D.B. Kothe, C. Zemach, A continuum method for modeling surface tension, J. Comput. Phys. 100 (1992) 335-354.

[55] S. Gottlieb, C. Shu, Total variation diminishing Runge-Kutta schemes, Math. Comp. 67 (1998) 73-85.

[56] A.J. Chorin. Numerical solution of the Navier-Stokes equations, Math. Comp. 22 (1968) 745-762.

[57] J.L. Guermond, P. Minev, J. Shen, An overview of projection methods for incompressible flows, Comput. Methods Appl. Mech. Eng. 195 (2006) 6011-6045.

[58] N. Balcázar, J. Rigola, J. Castro, A. Oliva, A level-set model for thermocapillary motion of deformable fluid particles, Int. J. Heat Fluid Flow. 62B (2016) 324-343.

[59] R.W. Davis, E.F. Moore, A numerical study of vortex shedding from rectangles, J. Fluid Mech. 116 (1982) 475-506.

[60] Wikipedia: STL (file format).https://en.wikipedia.org/wiki/STL_(file_format) (accessed 8 January 2018).

[61] F. Favre, G. Colomer, O. Lehmkuhl, A. Oliva, Numerical simulations of conjugate convection combined with surface thermal radiation using an Immersed-Boundary Method, J. Phys. Conf. Ser. 745:3 (2016).

[62] R.W.C.P. Verstappen, A.E.P. Veldman, Spectro-consistent discretization of Navier-Stokes: a challenge to RANS and LES, J. Engrg. Math. 34 (1998) 163-179.

[63] M. Meyer, A. Devesa, S. Hickel, X. Y. Hu, N. A. Adams. A conservative immersed interface method for Large-Eddy Simulation of incompressible flows. J. Comput. Phys., 229:18 (2010) 6300-6317.

[64] F. Favre, Numerical simulation of thermal flow problems using the Immersed Boundary Method, PhD thesis, 2017.

[65] Termo Fluids S.L. http://www.termofluids.com/, (accessed 8 January 2018).

[66] S. Hysing, S. Turek, D. Kuzmin, N. Parolini, E. Burman, S. Ganesan, L. Tobiska, Quantitative benchmark computations of two-dimensional bubble dynamics, Int. J. Numer. Meth. Fluids 60 (2009) 1259-1288.

[67] J.D. Bugg, G.A. Saad, The velocity field around a Taylor bubble rising in a stagnant viscous fluid: Numerical and experimental results, Int. J. Multiph. Flow. 28 (2002) 791-803.

[68] J. Han and G. Tryggvason, Secondary breakup of axisymmetric liquid drops. I Acceleration by a constant body force, Physics of fluids, 11:12 (1999) 3650-3667.

[69] T.Z. Harmathy, Velocity of large drops and bubbles in media of infinite or restricted extent, AIChE J. 6 (1960) 281-288.

5

Conclusions and future research

The present chapter aims at summarizing the work developed in the context of this PhD thesis. Additionally, some further work is outlined below, aiming to establish the following goals to be addressed within the present research line.

5.1 Concluding remarks

The present work developed a method to study bubbles and drops in an Arbitrary Lagrangian Eulerian formulation. The use of dynamic meshes makes possible the uncoupling of the computational domain from the physical domain. Therefore, the mesh is no longer subordinated to the geometry of the problem, which drastically increases the versatility of the solver. Some challenging problems, like the Taylor bubble problem studied in Chap. 3, are easily approachable by using the proposed technique. Moreover, the integration with an Immersed Boundary method provides an effective and versatile way to reproduce inner and intricate boundaries that do not conform the mesh shape. All these improvements were implemented on an in-house code called *Termofluids*, in the context of a finite-volume discretization, unstructured meshes and a conservative level set (CLS) multiphase treatment.

The main initial motivation of this work was reducing the computational expenditure in rising bubble problems, due to the use of long domains to capture the whole ascent of the bubble. Therefore, in chapter 2 several Domain Optimization Methods (DOMs) were presented. First, two DOMs based on periodic boundaries were introduced: the fringe zone and the buffer zone methods (Secs. 2.2.1 and 2.2.2, respectively). These techniques aim at reinitializing the perturbation that the bubble leaves when it moves in order to successfully use a periodic domain. To do this, the fringe zone method enforces an additional source term in the momentum equation (Eq. 2.2.1), and the buffer

zone method uses a region of high viscosity to dampen the bubble disturbances. On the other hand, two DOMs based on open boundaries were formulated. First, a moving mesh method was proposed. By using this method, the mesh follows the motion of the bubble, and therefore small domains covering only the important regions of the problem can be enforced. In a similar way, with the non inertial reference frame method the dynamics of the bubble are analyzed from an observer on the bubble. Both methods require a careful setting of the boundary conditions. With that purpose, a new outflow boundary condition was implemented (see Sec. 2.4). Additionally, a study on the placement of the domain limits was carried out in Sec. 2.5, providing some recommendations on how to size the computational domain. Afterwards, the proposed DOMs were tested in two and three dimensional benchmark cases. We selected the moving mesh method as the one with better performance.

Once validated, the proposed CLS+MM method was used to solve the challenging problem of the Taylor bubble. This problem is important to understand many phenomena presented in industrial applications, like oil extraction or microfluidics. A complete study of this problem was presented in Chap. 3, including mesh independence studies, description of the velocity field, time evolution, profiles evolution and streamlines maps. Additionally, particular attention was paid to the sensitivity of the problem to several physical issues, i.e. the initial shape of the bubble, the initial volume of the bubble, the flow regime and the inclination of the channel.

The next step was to adapt the CLS+MM method to complex geometries (see Ch. 4). With that purpose, an Immersed Boundary (IB) technique was adopted. This approach allows to handle complex geometries by representing them by triangular surface meshes. These bodies do not have to conform the grid shape, and they could be arbitrarily intricate and complex. The resulting CLS+MM+IB method has a direct impact on the computational resources consumption, as well as on the versatility and flexibility of the simulations. Several two and three dimensional problems were addressed in order to assess the proposed formulation. Good agreement was found for all these cases.

5.2 Future research

The current section introduces some ideas that can be taken as reference in order to push the boundaries of the research presented in this PhD thesis. Therefore, in our view, those topics constitute the natural extension of earlier achievements, and some of them are already under development in the context of the CTTC.

The CLS+MM+IB method to simulate bubbles and drops in complex geometries is the final achievement of the this thesis, and constitutes the result of all previous work done in this context. Therefore, some ideas on further improvements of this method are given in the subsections below. Before that, some paragraphs are devoted to explain

the further work that could be conducted in some related topics of the thesis, i.e. the Taylor bubble study and the improvement of other domain optimization methods.

In relation to the Domain Optimization Methods (DOMs) presented in Ch. 2, those based on periodic boundary conditions (i.e. the fringe zone and the buffer zone methods) still need further improvements to constitute a real alternative. In this sense, these methods need a careful process of setting the defining parameters of the fringe or buffer zone (namely, s, b, Δ and $\lambda_{\max}$). The first step to achieve a versatile method would be to study how these parameters are affected by the domain size and/or the flow regime. By performing a parametric study followed by a regression analysis, each of those parameters might be formulated as a function of the conditions of the problem. In this way, sufficiently precise values could be selected beforehand, thus saving simulation time. In relation to the buffer zone method, it has the additional disadvantage of presenting large simulation times, due to the reduction of the time step as a consequence of the high values of viscosity in some regions of the domain. This problem could be straightforwardly addressed by using an implicit method to solve the fractional step method.

Regarding the Taylor bubble problem, while there has been marked improvements in the solution of this problem, challenges remain. First, further configurations could be solved, involving not only straight tubes, but also circular pipes, helical, meandering, etc. There is a huge lack of studies about these configurations available in the literature. The method presented in Ch. 4 is capable of solving those problems in a wide range of flow conditions. Furthermore, by coupling that method with an energy solver (see for instance [1]) the heat transfer resulting from the passage of a Taylor bubble could be analyzed. Additionally, the problem of a Taylor bubble rising in inclined pipes in scenarios where the suspending fluid is not stagnant is a problem of huge relevance for the industry (for instance, in oil extraction processes). That problem could be addressed with the tools presented through the present thesis.

Regarding the enhancement of the CLS+MM+IB method to simulate bubbles/drops in complex geometries, there are two main groups of task to be developed. On the one hand, once the method has proven effective, its potential could be released to seed some light in different problems of great importance for the industry, e.g. the sudden expansion or contraction of a Taylor bubble, the evolution of a micro-drop inside a porous media, the interaction of bubbles with textured surfaces, etc. On the other hand, some improvements in the formulation of the method could still be carried out, in order to increase even further the versatility of the method. Those actions deserve a particular attention, and they have been treated separately in the subsequent subsections.

5.2.1 Dynamic readjustment of the distances from the bubble/-drop to the boundaries

The study presented in Sec. 2.5 about the placement of the inlet and outlet boundary condition can be improved. Indeed, considering the boundary treatment presented in Sec. 4.3.1 the concept of fixed boundaries becomes obsolete. In that section, we proposed a generalized concept of "open boundary", which homogenizes every boundary of the computational domain and applies particular conditions depending on the relation between the unit normal vector to the boundary face and the bubble/drop velocity. With this formulation, a new approach to compute the distance from the bubble/drop to the boundaries would be needed. Two main ideas are proposed (see Fig. 5.1):

- An optimal distance $D_{\text{opt}} = \mathscr{F} \cdot d$ from a generic boundary face F to the bubble/-drop centroid can be predicted. Here, $\mathscr{F}$ is a generic fitting function and d is the initial diameter of the drop/bubble. This distance D_{opt} assures that the solution is minimally upset (i.e. the velocity of the bubble/drop is perturbed by less than a small threshold value). By running a parametric study and performing a regression analysis, a function $\mathscr{F} = \mathscr{F}\left(\mathrm{v}_{\perp}^{*}\right)$ the can be fitted. This function should depends on the dimensionless projection of the velocity of the bubble/drop $\mathrm{v}_{\perp}^{*}$ over the unit normal vector to the face. By proceeding this way, each boundary face will have a value of D_{opt} associated, and therefore an optimal position for the bubble/drop can be obtained.

- The procedure explained in the item above may allow the motion of the drop/bubble within the computational domain. Therefore, by deforming the mesh, an optimal distribution of the cell sizes can be obtained, in order to increase the accuracy of the simulation in the important regions of the problem.

5.2.2 Domain sizing

In the present PhD thesis, we always have used rectangular meshes in two-dimensional problems, and cylindrical ones in three-dimensional problems. Nonetheless, these shapes may not be the most efficient configurations. Thus, it seems necessary to carry out a detailed study on this topic. Without this study, the large effort made throughout this thesis on the optimization of the proposed method would not seem to be fully complete.

For problems of drops/bubbles evolving in non-constricting geometries (i.e. those in which the solid does not determine the trajectory of the drop/bubble beforehand), we propose to carry out a parametric study depending on the flow regime. For each of these cases and depending on the instant velocity of the bubble/drop, the cells that are not "aware" of the presence of the bubble/drop can be identified by filtering the velocity

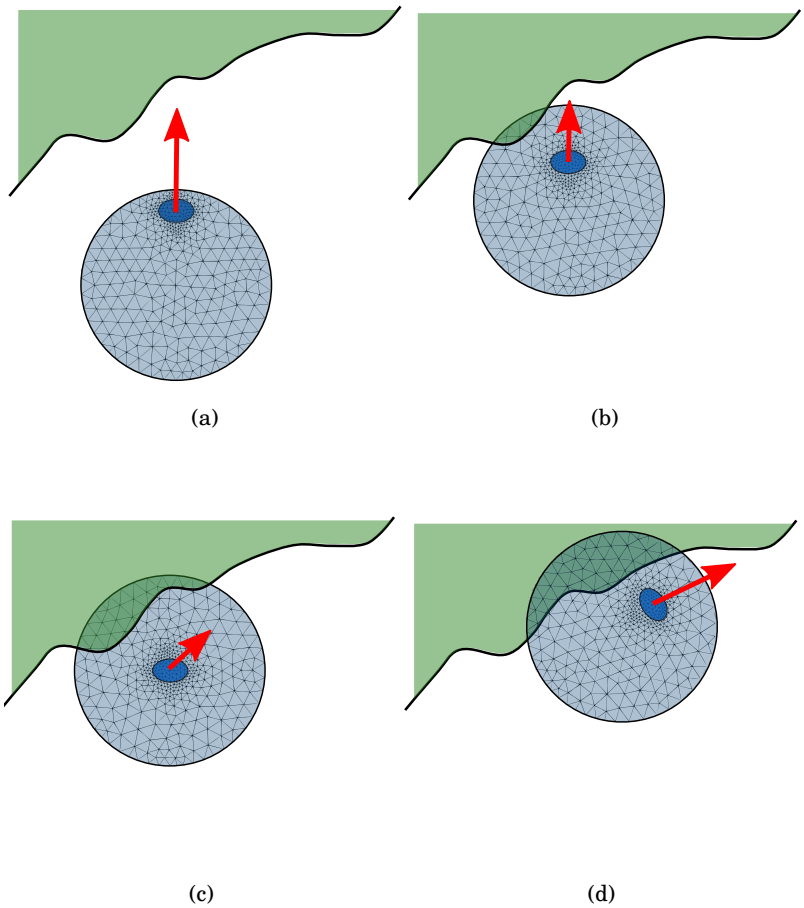

Figure 5.1: Sketch of the mechanism to change the distance from bubble/drop centroid to the boundaries.

field (e.g. applying a threshold of the 1% of the velocity of the drop/bubble). Therefore, an optimal domain for that specific time instant can be obtained and, thereafter, global conclusions on the shape of the domain depending on the regime could be draw by considering all the time instants of the simulation and the selected flow regime.

For problems of drops/bubbles in constricting geometries (i.e. tubular solids), the suggested procedure to find the optimal domain shape is different from the one presented in the previous paragraph. In this case, we propose to follow a semi-analytical approach in order to optimize the dimensions of the mesh. The challenging issue here

is to assure that the mesh is of sufficient width to cover the whole transversal section of the tube throughout the complete simulation (see Fig. 5.2). Therefore, given the driven and the driving curves of the pipe, this issue is essentially a problem of calculus of variations.

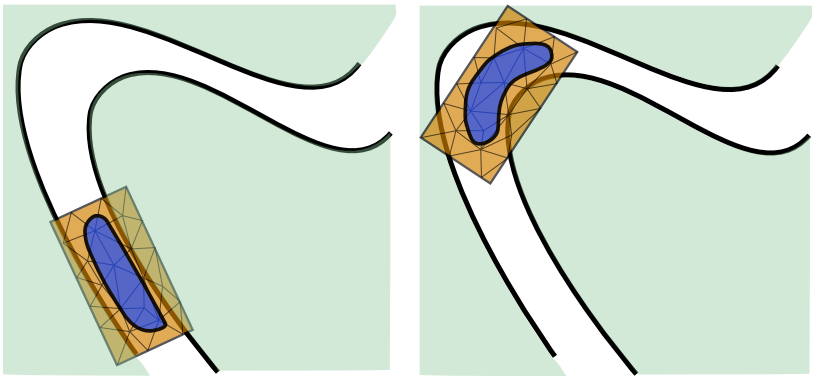

(a) (b)

Figure 5.2: Sketch of two instants of an example case, where the width of the mesh fails to cover the whole transversal section of the domain.

5.2.3 Deformability of the solids

So far, the solids are treated as rigid bodies, i.e. no deformation is allowed. However, in a real scenario, the motion of the fluids within the domain may alter the position or shape of the solids (see Fig. 5.3). For instance, an overpressure in a specific region of a flexible tube might cause an increase of the transversal area. Additionally, the passage of a bubble by a valve is conditioned by the elastic properties of the boundary walls. Those cases have a crucial importance in many engineering and biomedical cases, for example in the study of embolisms, oil extraction, micro-fluids, etc.

Modeling the deformation of the immersed bodies represented by triangular surface meshes (STL files) is a topic which falls within the broad field of the fluid-structure interaction. Some progresses have been already done in the study of bubbles/drops evolving through flexible geometries [2–4]. Nevertheless, to the author's knowledge, there are no previous works on this topic using a DNS conservative level set formulation, nor an immersed boundary method.

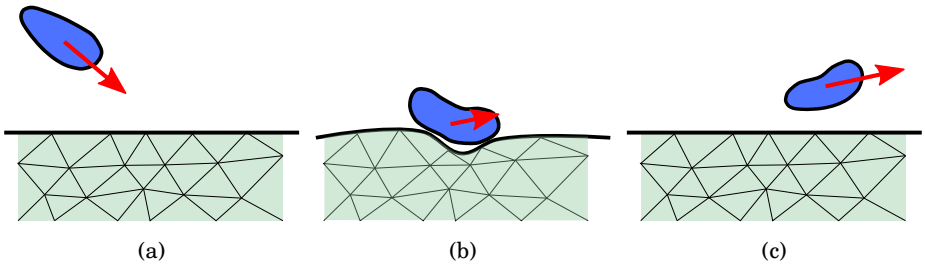

Figure 5.3: Sketch of the elastic impact of a drop against a flexible surface.

5.2.4 Contact angle model

The dynamics of a secondary phase in full-contact with a solid is an important phenomenon for many industrial applications, such as cooling of nuclear reactors, sprays and piping. It is well-known that the surface characterization in terms of its physical properties constitutes a crucial factor to determine the behaviour of the drop when interacting with that surface. Some of these properties include roughness, ion affinity, and patterns that could be "drawn" over the surface.

The usual approach to simulate that complex phenomena in DNS methodologies is modeling a macroscopic magnitude: the contact angle between fluids and solid. So far, the method developed in this thesis is not able to simulate a generic full-contact between phases, and only a contact angle condition of 90 degrees can be imposed, as it is inherent in the Neumann boundary condition.

Therefore, a suitable contact angle model is needed to generalize the method presented in previous chapters. In this regard, some progresses have already been done within the scientific community. There are already some valuable works that aim to shed some light on the modeling of the contact angle phenomenon. Albadawi et al. [5] proposed a robust model to impose contact angle conditions in a VoF formulation. The model of Sussman [6] has the concomitant advantage of avoiding locating the triple line in order to impose the contact angle boundary condition. Yokoi et al. [7] successfully validates the Sussman's model, and extended it to further situations. Considering the particularities of our method, the model of Sussman seems the most suitable starting point, since it is formulated within a single fluid method, and using an Immersed Boundary approach.

5.2.5 Coalescence and break-up

As discussed in Sec. 4.4, the method developed through this thesis is not able to deal with problems where two or more bubbles/drops coexist. This is because the motion

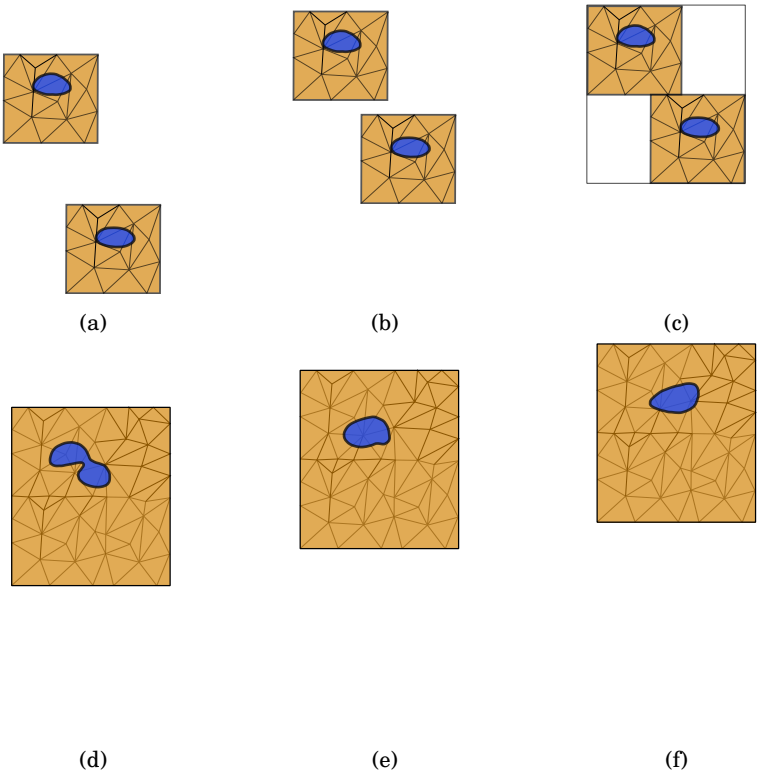

Figure 5.4: Sketch of the coalescence of two bubbles using an extended technique of the CLS+MM+IB approach.

of the mesh is defined in terms of the velocity of the centroid of a single bubble/drop. Therefore, in cases with multiple drops/bubbles, this criterion becomes obsolete.

However, the fact of working with multiple bubbles/drops is feasible in the context of the CLS+MM+IB method developed in this thesis. The idea is to take advantage of the auto-meshing tools and the software devoted to interconnect different simulation domains (e.g. the NEST code developed at CTTC). By proceeding in this way, coalescence could be study by running two independent simulations, and "merge" both computational domains at some point of the simulation. Fig. 5.4 sketches this process. Similar ideas could be applied to problems involving break-up.

References

[1] N. Balcázar, J. Rigola, J. Castro, A. Oliva, A level-set model for thermocapillary motion of deformable fluid particles, Int. J. Heat Fluid Flow. 62B (2016) 324-343.

[2] V. Coralic and T. Colonius, Shock-induced collapse of a bubble inside a deformable vessel, European Journal of Mechanics B/Fluids 40 (2013), 64-74.

[3] H. Miao, S. M. Gracewski and D. Dalecki, Ultrasonic excitation of a bubble inside a deformable tube: Implications for ultrasonically induced hemorrhage, J. Acoust. Soc. Am. 124:4 (2008) 2374-2384.

[4] S. Martynov, E. Kostson, N. Saffari and E. Stride, Forced vibrations of a bubble in a liquid-filled elastic vessel, J. Acoust. Soc. Am. 130:5 (2011) 2700-2708.

[5] A. Albadawi, D.B. Donoghue, A.J. Robinson, D.B. Murray, Y.M.C. DelaurÃ©, On the assessment of a VOF based compressive interface capturing scheme for the analysis of bubble impact on and bounce from a flat horizontal surface, Int Journal of Multiphase Flow 65, pp. 82-97, 2014.

[6] M. Sussman Adaptive Method of Lines: Chapter 7 "An Adaptive Mesh Algorithm for Free Surface Flows in General Geometries", A, Vande Wouwer, , Ph. Saucez,W.E. Schiesser, 2001.

[7] K. Yokoi, D. Vadillo, J. Hinch, I. Hutchings, Numerical studies of the influence of the dynamic contact angle on a droplet impacting on a dry surface, Physics of Fluids 21, pp- 72-102, 2009.

A

Calculations of bubble/drop properties

The kinematic properties of a single bubble/drop are computed as explained below. The following expressions are directly given in their discrete form. The position of the bubble/drop centroid G is computed as follows:

$$\mathbf{x}_{\mathrm{G}} = \frac{\sum_n \mathbf{x}^n \phi^n V^n}{\sum_n \phi^n V^n} \tag{A.1}$$

where subscript n denotes that the corresponding variable is evaluated at the node n under consideration. V is the volume of the corresponding CV, $\mathbf{x}$ is the position vector of its centroid, and ϕ is the level set function. In addition, the velocity of the bubble/drop is given by:

$$\mathbf{v}_{\mathrm{G}} = \frac{\sum_n \mathbf{v}^n \phi^n V^n}{\sum_n \phi^n V^n} \tag{A.2}$$

The total volume of the secondary phase V_2 can be computed as:

$$V_2 = \sum_n \phi^n V^n \tag{A.3}$$

Here the integral is computed on the complete domain. Additionally, bubble/drop acceleration $\mathbf{a}_G$ can be expressed as:

$$\mathbf{a}_G = \frac{\mathrm{d}\mathbf{v}_G}{\mathrm{d}t} \tag{A.4}$$

In order to discretize the previous equation, a second order finite difference scheme is used

$$\mathbf{a}_G = \frac{\mathrm{d}t^{m-1}\left(\mathrm{d}t^{m-1} + \mathrm{d}t^m\right)\mathbf{v}_G^m - \left(\mathrm{d}t^m + \mathrm{d}t^{m-1}\right)^2 \mathbf{v}_G^{m-1} + (\mathrm{d}t^m)^2 \mathbf{v}_G^{m-2}}{\mathrm{d}t^m \cdot \mathrm{d}t^{m-1}\left(\mathrm{d}t^m + \mathrm{d}t^{m-1}\right)} \tag{A.5}$$

where superscripts indicate the time iteration corresponding to each variable. The accuracy of this formula is consistent with other schemes used to discretize the governing equations. For the first time step, a first order finite difference scheme is needed, because it is not possible to apply the second order formula.

Finally, in two dimensional problems, the circularity ζ_{2D} measures the deformation with respect to a perfect circular bubble/drop. It is computed as:

$$\zeta_{2D} = \pi d \frac{\sum_n \left\| \nabla \phi \right\|^n V^n}{\sum_n \phi^n V^n} \tag{A.6}$$

where d is the bubble/drop initial diameter. The integral is computed on the complete domain. the sphericity ζ_{3D} is defined for a three-dimensional bubble/drop; this yields:

$$\zeta_{3D} = \frac{\pi d^2}{\sum_n \left\| \nabla \phi^n \right\| V^n} \tag{A.7}$$

B

Exact calculation of the swept volume for moving mesh methods

In the current appendix the exact volume swept by the mesh faces while deforming is calculated. Based on [1], a first order error is obtained for the calculation of this volume. That work proposed an approach based on a linear interpolation of the position of the vertices. In some CFD methodologies, this approach could reduce the order of accuracy of the overfall algorithm. A straightforward improvement of this technique would be to use an interpolation scheme of higher order. However, when the mesh is being moved following a driven curve, the exact path of each vertex is known. Therefore, an exact calculation of the swept volume of the faces can be computed.

In the following sections, we present an algorithm to compute the deformation of the vertices of a mesh trough a given curve. Furthermore, particular remarks have been put forward for some specific cases, i.e. extruded meshes, two-dimensional meshes, 2D and 3D cylindrical mesh curved along a circumference.

Throughout the present PhD thesis, a Conservative Level-Set (CLS) method is used to deal with the multiphase flow. This technique is focused on solving the mass conservation issue, one of the classical problems of the standard Level-Set (SLS) approach. Thus, to be consistent with this formulation a special care should be taken in the mass flow update process of the moving mesh method. This step is needed to properly implement any dynamic mesh method. Therefore, under some assumptions, an exact mass update process is going to be developed, aiming to minimize the mass error resulting from moving the mesh.

B.1 Moving the mesh through a curve

Given an arbitrary mesh M and a driving curve Γ, a precise description of the movement of a vertex $\mathrm{V} \in M$ along the curve Γ is sought. We assume that the curve Γ is analytical, but if it were given in a discrete form (as a set of points), the procedure described below is still applicable after interpolation among points (see for instance [2]).

A global inertial reference frame $OXYZ$ is used. The mesh is going to be deformed each time step in order to follow the bubble rise. The distance ℓ that the bubble rises each time step is defined as:

$$\ell = \mathrm{v}_G \cdot dt \tag{B.1}$$

where v_G is the velocity of the centroid G of the bubble, and dt is the current time step. Distance ℓ coincides with the distance that the mesh moves.

The curve Γ is a sufficiently smooth simple curve ($\Gamma \in C^3$) given in parametric form as:

$$\Gamma \equiv \mathbf{r}(s) \equiv \overrightarrow{OR} = [x(s), y(s), z(s)] \tag{B.2}$$

Without loss of generality [3], we assume that s is the arc length parameter of the curve. The Frenet-Serret frame of the driving curve is defined by the tangential $\mathbf{t}(s)$, normal $\mathbf{n}(s)$ and the binormal $\mathbf{b}(s)$ vectors of Γ, given by the following expressions:

$$\mathbf{t}(s) = \frac{d\mathbf{r}(s)}{ds} \quad ; \quad \mathbf{n}(s) = \frac{1}{\left\| \frac{d\mathbf{t}(s)}{ds} \right\|} \cdot \frac{d\mathbf{t}(s)}{ds} \quad ; \quad \mathbf{b}(s) = \mathbf{t}(s) \times \mathbf{n}(s) \tag{B.3}$$

Now, Π denotes the perpendicular plane to Γ that contains the vertex V to be moved. Then, the point P defined as the intersection of Π and Γ is easily moved with simply going through the curve Γ a distance ℓ. The new position of the point P is defined as P' and the perpendicular plane to Γ at P' is defined as Π'. This geometrical arrangement is shown in Fig. B.1. The vertex V is forced to be moved in unison with the frame $\{\mathbf{t}(s), \mathbf{n}(s), \mathbf{b}(s)\}$. This condition is tantamount to saying that a certain fixed line in the plane Π always coincides with the binormal $\mathbf{b}$ of Γ.

Therefore, ones defined the frame $\{\mathbf{t}(s), \mathbf{n}(s), \mathbf{b}(s)\}$, the plane Π can be parametrically represented as:

$$\Pi \equiv \Pi(\lambda, \mu) = \mathbf{r}(s_1) + \lambda \mathbf{n}(s_1) + \mu \mathbf{b}(s_1) \tag{B.4}$$

where s_1 is the arc length parameter of the curve at the position of P. On the other hand, plane Π' is similarly given by:

$$\Pi' \equiv \Pi'(\lambda, \mu) = \mathbf{r}(s_2) + \lambda \mathbf{n}(s_2) + \mu \mathbf{b}(s_2) \tag{B.5}$$

where s_2 is the arc length parameter of the curve at the position of P'. Thus, the coordinates of V are given by:

$$\overrightarrow{OV} = \mathbf{r}(s_1) + \lambda_0 \mathbf{n}(s_1) + \mu_0 \mathbf{b}(s_1) \tag{B.6}$$

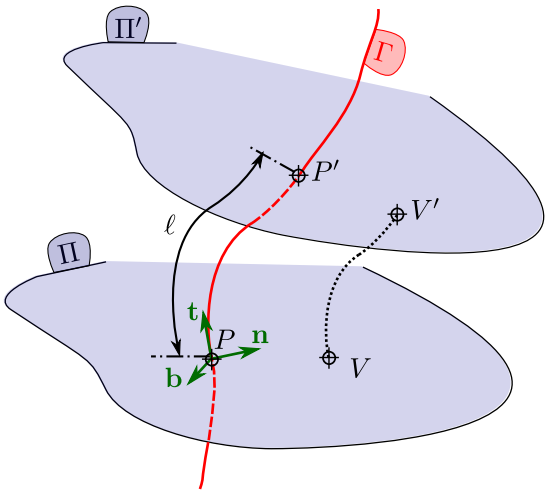

Figure B.1: Geometrical arrangement of the motion of a vertex V through a driving curve Γ. Variables with «$'$»refer to the moved state. P is the intersection point between the plane Π containing V and Γ. The frame $\{\mathbf{t},\mathbf{n},\mathbf{b}\}$ is the Frenet-Serret frame. Finally, ℓ is the distance that the point P is moved.

which allows the calculation of the parameters $\{\lambda_0,\mu_0\}$, since coordinates of V are known. Finally, the coordinates of V$'$ (the moved V) are given by:

$$\overrightarrow{OV'} = \mathbf{r}(s_2) + \lambda_0\mathbf{n}(s_2) + \mu_0\mathbf{b}(s_2) \tag{B.7}$$

and the displacement vector is $\mathbf{VV'} = \overrightarrow{OV'} - \overrightarrow{OV}$. By following this procedure with each vertex V_i of the mesh M, the new mesh M' is easily obtained.

B.1.1 Two dimensional case

The procedure described above can be readily particularized for a two-dimensional situation, in order to get a more natural formulation. Given an arbitrary mesh M and a driving curve Γ in the plane OXY, the position of the mesh when it moves a distance ℓ along the driving curve is sought. The curve Γ is implicitly described as:

$$\Gamma \equiv F(x,y) = 0 \tag{B.8}$$

The frame $\{\mathbf{t},\mathbf{n}\}$ is defined as:

$$\mathbf{t} = \frac{1}{\sqrt{F_x^2+F_y^2}}\begin{pmatrix} F_y \\ -F_x \end{pmatrix} \quad ; \quad \mathbf{n} = \frac{1}{\sqrt{F_x^2+F_y^2}}\begin{pmatrix} F_x \\ F_y \end{pmatrix} \tag{B.9}$$

where F_x and F_y are the partial derivatives of $F(x,y)$.

Now, π is the perpendicular line to Γ that contains the vertex V to be moved, and P is the intersection point between π and Γ. Then, the point P' (the moved P) is obtained going a distance ℓ through the curve Γ. The perpendicular line to Γ at P' is defined as π'. The parametric representation of lines π and π' are:

$$\pi \equiv r(\lambda) = \overrightarrow{OP} + \lambda \mathbf{n}_P \qquad ; \qquad \pi' \equiv r'(\lambda) = \overrightarrow{OP'} + \lambda \mathbf{n}_{P'} \tag{B.10}$$

where $\mathbf{n}_P$ and $\mathbf{n}_{P'}$ denote that the normal vector is evaluated at the point indicated in the subscript. Thus, the coordinates of the vertex V are given by:

$$\overrightarrow{OV} = \overrightarrow{OP} + \lambda_0 \mathbf{n}_P \tag{B.11}$$

which allows the calculation of the parameter λ_0, since coordinates of V are known. Finally, the coordinates of V′ (the moved V) are given by:

$$\overrightarrow{OV'} = \overrightarrow{OP'} + \lambda_0 \mathbf{n}_{P'} \tag{B.12}$$

and the displacement vector is given by $\overrightarrow{VV'} = \overrightarrow{OV'} - \overrightarrow{OV}$.

B.1.2 Numerical considerations for particular cases

The process described below is computationally expensive. It requires the calculation of a considerable amount of geometrical parameters for each vertex of the mesh. However, for some specific meshes and/or driving curves, the procedure explained above can be optimized in order to get a faster computation. For instance, if the driving curve Γ is only composed of linear segments, the moving mesh technique is trivially simplified by just moving each vertices a distance ℓ along the corresponding linear segment.

Other specific circumstances can give rise to notably simplifications in the calculation algorithm. That is the case with meshes generated by extrusion of a two-dimensional grid. In this case, the vertices of each layer are moved to the same plane, so the computation process should be intelligently structured, in order to avoid duplication of calculations.

The particular case of a cylindrical mesh is study in detail in Sec. B.3, due to its special relevance in terms of applicability.

B.2 Mass update process

In order to preserve the computational volume in a dynamic mesh framework, the so-called *Space Conservation Law* (SCL) should be used [1], giving rise to the following equation:

$$\dot{m}_F^{\text{modified}} = \dot{m}_F - \rho_F \frac{\Omega_F}{\Delta t} \tag{B.13}$$

where $\dot{m}_F^{\text{modified}}$ is the modified mass trough face F, $\dot{m}_F$ is the original mass trough face F, ρ_F is the density at face F, and Ω_F is the volume swept by the face F during the time step Δt. Fig. B.2 depicts this swept volume by a face in a general movement. The aim in the present section is to exactly evaluate this swept volume Ω_F in the current problem. In order to do this, the work of Goodman and Goodman [4] is followed, adapting the formulation to this particular case.

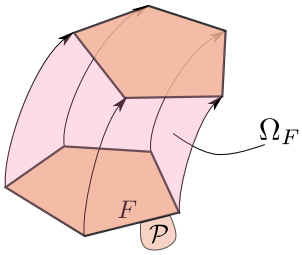

Figure B.2: Volume Ω_F swept by a face F in its motion. $\mathscr{P}$ is the polygon which delimit the face F.

As stated, the volume swept by a face F when its vertices are moved following a driving line Γ is going to be obtained. No self-intersection is assumed in this movement. F is assumed to be plane. A global inertial frame $O_1X_1Y_1Z_1$ and a local frame $O_2X_2Y_2Z_2$ attached to the face F are taken. For simplicity without loss of generality, the $O_2X_2Y_2$ plane is taken to contain the face F. Furthermore, the frame $O_2X_2Y_2Z_2$ satisfy the following condition: $\overrightarrow{O_2R_0}$ is parallel to the binormal vector $\mathbf{b}(s)$ of Γ, where $\overrightarrow{O_2R_0}$ and the point O_2 define a certain fixed line in the $O_2X_2Y_2$ plane. This obliges the face F to move in unison with the Frenet-Serret frame of Γ, thus moments of F about the axes of $O_2X_2Y_2Z_2$ frame are maintained constant (see [4]).

The polygon $\mathscr{P}$ which comprises the edges of the face F is defined in $O_2X_2Y_2Z_2$ as:

$$\mathscr{P} \equiv \mathbf{r}_P(\xi) = \overrightarrow{O_2R_1} = [f(\xi), g(\xi), 0] \qquad 0 \le \xi \le M \tag{B.14}$$

where ξ is the length arc of $\mathscr{P}$ and M is the total length of $\mathscr{P}$. Fig. B.3 illustrates the geometrical arrangement.

$\mathscr{S}$ denotes the surface of the solid $\mathscr{V}$ generated in the movement of F, and it is defined by the position vector $\overrightarrow{O_1P}$:

$$\overrightarrow{O_1P} = \overrightarrow{O_1O_2} + \overrightarrow{O_2P} \tag{B.15}$$

or,

$$\mathscr{S} \equiv \mathbf{P}(s,\xi) = \mathbf{r}(s) - f(\xi)\mathbf{n}(s) - g(\xi)\mathbf{b}(s) \tag{B.16}$$

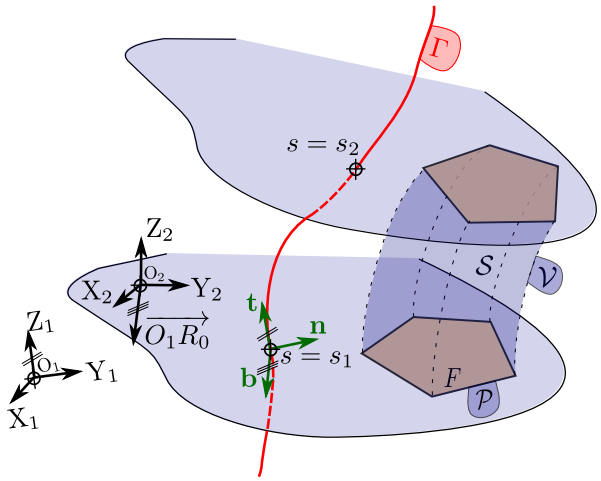

Figure B.3: Geometrical arrangement of the motion of a face F through a driving curve Γ. $O_1X_1Y_1Z_1$ and $O_2X_2Y_2Z_2$ are auxiliary frames defined in the text. $\{\mathbf{t},\mathbf{n},\mathbf{b}\}$ is the Frenet-Serret frame. $\mathscr{V}$ is the volume swept by the motion of the face F. $\mathscr{S}$ is its lateral surface. Finally, $\mathscr{P}$ is the polygon which delimit the face F.

An arbitrary point Q belongs to the surface $\mathscr{S}$ if and only if a pair (s_0,ξ_0) exists, such that $\mathbf{P}(s_0,\xi_0) = \overrightarrow{O_1Q}$, with $s_1 \le s_0 \le s_2$ and $0 \le \xi_0 \le M$.
Now, in order to calculate the volume of $\mathscr{V}$, the Gauss Theorem is applied:

$$\iiint_{\mathscr{V}} \nabla\cdot\mathbf{P}\mathrm{d}V = \iint_{\mathscr{S}} \mathbf{P}\cdot\mathbf{n}\mathrm{d}\sigma \tag{B.17}$$

where $\mathbf{n}$ is an outward unit normal vector, and $\mathrm{d}V$ and $\mathrm{d}\sigma$ are the volume element and the surface element, respectively. Since $\mathbf{P}$ is a position vector, $\nabla\cdot\mathbf{P} = 3$ and then,

$$\Omega_F = \frac{1}{3}\iint_{\mathscr{S}} \mathbf{P}\cdot\mathbf{n}\mathrm{d}\sigma \tag{B.18}$$

In order to calculate this integral, the chosen parameterizations for Γ and $\mathscr{P}$ must be specified, with the objective of maiking $\mathbf{n}$ indeed the outward normal vector to the solid $\mathscr{V}$. This occurs if:

1. The chosen parametrization in (B.14) should describe $\mathscr{P}$ counterclockwise as ξ increases.

2. The global frame $O_1X_1Y_1Z_1$ should satisfy that O_1Z_1 axis is parallel to the tangent vector $\mathbf{t}$ of the curve Γ at $s = s_1$ (initial position).

3. The following definition is settled:

$$\mathbf{n}\mathrm{d}\sigma = \frac{\partial \mathbf{P}}{\partial \xi} \times \frac{\partial \mathbf{P}}{\partial s}\mathrm{d}\xi\mathrm{d}s \tag{B.19}$$

Using Eq. (B.16), the definition of the Frenet-Serret frame (Eq. (B.3)) and the fact that the frame $\{\mathbf{t}(s), \mathbf{n}(s), \mathbf{b}(s)\}$ forms a righthanded orthonormal system, the next expressions were found:

$$\frac{\partial \mathbf{P}}{\partial \xi} = -f'(\xi)\mathbf{n}(s) - g'(\xi)\mathbf{b}(s) \tag{B.20}$$

$$\frac{\partial \mathbf{P}}{\partial s} = (1 + f(\xi)\kappa(s))\mathbf{t}(s) + g(\xi)\tau(s)\mathbf{n}(s) - f(\xi)\tau(s)\mathbf{b}(s) \tag{B.21}$$

where $\kappa(s)$ and $\tau(s)$ are respectively the curvature and the torsion of the curve Γ, defined as:

$$\kappa(s) = ||\mathbf{t}'(s)|| \qquad ; \qquad \tau(s) = -\mathbf{n}(s)\cdot\mathbf{b}'(s) \tag{B.22}$$

Functional dependencies are suppressed hereinafter for the sake of clarity (i.e. $f(\xi) \sim f$, $\kappa(s) \sim \kappa$, etc.). By multiplying the expressions obtained in Eqs. (B.20) and (B.21), the following relationship is obtained:

$$\frac{\partial \mathbf{P}}{\partial \xi} \times \frac{\partial \mathbf{P}}{\partial s} = \left(ff' + gg'\right)\tau\mathbf{t} - g'(1 + f\kappa)\mathbf{n} + f'(1 + f\kappa)\mathbf{b} \tag{B.23}$$

In light of the foregoing, it is found that:

$$\Omega_F = \frac{1}{3}\iint_{\mathscr{S}} \mathbf{P}\cdot\mathbf{n}\mathrm{d}\sigma = \frac{1}{3}(I_1 - I_2 + I_3 + I_4 - I_5) \tag{B.24}$$

where

$$I_1 = \iint_{\mathscr{S}} \mathbf{r}\cdot\mathbf{t}\left(ff' + gg'\right)\tau\mathrm{d}\xi\mathrm{d}s \tag{B.25}$$

$$I_2 = \iint_{\mathscr{S}} \mathbf{r}\cdot\mathbf{n}g'(1 + f\kappa)\mathrm{d}\xi\mathrm{d}s \tag{B.26}$$

$$I_3 = \iint_{\mathscr{S}} \mathbf{r}\cdot\mathbf{b}f'(1 + f\kappa)\mathrm{d}\xi\mathrm{d}s \tag{B.27}$$

$$I_4 = \iint_{\mathscr{S}} fg'(1 + f\kappa)\mathrm{d}\xi\mathrm{d}s \tag{B.28}$$

$$I_5 = \iint_{\mathscr{S}} gf'(1 + f\kappa)\mathrm{d}\xi\mathrm{d}s \tag{B.29}$$

Each of these integrals have terms of the form $T(\xi)J(s)$, so we can write:

$$\iint_{\mathscr{S}} T(\xi)J(s)\mathrm{d}\xi\mathrm{d}s = \int_{s_1}^{s_2}\int_0^M T(\xi)J(s)\mathrm{d}\xi\mathrm{d}s = \left(\int_0^M T(\xi)\mathrm{d}\xi\right)\left(\int_{s_1}^{s_2} J(s)\mathrm{d}s\right) \tag{B.30}$$

In addition, it often occurs that the right-side term of Eq. (B.30) is zero, due to the fact that the polygon $\mathscr{P}$ is continuous and piecewise differentiable. Thus, in order to simplify Eq. (B.24), the following results were found helpful:

$$\int_0^M \left(ff' + gg'\right) \mathrm{d}\xi = \frac{1}{2}\left(f^2(\xi) + g^2(\xi)\right)\Big|_0^M = 0 \tag{B.31}$$

$$\int_0^M g' \mathrm{d}\xi = g(M) - g(0) = 0 \tag{B.32}$$

$$\int_0^M f' \mathrm{d}\xi = f(M) - f(0) = 0 \tag{B.33}$$

$$\int_0^M fg' \mathrm{d}\xi = \oint_{\mathscr{P}} X \mathrm{d}Y = A \tag{B.34}$$

$$\int_0^M gf' \mathrm{d}\xi = \oint_{\mathscr{P}} Y \mathrm{d}X = -A \tag{B.35}$$

$$\int_0^M f^2 g' \mathrm{d}\xi = \oint_{\mathscr{P}} X^2 \mathrm{d}Y = \iint_F 2X \mathrm{d}X \mathrm{d}Y = 2M_Y \tag{B.36}$$

$$\int_0^M fgf' \mathrm{d}\xi = \oint_{\mathscr{P}} XY \mathrm{d}X = \iint_F -X \mathrm{d}X \mathrm{d}Y = -M_Y \tag{B.37}$$

where X and Y are the Cartesian coordinates in the $O_2X_2Y_2Z_2$ frame, A is the area of the face F, and M_Y is the moment of F about the Y_2-axis. Besides, the following two derivations are also needed:

$$\int_{s_1}^{s_2} \mathrm{d}s = \ell \tag{B.38}$$

$$\begin{aligned}\int_{s_1}^{s_2} \mathbf{r}\cdot\mathbf{n}\kappa \mathrm{d}s &= \int_{s_1}^{s_2} \mathbf{r}\cdot\mathbf{t}' \mathrm{d}s = \int_{s_1}^{s_2} \mathbf{r}\cdot\mathbf{r}'' \mathrm{d}s = \int_{s_1}^{s_2} \left[\left(\mathbf{r}\cdot\mathbf{r}'\right)' - \mathbf{r}'\cdot\mathbf{r}'\right] \mathrm{d}s \\ &= \mathbf{r}(s_2)\cdot\mathbf{r}'(s_2) - \mathbf{r}(s_1)\cdot\mathbf{r}'(s_1) - \int_{s_1}^{s_2} \mathbf{t}\cdot\mathbf{t} \mathrm{d}s = \ell' - \ell\end{aligned} \tag{B.39}$$

being

$$\ell' = \mathbf{r}(s_2)\cdot\mathbf{r}'(s_2) - \mathbf{r}(s_1)\cdot\mathbf{r}'(s_1) \tag{B.40}$$

By using Eqs. (B.30) to (B.39) in Eq. (B.24), it is found that I_1 and I_3 are equal to zero, and:

$$\Omega_F = A\ell - \frac{A\ell'}{3} + M_Y \int_{s_1}^{s_2} \kappa(s) \mathrm{d}s \tag{B.41}$$

B.3 Particular case: Extruded cylindrical mesh moving along a circumference

A very common situation that deserves to be particularly studied is an extruded cylindrical domain that moves along a circumference. The purpose of the current section is to rewrite the general formulation in order to make it more manageable for this particular case. The subsequent derivations are done for a three-dimensional case, but the particularization for a two-dimensional case is straightforward.

The initial state is defined by a cylindrical mesh M and a driving curve Γ, as is shown in Fig. B.4. The diameter of the cylinder is D and its height is L_y. A global frame $OXYZ$ is defined, with its origin at the center of the cylinder's base, and with the y-axis in accordance with the cylinder's axis. The curve Γ is given by the following expression:

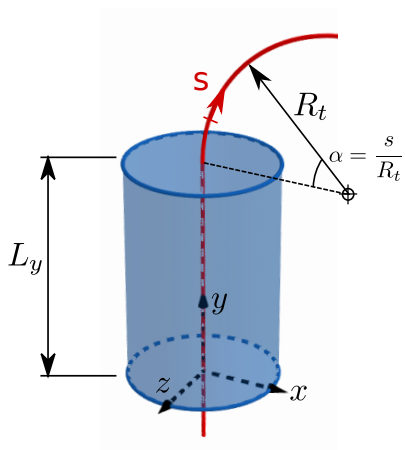

Figure B.4: Particular case of a cylindrical mesh moving along a circumference

$$\Gamma \equiv \mathbf{r}(s) = \begin{cases} (0,s,0) & \text{if } s < L_y \\ \left(R_t\left(1-\cos\left(\frac{s}{R_t}\right)\right), L_y + \sin\left(\frac{s}{R_t}\right), 0\right) & \text{if } s \geq L_y \end{cases} \tag{B.42}$$

where R_t is the turning radius of Γ and s is the arc length parameter. The point C is the center of the turning circumference, and it is defined by $\overrightarrow{OC} = (R_t, L_y, 0)$. Now, V is the vertex of the mesh which is going to be moved to a new position V', once the mesh ascents a distance ℓ. The position vector of V is $\overrightarrow{OV} = (x_V, y_V, z_V)$. If $y_V + \ell \leq L_y$, the displacement vector $\overrightarrow{VV'}$ is given by $\overrightarrow{VV'} = (0, \ell, 0)$. If, on the contrary, $y_V + \ell > L_y$, the

displacement vector is given by:

$$\overrightarrow{VV'} = \left(2||\overrightarrow{R_V}||\sin\left(\frac{\alpha}{2}\right)\cos\left(\frac{\pi}{2}-\frac{\alpha}{2}-\alpha_t\right), 2||\overrightarrow{R_V}||\sin\left(\frac{\alpha}{2}\right)\sin\left(\frac{\pi}{2}-\frac{\alpha}{2}-\alpha_t\right), 0\right) \tag{B.43}$$

where

$$\overrightarrow{R_V} = \overrightarrow{OV}_{OXY} - \overrightarrow{OC} \tag{B.44}$$

$$\alpha_t = \angle\left(\overrightarrow{R_V}, -\vec{\imath}\right) \tag{B.45}$$

$$\alpha = \frac{\ell}{R_t} \tag{B.46}$$

The subscript OXY denotes that the corresponding vector has been projected in the $z = 0$ plane. This projection is given, for a generic vector $\overrightarrow{OP}$, by $\overrightarrow{OP}_{OXY} = \overrightarrow{OP} - \left(\overrightarrow{OP}\cdot\vec{k}\right)\vec{k}$. Fig. B.5 helps to understand the geometrical process to obtain $\overrightarrow{VV'}$, showing a graphic representation of the movement of V in the OXY plane.

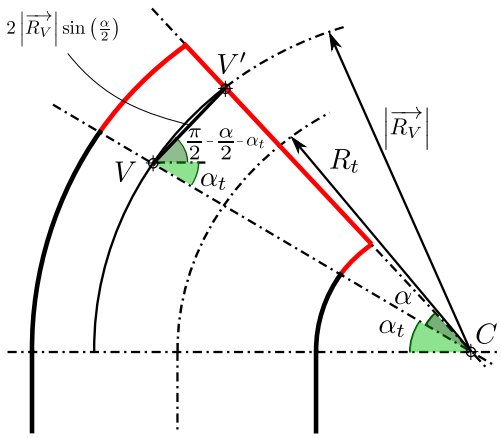

Figure B.5: Graphic representation of the movement of a vertex V in the OXY plane. The reader is referred to the main text for a detailed explanation on every variable.

B.3.1 Swept Volume

As the trajectory of each point of the mesh M is easily obtained, the volume swept in the movement of a face F is directly computed applying the *First Theorem of Pappus-Guldin* [4], once obtained the centroid G_F of F.

In order to calculate this centroid G_F of the face F (polygonal), a triangular decomposition is carried out, followed by a weighted average of the centroids of each triangle, as explained in [5].
Once the position $\overrightarrow{OG_F}$ is known, the volume Ω_F swept in the movement of F is given by:

$$\Omega = A \cdot \alpha ||\overrightarrow{R_{G_F}}|| \tag{B.47}$$

where A is the area of F, and $\overrightarrow{R_{G_F}} = \overrightarrow{OG_F}_{OXY} - \overrightarrow{OC}$.

References

[1] O. Estruch, O. Lehmkuhl, R. Borrell, C. D Pérez Segarra, A. Oliva, A parallel radial basis function interpolation method for unstructured dynamic meshes, Comput. Fluids. 80 (2013) 44-54.

[2] R. L. Burden, J. D. Faires, Numerical Analysis, Cengage Learning (2001).

[3] W. Kuhnel, Differential geometry: curves - surfaces - manifolds, American Mathematical Society (2005).

[4] A. W. Goodman, G. Goodman, Generalizations of the Theorems of Pappus, The American Mathematical Monthly, 76:4 (1969) 355-366.

[5] A. H. Stroud, Approximate calculation of multiple integrals, Prentice-Hall Inc., Englewood Cliffs, N. J., 1971.

C

List of publications and presentations at congresses

In international journals

E. Gutiérrez, N. Balcázar, O. Lehmkuhl, and A. Oliva, On the solution of the full three-dimensional Taylor bubble problem by using a coupled Conservative Level Set - Moving Mesh method, Journal of Physics: Conference Series, 745:3 (2016).

E. Gutiérrez, N. Balcázar, E. Bartrons, J. Rigola, Numerical study of Taylor bubbles rising in a stagnant liquid using a Level-set / Moving-Mesh method, CCemical Engineering Science 164 (2017) 158-177.

E. Gutiérrez, F. Favre, N. Balcázar and J. Rigola, On the solution of the problem of a drop falling against a plane by using a level set - moving mesh - immersed boundary method, International Journal of Computational Methods and Experimental Measurements 6:1 (2017) 208-219.

E. Gutiérrez, F. Favre, N. Balcázar, A. Amani and J. Rigola, Numerical approach to study bubbles and drops evolving through complex geometries by using a level set - moving mesh - immersed boundary method, Chemical Engineering Journal 349 (2018) 662-682.

Presentations at congresses

E. Gutiérrez, N. Balcázar, O. Lehmkuhl, and A. Oliva, On the solution of the full three-dimensional Taylor bubble problem by using a coupled Conservative Level Set - Moving Mesh method, Eurotherm 2016.

E. Gutiérrez, F. Favre, N. Balcázar and J. Rigola, On the solution of the problem of a drop falling against a plane by using a level set - moving mesh - immersed boundary method, International Conference on Computational and Experimental Methods in Multiphase and Complex Flow 2017.

D

Computational resources

FI-2016-1-0024 Direct Numerical Simulations of Taylor bubbles in inclined channels by using domain optimization methods, Spanish Supercomputing Network - Altamira Supercomuter, 01/03/2016 - 01/07/2016.

FI-2016-3-0037 Computations of 3D Taylor bubbles in a broad range of flow conditions, Spanish Supercomputing Network - Marenostrum Supercomputer, 01/11/2016 - 03/03/2017.

FI-2017-2-0042 Computations of the impact of a bubble against an inclined plane, Spanish Supercomputing Network - Finisterre Supercomputer, 01/07/2017 - 03/11/2017.

FI-2018-1-0036 DNS of the impact of a rising drop against a solid circular cylinder, Spanish Supercomputing Network - Calendula Supercomuter, 01/03/2018 - 01/07/2018.

tceng015c Computations of the impact of a bubble against a curved surface, Irish Centre for High-End Computing, from 15-05-2017.